Edited by
J.P. Hirth and L. Kubin

Dislocations in Solids
Volume 15

North-Holland

Dislocations in Shock Compression and Release

M.A. MEYERS, H. JARMAKANI

Materials Science and Engineering Program, Departments of Mechanical and Aerospace Engineering and Nanoengineering, University of California, San Diego, La Jolla, CA 92093-0418, USA

and

E.M. BRINGA, B.A. REMINGTON

Lawrence Livermore National Laboratory, Livermore, CA 94550, USA

Contents

1. Introduction

The response of metals to very high strain rate deformation is reasonably well-understood. In particular, shock experiments have been carried out for over 60 years. Detonating explosives in direct contact with the metal were first used [Fig. 1(a)], followed by the use of flyer plates driven by explosives and gas-guns to create the compressive pulse in the material [Figs 1(b) and 1(c)], and pressures attained were on the order of tens of GPa with accompanying strain rates on the order of $10^7\,s^{-1}$ with durations on the order of microseconds or fractions thereof. More recently, laser pulses have also been used to study shock compression in metals. The generation of shock pulses in metals from laser-pulse induced vaporization at the surface was first demonstrated by Askaryon and Morez [1] in 1963. Shortly thereafter, White [2] and others [3–5] advanced this technique and postulated that lasers could be used to obtain Hugoniot data for a broad range of pressures. The use of surfaces covered by a laser-transparent overlay was introduced by Anderholm [6]; this enabled the confinement of the vapor products resulting in an increase of the peak pressure of the shock incident on the metal.

In 1963, Leslie et al. [7] reported dislocation structures in shock-compressed iron. Early experiments by Johari and Thomas [8] and Nolder and Thomas [9] investigated defect substructures generated in explosively deformed copper and copper–aluminum alloys and nickel. Table 1 presents the main reviews on the topic with the primary emphasis of the articles.

The rapid heating and thermal expansion of the surface layers during laser irradiation generates a shock which propagates through the material. Shock pressures higher than those in planar impact setups can be achieved (up to 10,000 GPa), and the strain rates attained are as high as 10^9–$10^{11}\,s^{-1}$. A basic difference is that the duration of the pulse in the laser shock is on the order of nanoseconds rather than microseconds. Fig. 1(d) shows several modes by which lasers can be used to shock compress materials: (i) the direct illumination configuration, (ii) plasma confining overlay, (iii) laser-driven flyer plates, and (iv) the *hohlraum* configuration, converting the laser pulse to X-rays. Shock amplitudes as high or higher than those generated by explosives or planar impact devices can be generated with a basic difference: the duration of the shock pulse is in the nanosecond range [10]. More accurate microstructural characterization is possible due to the self-quenching mechanism associated with laser shock. Some of the earliest experimental work on laser shock damage is from Armstrong and Wu [11], who carried out Berg-Barret X-ray diffraction experiments on laser damage in zinc.

Laser shock and isentropic compression experiments (ICEs; discussed in detail in Section 6) are rapidly evolving as effective methods to explore the extreme pressure, strain rate, and temperature regimes inaccessible through other
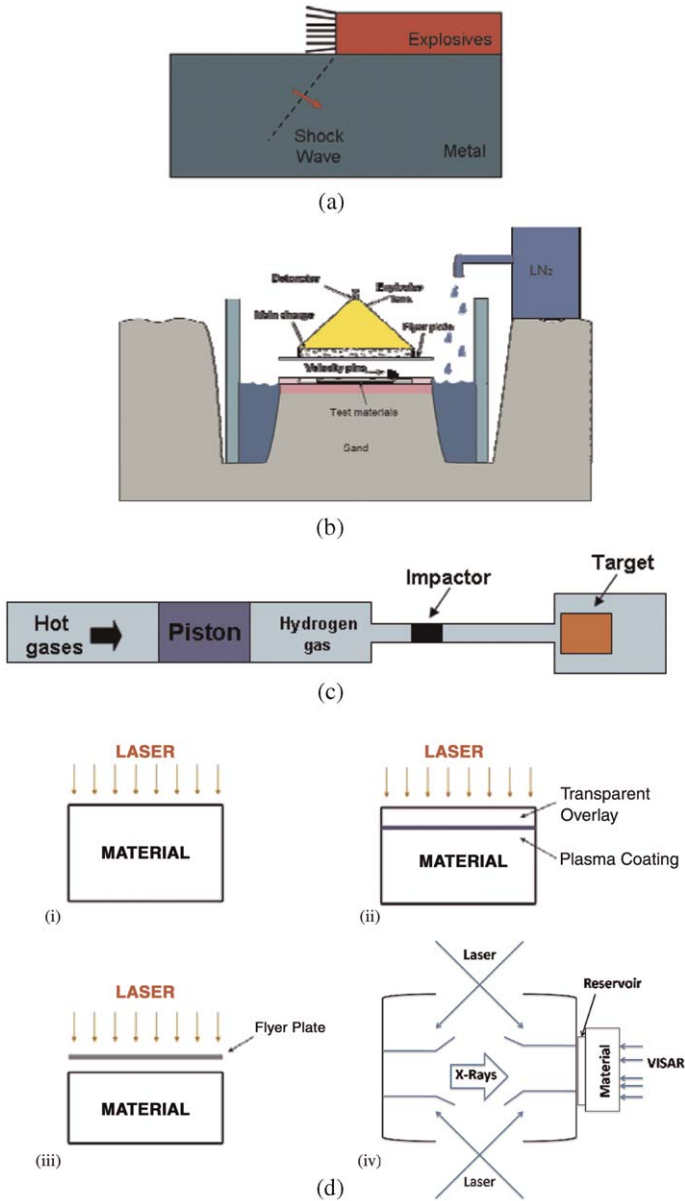
Fig. 1. (a) Configuration for generating an HE-induced shock in metal; (b) Schematic of a shock recovery experiment performed by acceleration of a flyer plate by an explosive charge; (c) gas-gun driven shock compression experiments; (d) Methods of laser shocking materials; (i) direct laser illumination at an intensity above the ablation threshold; (ii) laser irradiation through a transparent overlay to increase achievable pressures; (iii) laser accelerated flyer plate; and (iv) laser generated X-rays through a *hohlraum* (indirect drive).

Table 1
Review articles on dislocation effects in shock loading

Author	Year	Focus
Dieter [12,13]	1961, 1962	First TEM
Zukas [14]	1966	
Leslie [15]	1973	
Davison and Graham [16]	1979	Physics of shock-induced defects
Meyers and Murr [10]	1981, 1983	Metallurgical effects
Mogilevsky and Newman [17]	1983	Mechanisms of deformation
Murr [18]	1988	TEM, mechanical effects
Meyers [19]	1994	Shock front models, TEM
Gray [20,21]	1992, 1993	TEM
Remington et al. [22]	2004	Physics of laser shock compression
Armstrong and Walley [23]	2008	High strain rate deformation of metals

techniques. Although laser shock compression does not yet have the temporal and spatial uniformity of pressure as plate impact experiments, it has a significant advantage, especially from the point of view of recovery. The post-shock cooling is orders of magnitude faster than in plate-impacted specimens because of two key factors: (a) the short duration of the pulse and (b) the rapid decay, creating a self-quenching medium.

More recently [24–26], pulsed X-ray diffraction has been used to obtain quantitative information of the lattice distortions at the shock front. These measurements can be used to resolve issues of dislocation generation and motion as well as lattice distortions at the shock front. Coupled with recovery experiments to examine the deformation substructures, laser shock experiments are being used to obtain an understanding of compressive shock defect generation and relaxation processes. In this chapter, recent work on the laser shock compression of copper, copper alloys, and nickel is reviewed, examining the effects of crystallographic orientation, pressure decay, and stacking-fault energy (SFE) on the deformation microstructure. There is specific emphasis on the slip to twinning transition. A new criterion for the transition from perfect to partial dislocation nucleation is proposed. This criterion explains the transition from cells to stacking faults, why for pure copper the cell structure gives rise to planar stacking faults above a critical pressure, and how this transition pressure decreases with a decrease in SFE.

The response of dislocations to shock compression can be rationalized through the classic Orowan equation [27], proposed in 1940:

$$\gamma = k\rho b\bar{l},^{\star} \tag{1}$$

where γ is the strain, ρ the mobile dislocation density, $\boldsymbol{b}$ the Burgers vector, $\bar{l}$ the mean distance traveled by a dislocation, and k is a proportionality constant. By taking the time derivative:

$$\dot{\gamma} = k\boldsymbol{b}\frac{d}{dt}(\rho\bar{l}). \tag{2}$$

Thus, the strain rate has two components:

$$\dot{\gamma} = k\mathbf{b}\rho \frac{d\bar{l}^{\star}}{dt} + k\mathbf{b}\bar{l}\frac{d\rho}{dt}.$$ (3)

Prescribed strain rates can be either accommodated by dislocation movement (at a velocity $d\bar{l}/dt$), the generation of dislocations ($d\rho/dt$), or by a combination of both. At the lower strain rates, the velocity of dislocations is not a limiting factor, but in shock compression, especially at higher pressures (above the HEL), the $d\rho/dt$ term dominates. Thus, the generation and not the movement of dislocations determines the overall configuration. Indeed, Zerilli and Armstrong [28] pointed out this aspect of the Orowan equation which cannot be overlooked, if one considers the change in dislocation density due to the activation of sources. Armstrong and Elban [29] also note that heat generated by rapid dislocation motion in shock-compressed energetic crystals plays an important role in the detonation process. Armstrong et al. [30,31] addressed the relationship experimentally obtained by Swegle and Grady [32] and expressed it in terms of dislocation dynamics, incorporating nucleation and propagation of dislocations at the front. Specific mechanisms for the generation and high-velocity motion of these dislocations are presented in Section 2. There exist a number of reviews on defects generated in shock compression. The most prominent are shown in Table 1. These works supplement the material presented here and provide a broad background.

2. Early models for dislocations in a shock front

A number of models have been proposed for the generation of dislocations in shock loading. They will be reviewed next. The dislocation generation mechanisms operating under shock loading vary from the conventional ones operating at low strain rates, where the first term in eq. (3) (dislocation motion) dominates to mechanisms uniquely associated with high strain rates, including the dominance of the second term in eq. (3) (dislocation generation).

2.1. Smith's model

Smith [21] made the first attempt to interpret the metallurgical alterations produced by shock waves in terms of fundamental deformation modes. He depicted the interface as an array of dislocations that accommodates the difference in lattice parameter between the virgin and the compressed material. In this sense, the Smith interface resembles an interface between two phases in a transformation. Fig. 2(a) shows the interface if no dislocations were present; the deviatoric stresses cannot be relieved. This interface of dislocations would, according to Smith, move with the shock front, as shown in Fig 2(b). Since the density of dislocations at the front is, according to Smith, 10^3–10^4 times higher than the residual density, sinks and sources, moving at the velocity of the shock, were postulated.
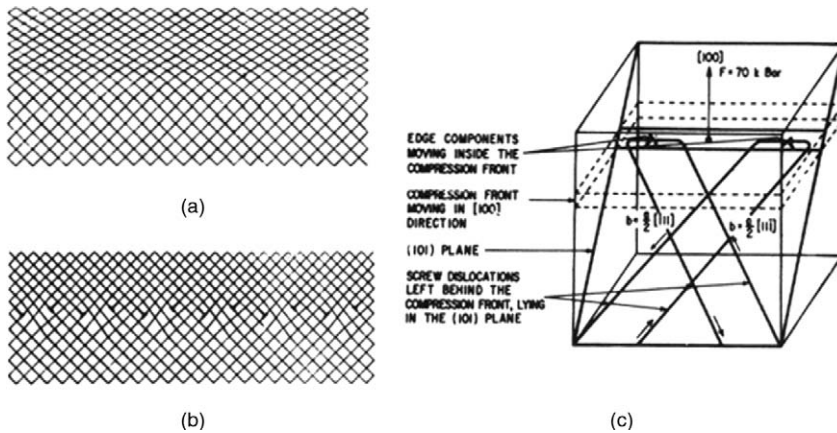
Fig. 2. (a, b) The Smith [33] and (c) Hornbogen [34] models for dislocation generation in shock loading.

2.2. Hornbogen model

Hornbogen [34] modified Smith's model because it could not account for the residual dislocation substructures found in shock-loaded iron, where screw dislocations lying on ⟨111⟩ directions were found. Hornbogen's explanation is shown schematically in Fig. 2(c). Dislocation loops are formed as the compression wave enters the crystal. The edge components move with the velocity of the shock front, so that their compression zone forms the wave; and the screw components remain and extend in length as the edge components advance. As will be seen in Section 5, the residual dislocation density in iron is, indeed, comprised primarily of screw dislocations.

2.3. Homogeneous dislocation nucleation model

The limitations of Smith and Hornbogen's proposals led Meyers [35,36] to propose a model whose essential features are as follows:

1. Dislocations are homogeneously nucleated at (or close to) the shock front by the deviatoric stresses set up by the state of uniaxial strain; the generation of these dislocations relaxes the deviatoric stresses.
2. These dislocations move short distances at subsonic speeds.
3. New dislocation interfaces are periodically generated as the shock wave propagates through the material.

This model presents, with respect to its predecessors, the following advantages:

1. No supersonic dislocations are needed.
2. It is possible to estimate the residual density of dislocations.

An early version was proposed in 1978 [36]. Fig. 3 shows the progress of a shock wave moving through the material in a highly simplified manner. As the shock wave penetrates into the material, high deviatoric stresses effectively distort the initially cubic lattice into a rhombohedral lattice [Fig. 3(a)]. When these stresses reach a certain threshold level, homogeneous dislocation nucleation can take place [Fig. 3(b)]. This process of deviatoric stress buildup and relaxation through the homogeneous dislocation loop generation repeats itself [Figs 3(c) and 3(d)].

Fig. 4 shows an idealized configuration of dislocation loops when a shock wave propagates through the lattice. The planes are (1 1 1) and the dislocations are edge dislocations. The screw components are not shown in the picture. As the shock-front advances, the dislocation interface is left behind. As this occurs, elastic deviatoric stresses build up.
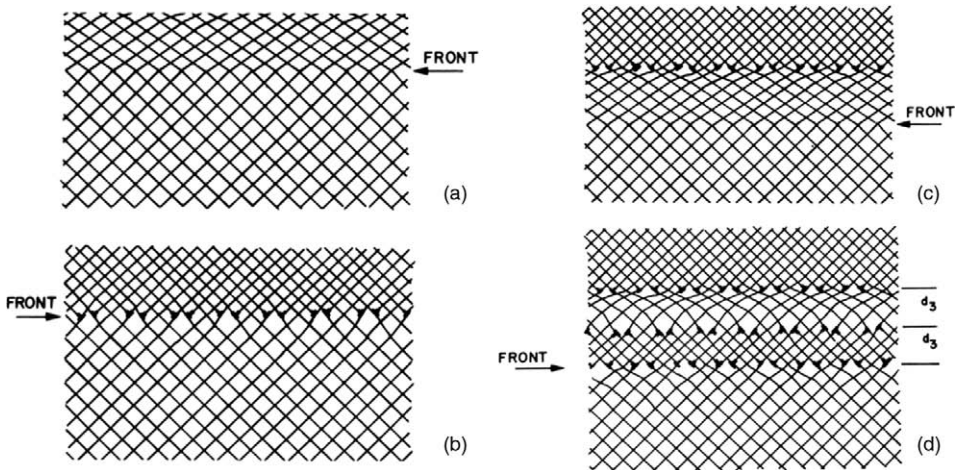

Fig. 3. Shock front evolution according to a homogeneous dislocation nucleation model [36].
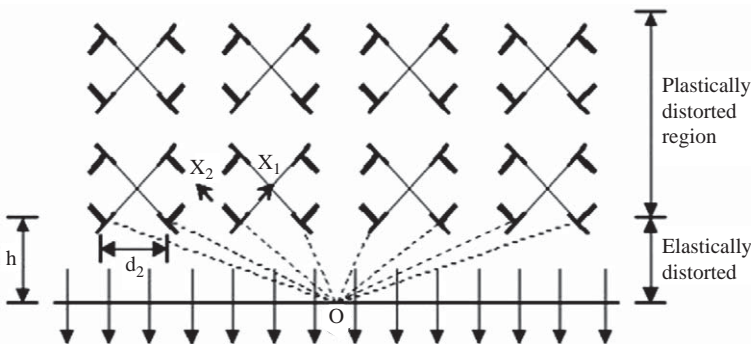
Fig. 4. Stresses due to dislocations on a reference point 0 at shock the front (adapted from [37]).

We reproduce below the early and more recent calculations and discuss the reasons for the difference. As shown in Fig. 4, successive layers of interfacial dislocation loops are generated and left behind by the shock front. The insertion of dislocations relaxes the deviatoric stresses that elastically distort an ideal lattice to rhombohedral. Hence, a reduced cubic lattice is restored by the insertion of dislocations in the near vicinity of the shock front. The dislocation spacing along the front required to accommodate this is d_2 (Fig. 4). This situation is analogous to the epitaxial growth of films, in which interface dislocations, creating a semi-coherent boundary, accommodate the disregistry. The dislocation spacing along the front is calculated from the ratios of the original and compressed lattices. The ratio between the initial and compressed specific volumes of the lattices, V_0 and V, is:

$$\frac{V}{V_0} = \left(\frac{\bm{b}_s}{\bm{b}_0}\right)^3, \tag{4}$$

where $\bm{b}_0$ is the original Burgers vector and $\bm{b}_s$ the compressed Burgers vector. The spacing of dislocations at the front is given by the epitaxial growth equation:

$$d_2 = k\frac{\bm{b}_0\bm{b}_s}{\bm{b}_0 - \bm{b}_s}, \tag{5}$$

where k is an orientation factor. These interplanar spacing can be expressed in terms of dislocation densities. The dislocation density generated can be calculated from d_2, and h, the spacing between successive dislocation loop layers nucleated. Since each distance d_2 corresponds to two dislocations (on planes (111) and $(1-11)$), the spacing $d_2/2$ is taken. Thus, the dislocation density, ρ, is:

$$\rho = \frac{2}{d_2 h}. \tag{6}$$

At this point, the early and more recent calculations diverge. In the early version, h was taken equal to d_2, as a first approximation. This is reasonable and is based on the assumption that the stress field of a dislocation has a radius equal to the dislocation spacing, d_2. Thus:

$$\rho = \left(\frac{2}{d_2^2}\right)\Bigg(\tag{7}$$

The more recent model, developed with the important input of Ravichandran (private communication, 2002), uses a more detailed analysis. The spacing between dislocation loop layers is calculated by using the stress fields around dislocations and summing them at a generic point 0 at the front over the stress field of all dislocations. The stress fields due to the dislocation arrays balance elastic distortion at the shock front. Thus, when the stresses at the front reach a critical level (at which homogeneous dislocation nucleation of loops can occur), a new layer of dislocations is formed. The shear stress at point 0 in the front (Fig. 4) can be

estimated from the stress fields due to the last layer of dislocations. This is described by Meyers et al. [37]. Assuming edge dislocations only:

$$\sigma_{11} \approx \frac{Gb}{2\pi(1-v)} \frac{2\sqrt{2}}{4nd_2} \left(\to \sum_{-\infty}^{+\infty} \frac{1}{n} = 0, \right. \tag{8}$$

$$\sigma_{22} \approx \frac{Gb}{2\pi(1-v)} (-2h^2) \frac{2\sqrt{2}}{n^3 d_2^3} \left(\to \sum_{-\infty}^{+\infty} \frac{1}{n^3} = 0, \right. \tag{9}$$

$$\sigma_{12} \approx \frac{Gb}{2\pi(1-v)} \frac{2\sqrt{2}}{n^2 d_2^2} \left(h \to \sum_{-\infty}^{+\infty} \frac{1}{n^2} = \frac{\pi^4}{90}, \right. \tag{10}$$

where v is Poisson's ratio.

Thus, the normal stresses due to dislocations at 0 are zero and one has only the shear stress. When this stress equals the stress required for the nucleation of a dislocation loop, a new dislocation is generated. This is discussed further in Section 6.4. The dislocation density can be obtained from the stress for homogeneous nucleation of dislocation loops. From Xu and Argon [38], the activation energy is zero at the critical stress for plastic flow, which is considered as the stress at which the loops are generated. This stress was taken as [39]:

$$\sigma_{12} = 0.04G. \tag{11}$$

For a more detailed discussion, see Section 4.1.

The spacing between dislocation planes can be calculated by setting eq. (10) equal to eq. (11):

$$h = \frac{0.8(1-v)}{\pi^2 b} d_2^2. \tag{12}$$

The dislocation density is obtained from eq. (6):

$$\rho = \frac{2\pi^2 b_s}{0.8(1-v)d_2^3}. \tag{13}$$

The Rankine–Hugoniot equation connecting pressure P to specific volume V is [29]:

$$P = \frac{C_0^2(1-V/V_0)}{V_0[1-S(1-V/V_0)]^2}. \tag{14}$$

where C_0 is the ambient sound speed, and S is an equation of state (EOS) parameter. The application of eqs (4), (5), (7), and (14) leads to the dislocation density as a function of pressure (early model):

$$P = \frac{C_0^2 \{1 - [1/1 + kb_0(\rho/2)^{1/2}]^3\}}{V_0 \{1 - S[1 - [1/1 + kb_0(\rho/2)^{1/2}]^3]\}^2}. \tag{15}$$
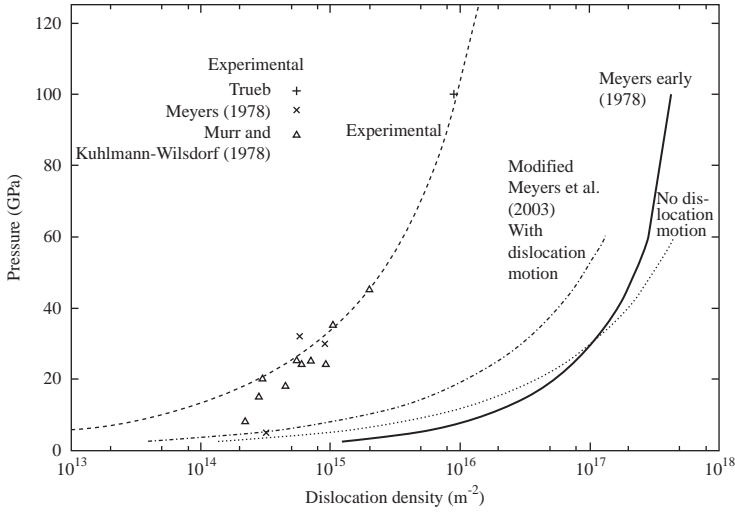
Fig. 5. Experimental (from Murr [40], Meyers [36], Bernstein and Tadmor [41], Murr and Kuhlmann-Wilsdorf [42], and Trueb [43]) and computed dislocation densities as a function of shock pressure for nickel.

These initial calculations of dislocation densities produced results orders of magnitude higher than the observed results [36]. They are shown in Fig. 5.

A recalculation of the improved model by Meyers et al. (2003) [37], using a slightly modified approach, is shown below. By substituting eq. (4) into eq. (5) and the result into eq. (13) one obtains:

$$\rho = \frac{2\pi^2}{0.8(1-v)k^3 b_0^2} \left(\frac{V}{V_0}\right)^{-2/3} \left[1 - \left(\frac{V}{V_0}\right)^{1/3}\right]^3. \tag{16}$$

Solving eqs (14) and (16) by assigning different values $V/V_0 < 1$, one obtains the dislocation density as a function of pressure. This is shown in Fig. 5. The difference between the original (1978) and improved models is clear from the two plots in Fig. 5 and by comparing eqs (7) with (13). Eq. (13) can be approximated as $35b_s/d_3^2$. For low pressures, $d_2 > 35b_s$ and the early model (1978) prediction gives higher dislocation densities. For $P > 32$ GPa, $d_2 < 35b_s$ and the 2003 model predicts a higher dislocation density.

There is also a second case: moving dislocations. If the dislocations are assumed to move under the influence of the high residual stresses, they try to "catch up" with the front, the maximum of h_2 is reached. This results in an increase in the spacing between dislocation arrays from h, given in eq. 12, to h_2:

$$h_2 = h \left[\left(+\frac{kV_d}{U_s}\right) \left(\right. \tag{17}$$

where V_d is the dislocation velocity and k an orientation factor. When $V_d = 0$, eq. (17) reduces to eq. 12. When the dislocation velocity equals the shear wave velocity V_{sw} (our maximum assumed velocity for dislocation velocities), h_2 reaches a maximum:

$$h_2 = h\left[\left(+\frac{kV_{sw}}{U_s}\right)\right]\left(\right. \tag{17a}$$

The predictions based on the two values of h (eq. (12) for stationary dislocations and eq. (17a) for dislocations moving at the shear sound velocity) are shown in Fig. 5 and compared with experimental results. The calculations are lower, by a factor of 5–10, than the measured densities. However, this is much closer to the experimental results than the earlier model [36].

Evidently, the improved calculation predicts values that compare more favorably with dislocation densities measured from transmission electron microscopy. The approach was thought to predict realistically the currently observed results. However, recent molecular dynamics (MD) calculations predict results that are much closer to the original calculations (early model). One possible reason for this is that the ''improved'' model, based on stresses from dislocations, does not consider the stresses from the opposing dislocation in each loop. Only the dislocations in the last layer, facing the front, are included. If the dislocations in the backs of the loops were considered, there would be cancellation of the stress fields when the loop radius is small in comparison with h. As shown in Section 6.4, the nucleating loop radius, which is a function of the applied shear stress, is small at the high shear stresses imposed by shock compression. Thus, the early model might be a better representation of the generation of dislocations, and the spacing between adjacent dislocation layers in the shock wave propagation direction is closer to d_2 than to h. This is further discussed in Section 8.

2.4. Zaretsky model

Zaretsky [44] proposed a dislocation model based on multiplication and motion of partial dislocations (rather than perfect dislocations) bounding a stacking fault. In essence, their model extends the homogeneous dislocation nucleation model of Section 2.3 to partial dislocations. Stress-activated stretching of lateral branches of the partial dislocation bowed-out segment results in collapse of these branches with subsequent restoration of the ''initial'' dislocation half-loop and generation of a ''fresh'' partial dislocation loop, both capable to produce the next multiplication act. The multiplication results in the exponential increase of the concentration of both dislocations and stacking faults. The model explains the variations of X-ray diffraction patterns for material undergoing shock compression and the shock-induced formation of twins. Fig. 6 shows an illustration of the generation of stacking faults according to Zaretsky [44].
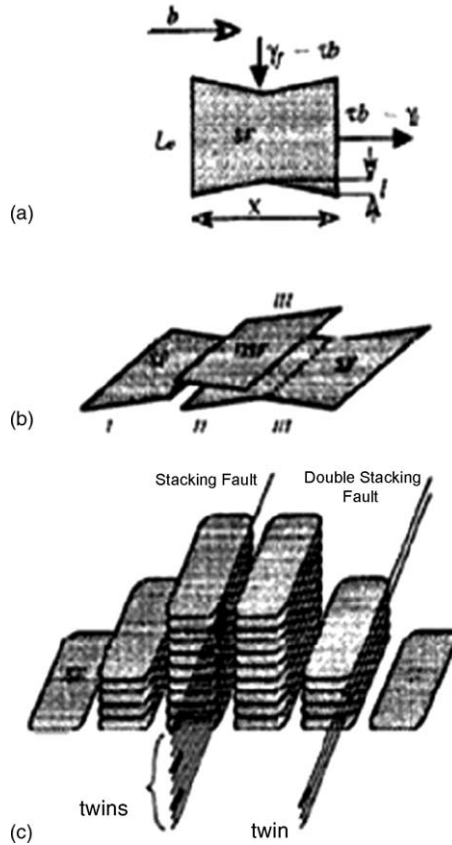
Fig. 6. The Zaretsky [44] mechanism for partial dislocation loop formation; (a) partial loop expansion; (b) stacking-fault overlap; and (c) successive partial loops forming twins.

2.5. Weertman mechanisms

Weertman [45] considered two regimes of shock-wave propagation: weak shocks (pressure small in comparison with bulk elastic modulus) and strong shocks (pressure on the same order of bulk elastic modulus). For weak shocks, Weertman and Follansbee [46,47] considered the front as composed of a superposition of plastic waves. They applied the Orowan equation [eq. (2)] eliminating the $d\rho/dt$ term:

$$\dot{\gamma} = kb\rho \frac{d\bar{l}}{dt}. \tag{18}$$

Thus, conventional mechanisms of dislocation motion accommodate the plastic strain at the front. For strong shocks, Weertman [45] proposed a mechanism incorporating both supersonic dislocations in a Smith interface at the front and a homogeneous dislocation generation behind the front. This is a hybrid of the Smith and Meyers models, as can be seen in Fig. 7.
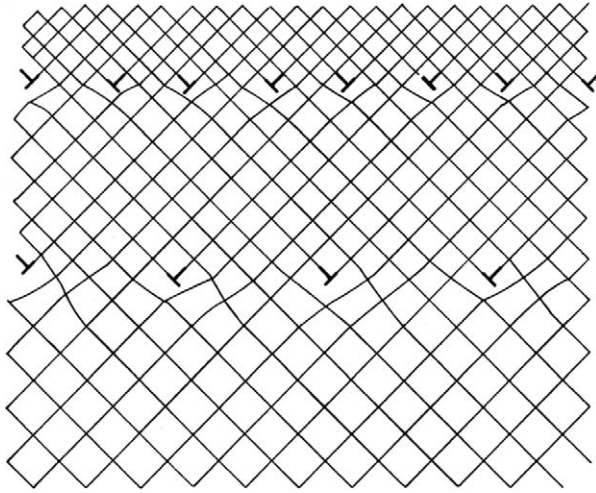
Fig. 7. The Weertman mechanism for dislocations in a strong shock using supersonic dislocations at the front and subsonic dislocations behind the front (Weertman [45]).

2.6. The question of supersonic dislocations

The existence of supersonic dislocations is fundamentally important and yet is an unresolved question. One of the earliest suggestions was a special configuration postulated by Eshelby [48] to move dislocations supersonically. Weertman [49,50] developed the mathematical analysis of subsonic, transonic, and supersonic dislocations, using the relativistic theory originally proposed by Frank [51]. He divided the behavior into three regimes: subsonic (below the shear-wave velocity); transonic (between the shear and the longitudinal wave velocities); and supersonic (higher than the longitudinal wave velocity). Thus, these researchers accepted the possibility of supersonic dislocations.

Gumbsch and Gao [52] carried out MD calculations in simple shear and obtained the velocities shown in Fig. 8 for an edge dislocation. Their atomistic simulations show that dislocations can move transonically and even supersonically if they are created as supersonic dislocations at a strong stress concentration and are subjected to high shear stresses. We note that the divergence in dislocation velocity at the Rayleigh velocity (edge dislocations) or shear-wave velocity (screw dislocations) is a consequence of assuming a compact dislocation core. MD simulations show a spreading core and these divergencies vanish. The topic is discussed further by Hirth and Lothe [39] and Hirth et al. [53]. Gilman [54] showed that the limiting speeds of moving dislocations are determined by inertial effects, or by viscous drag, at their cores. He developed simple expressions for the limiting speeds. He argued that the Frank proposal that the speeds are limited by the inertia of the elastic fields, accompanied by Lorentz contractions, is flawed because it neglects the angular momentum of a moving dislocation; or, equivalently, because it assumes that the motion is steady if the velocity is constant, which is not possible because the motion
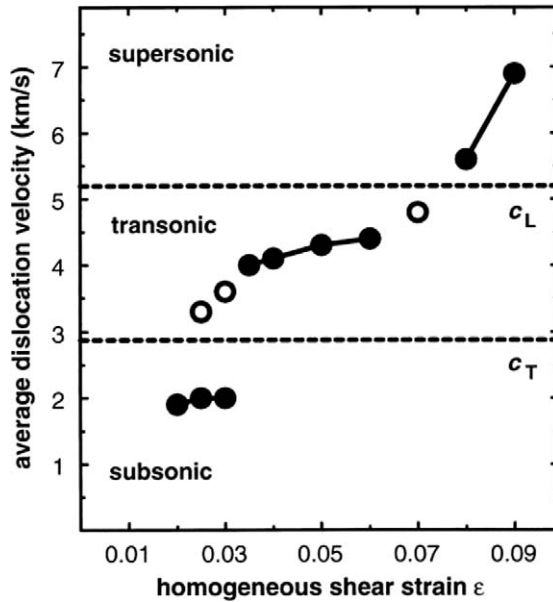
Fig. 8. Edge dislocation velocity versus applied shear strain in tungsten. The different regimes of stable dislocation motion at constant velocity (solid circles) are connected by solid lines. Open circles mark substantially varying velocities or the (average) velocity of dislocations before stopping. Dashed lines indicate the transverse and longitudinal elastic wave velocities. From Gumbsch and Gao [52].

creates plastic deformation. He also discarded the Gumbsch and Gao [34] MD calculations predicting supersonic dislocations.

3. *Polycrystallinity effects*

Meyers [55,56] and Meyers and Carvalho [57] proposed, in 1976, that the shock front was affected by the polycrystallinity of the material and acquired an irregular configuration. This concept had been originally expressed in a qualitative manner in Meyers' [55] doctoral dissertation. They performed simple calculations showing that the shock-front width increased with increasing grain size, for the same travel distance. Based on experimental results by De Angelis and Cohen [58] suggesting that grain rotation could occur in shock compression, Meyers et al. performed a number of experiments in aluminum [59], copper [60], and stainless steel [61]. For aluminum, Dhere et al. [59] varied the grain size from 26, 70, and 440 μm and subjected the systems to shock deformation at 5.8 GPa. However, after the shocks they could not detect any change in texture by X-ray diffraction, even though the cold rolled samples had significant texture changes. They also looked at misorientations within the grains by Kikuchi lines. Braga [60] shocked a copper bicrystal and observed a higher dislocation density close to the interface, suggesting
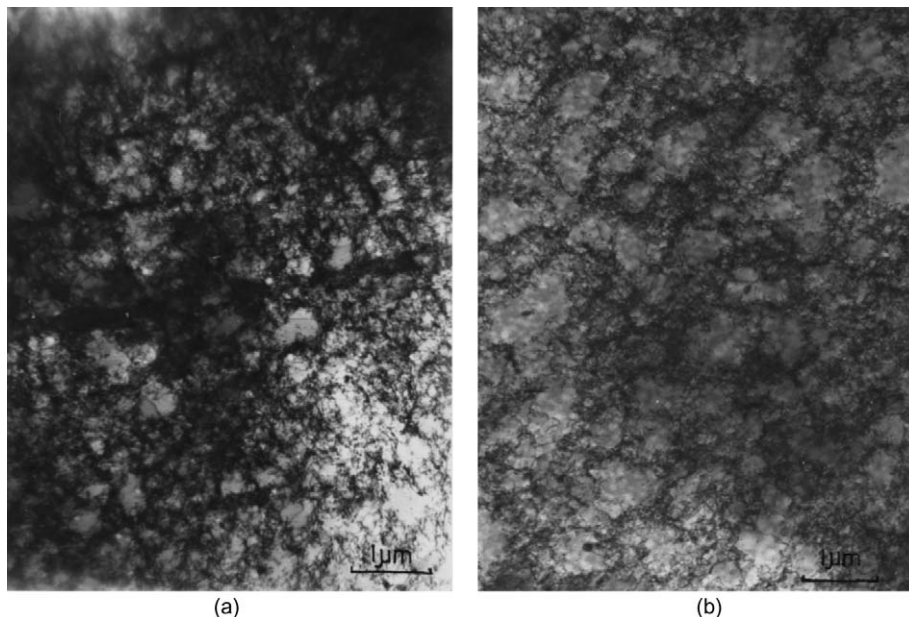
Fig. 9. Effect of polycrystallinity on the residual dislocation distribution in copper; (a) bicrystal close to the interface (grain boundary); (b) bicrystal far from the interface. From Braga [60].

an effect of polycrystallinity. Fig. 9 shows the dislocation cell structure in the monocrystalline region (away from the boundary) and close to the boundary. There is a definite difference. In stainless steels, Kestenbach and Meyers [61] identified changes in deformation mechanisms as a function of grain size. However, no grain rotation was observed.

Later, experiments carried out with Murr, Hsu, and Stone [62] on polycrystalline and monocrystalline Fe–Ni–Cr alloys revealed some differences in the micro-structure, the polycrystal exhibiting a slightly larger dislocation density. Systematic experiments with Murr [63,64] on nickel (monitoring the pressure pulse decay over distances of over 100 mm with samples having two widely different grain sizes) failed to reveal significant changes. Diagnostics (manganin gauges) did not show any difference in the rate of attenuation of the shock wave. This research direction was discontinued in the 1970s for lack of more sensitive diagnostic tools.

In 2006, atomistic simulations of shock wave propagation in nanocrystals were carried out by Bringa et al. [65]. The calculations demonstrate that the width of the wave is indeed a function of grain size, pressure, and time. The atomistic calculations match the analytical calculations of Meyers [56] and Meyers and Carvalho [57] for the width of the shock front for polycrystalline copper which, in turn, agreed with measurements of Jones and Holland [66] in the microcrystalline regime, as shown in Fig. 10.

The MD simulations also reveal the details of the propagation of a shock wave through the nanocrystalline (nc) metal. Fig. 11 shows snapshots at two different
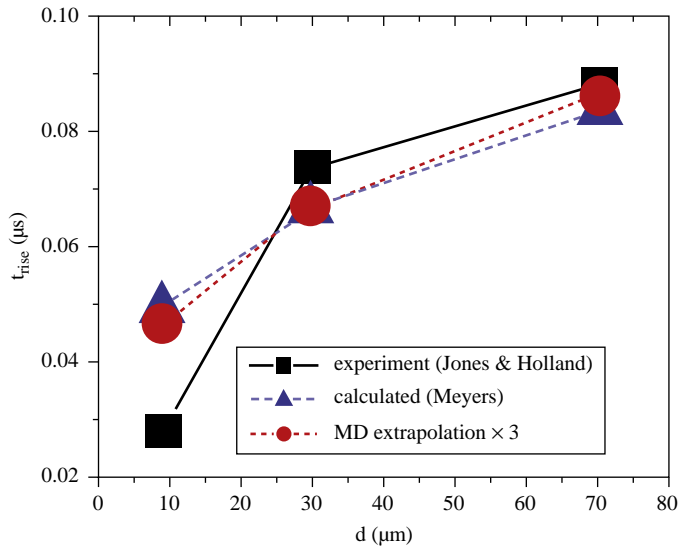
Fig. 10. Experimentally measured (Jones and Holland, [66]), analytically calculated (Meyers, [56]), and MD predictions of the rise time of the shock wave in copper as a function of grain size, d, in the conventional grain-size domain (Adapted from Bringa et al. [65]).
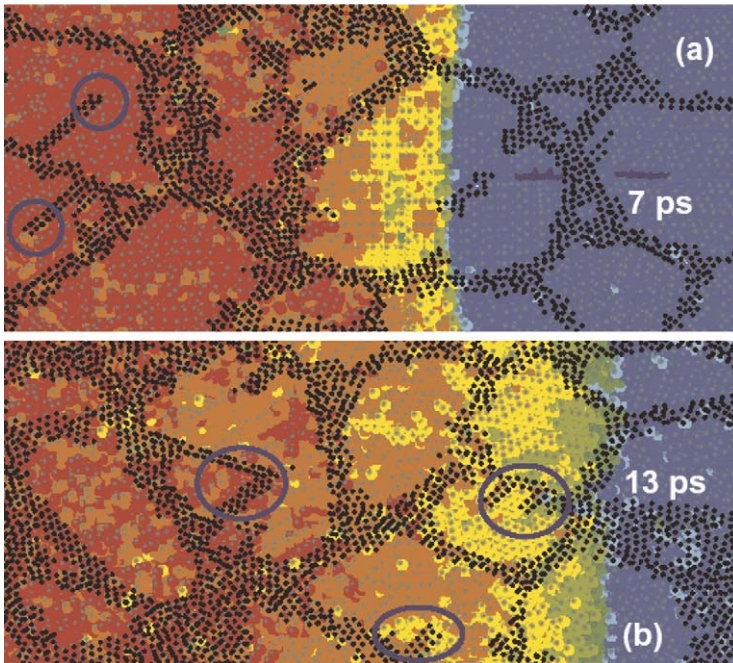
Fig. 11. MD simulations of shocked polycrystalline Cu showing the wave front at two different times. Grain-boundary atoms are shown as small black dots. $d = 5$ nm, $P = 22$ GPa, $U_p = 0.5$ km s^{-1} and strain $= 40$%. Atoms are colored according to their kinetic energy (red, high – moving at U_p; blue, low – unshocked). The upper frame shows a sharp front inside the grains, with some refraction due to orientation. Note that the energy levels track the GB, and that in frame (b) the front itself tracks the shape of one of the grains. Some of the stacking faults generated by the wave (emitted from grain boundaries) are marked with blue circles. From Bringa et al. [65].

times. The original color illustrations can be found in Bringa et al. [65]. The simulations suggest that the effect of grain boundaries in the width of the wave front is small compared to the effect of anisotropy from crystal to crystal. This is the reason why the continuum model by Meyers [56,57] was able to predict the front dispersion due to polycrystallinity. The dispersion of the wave calculated by MD, represented by the shock-front width normalized to the grain size, $\Delta z/d$, versus grain size, at three shock pressures (22, 34, and 47 GPa) is shown in Fig. 12(a). This shows that the normalized shock-front thickness decreases with increasing grain size

(a)

(b)
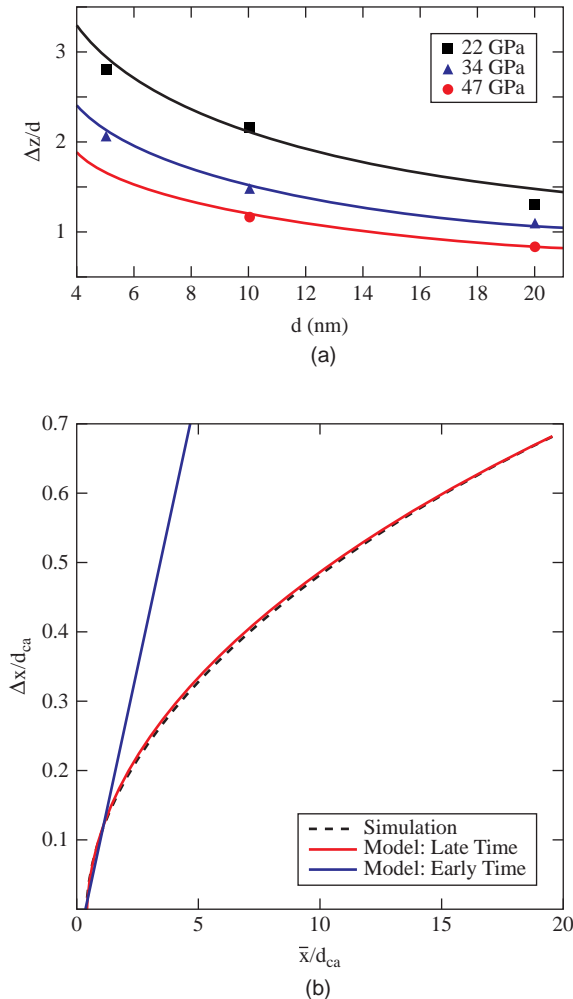
Fig. 12. (a) Results of MD simulations for shock front width, normalized to the grain size, versus pressure and grain size (from Bringa et al. [65]). (b) Normalized width of the shock front, $\Delta x/d$ versus normalized propagation distance x/d ($d =$ grain size); analytical (Model) and MD simulations. From Barber and Kadau [67], Fig. 2, p. 144106.

and with increasing pressure, whereas the absolute (un-normalized) shock-front width decreases with decreasing grain size. These simulations lead to a better understanding of the physics governing shock width. One of the possible applications of nanocrystalline (nc) metals, due to the greater sharpness of the shock front for small grain size, is as targets in the National Ignition Facility (NIF) at Lawrence Livermore National Laboratory [68]. The nc grain size would ensure that the fluctuations in the shock front remain small, decreasing the level of undesired hydrodynamic instabilities, which degrade inertial confinement fusion (ICF) capsule performance.

Barber and Kadau [67] extended the Meyers–Carvalho [56,57] analysis and obtained a shock-front width that varies as the ½ power of the penetration distance. Fig. 12(b) shows the normalized width of the shock front, $\Delta x/d$ versus normalized propagation distance x/d ($d =$ grain size). Both the analytical (Model) and MD simulations are shown. This result provides additional confirmation of the effect of polycrystallinity on the shock-front configuration.

4. Dislocation structures generated in different metals

Dislocation structures generated by shock loading have been exhaustively investigated. By far the most effective method of characterization is transmission electron microscopy (TEM). The first detailed characterization is due to Dieter [12,13] followed by Leslie [7]. The dislocation structure shown in Fig. 13 for BCC iron subjected to a 7 GPa shock reveals straight screw dislocations aligned in two directions. This morphology led Hornbogen to propose his shock propagation mechanism (Section 2.2). As the pressure is increased above the α(BCC)$\rightarrow\varepsilon$(HCP) transition, a completely different structure results, with profuse debris from the phase transition.

In FCC metals, on the other hand, one does not observe such a structure. Indeed, even Ta, a BCC metal, does not have such an aligned dislocation
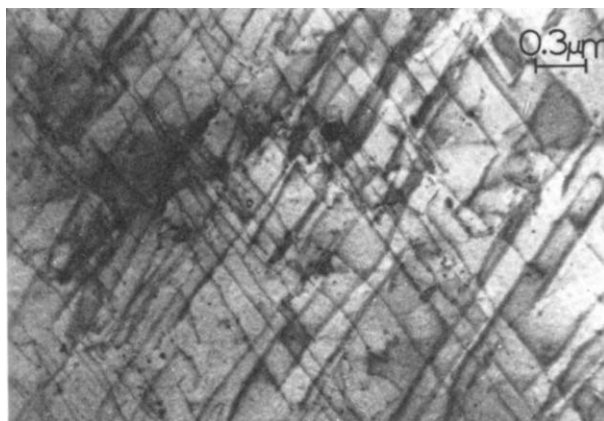
Fig. 13. Dislocation structure in BCC iron subjected to 7 GPa pressure shock. From Leslie et al. [7], Fig. 3, p. 122.
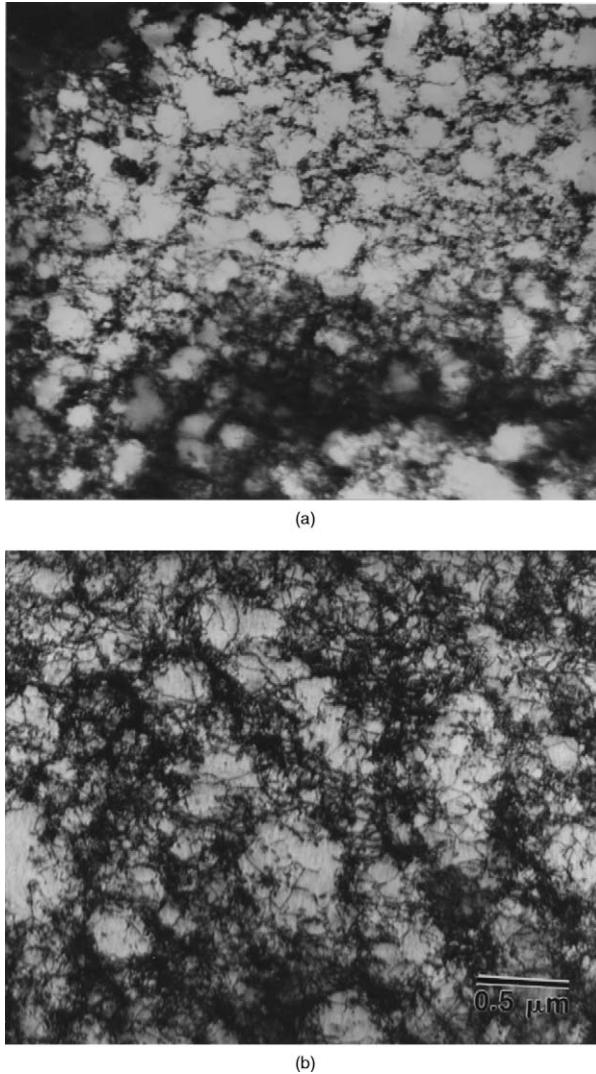
Fig. 14. Dislocation cells in shock-compressed (a) copper (5 GPa) and (b) nickel (10 GPa).

structure, being characterized by more random orientations of dislocation lines. Characteristic of high stacking fault energy (SFE) FCC metals are loose dislocation cells, illustrated in Fig. 14 for Cu and Ni. As the pressure increases the cell size decreases. Murr and co-workers [18,40,69–77] carried out extensive investigations on shock-recovered specimens. Murr and Kuhlmann-Wilsdorf [42] correlated the cell sizes to the shock pressures and proposed the relationship between the dislocation density, ρ, and pressure, P:

$$\rho \propto P^{1/2}. \tag{19}$$

Eq. (19) is a direct consequence of the Kuhlmann-Wilsdorf (K-W) relationship between dislocation cell size, l, and dislocation density (her Principle of Similitude):

$$l \propto \rho^{-1/2}. \tag{20}$$

The effects of both pressure and pulse duration for shocked Ni are seen in the $P-t_p$ plot by Murr [73] (Fig. 15). He developed similar maps for different metals
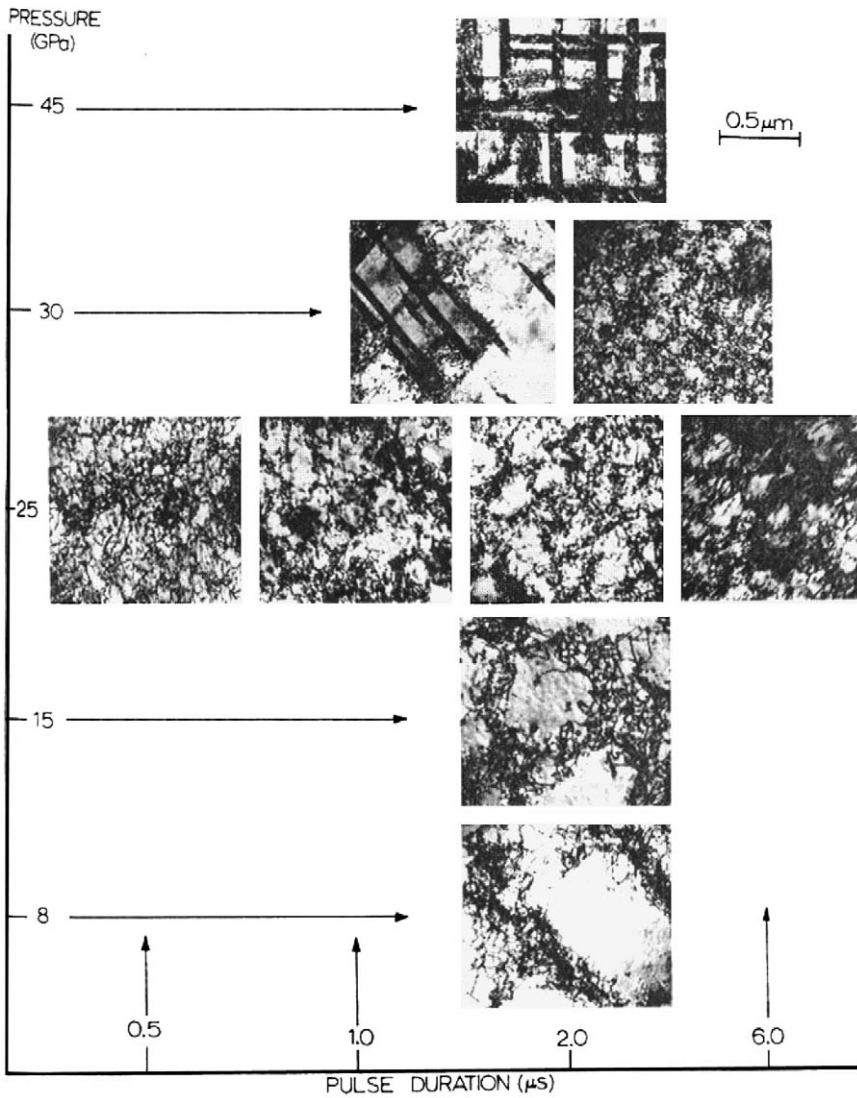
Fig. 15. Effect of shock pressure and pulse duration on residual substructure of nickel. Courtesy of L. E. Murr.
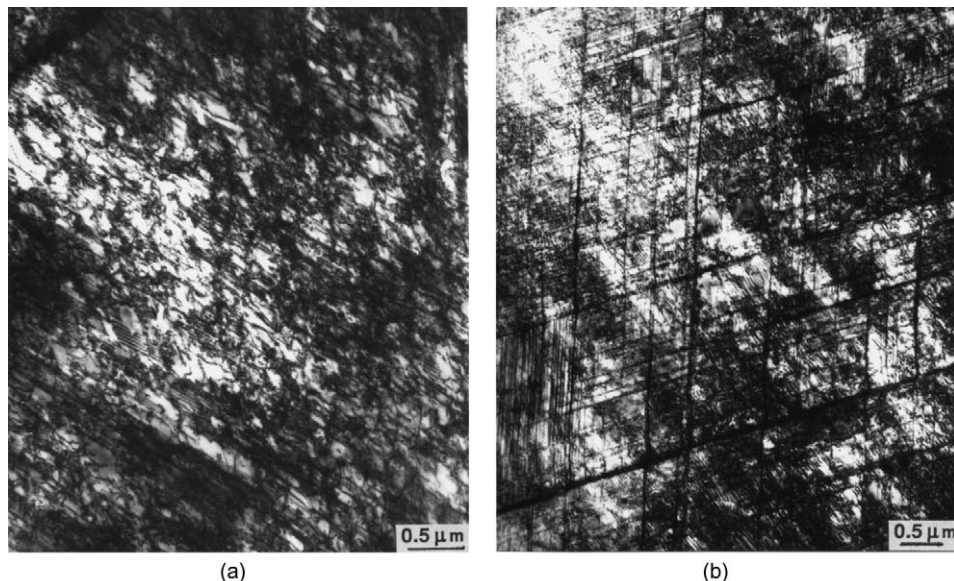
Fig. 16. Shock structures generated in intermetallic compounds (a) Ni$_3$Al (14 GPa) and (b) NiAl (23.5 GPa). Courtesy of G. T. Gray, LANL; also, Ref. [20], Fig. 6.13, p. 204.

and alloys. For Ni, as the pressure is increased the cell size decreases. At 30 GPa a new mechanism sets in – deformation twinning. The effect of pulse duration is evident in the horizontal line of photomicrographs, at 25 GPa. The dislocation cells become more distinct as the pulse duration increases.

As the SFE of FCC metals decreases (through alloying) the critical transition pressure for twinning also decreases. The dislocation cells are gradually replaced by planar dislocation arrays and stacking faults. This transition is treated in Section 6.

Intermetallic compounds are also hardened by shock waves. The dislocation structures are more complex by virtue of the ordered nature of the structure. Fig. 16 shows the dislocations generated in Ni$_3$Al and NiAl (Gray, private communication).

5. Stability of dislocation structure generated in shocks

The loose residual dislocation cell structure often encountered after shock compression is not stable, since the equilibration time for recovery is minimal. Hence, upon plastic deformation at conventional strain rates (10^{-3}–10^{-4} s^{-1}), the residual dislocation structure often collapses into better defined cells, with an associated stress drop. This phenomenon, called "work softening," was first observed in low-temperature shock deformation of FCC metals followed by ambient temperature deformation (e.g., Longo and Reed-Hill [78,79]). The shock-induced structure after subsequent plastic deformation is shown in Fig. 17 [63]. One can see a large elongated cell that has formed and annihilated the smaller loose cells characteristic
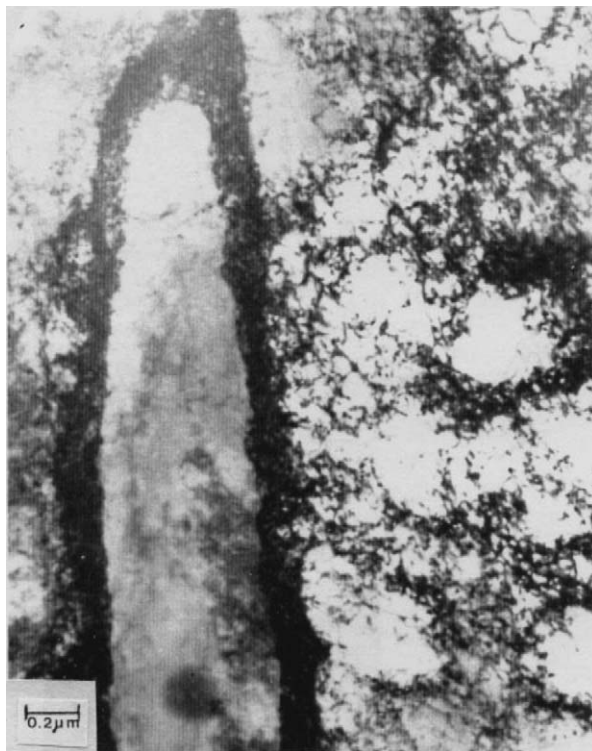
Fig. 17. TEM showing breakdown of shock-wave induced residual substructure in Ni shocked to 20 GPa and subsequently deformed in tension at ambient temperature until failure; TEM foil taken from neck portion of tensile specimen.

of shock compression (see Section 4). The quasi-static tensile response in the annealed condition, and after having been shocked is shown in Fig. 18(a). When the shocked specimen is deformed at ambient temperature, it necks immediately upon the onset of plastic deformation. However, when it is deformed at 77 K, the shock-induced structure continues to produce work hardening. This is the classical manifestation of the phenomenon of work softening as described by Longo and Reed-Hill [78]. This led Meyers [80] to propose that shock hardened Ni exhibited work softening. However, the results can be interpreted differently; Gray [81] suggested that the softening could be due to other causes and that only compressive response would identify the phenomenon incontrovertibly. This was successfully carried out by Lassila et al. [82] and is shown in Fig. 18(b). The compressive true stress–true strain curve for shock-compressed copper at ambient temperature shows a clear softening. In a similar fashion to the response of Ni, the 77 K response shows the characteristic hardening.

The shock-compressed copper was mechanically tested in compression at a strain rate of $10^{-3}\,\mathrm{s}^{-1}$ and temperature of 300 K; the conditions subjected to lower pressures (27 and 30 GPa) exhibited work softening, in contrast to the conventional
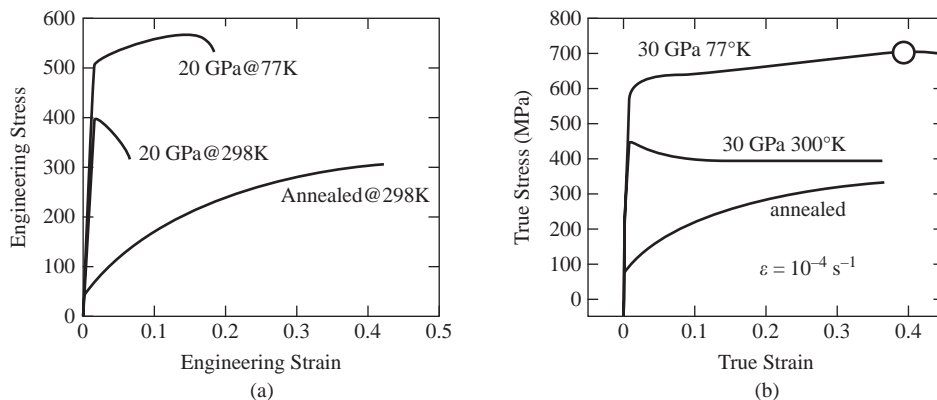
Fig. 18. Stress–strain curves for shock-recovered nickel (under subsequent tension) and copper (under subsequent compression) samples: (a) Engineering stress versus engineering strain for annealed and shock-recovered Ni. [80] (b) True stress versus true strain for annealed and shock-recovered Cu [82].

work hardening response. This work softening is due to the uniformly distributed dislocations and the formation of loose cells, evolving, upon plastic deformation at low strain rates, into well-defined cells, with a size of approximately 1 μm.

6. Detailed characterization of shock-compressed metals

We focus next on two metals that we have investigated in detail: copper and nickel. This constitutes the doctoral dissertations of Schneider [83], Cao [84,85], and Jarmakani [86] carried out in collaboration with LLNL researchers. We used two techniques: flyer-plate impact (by explosives and gas-guns) and laser-driven shock waves.

6.1. Explosively driven flyer-plate impact

We summarize here the work presented by Cao et al. [87,88] using the experimental setup shown in Fig. 1(b) and specimens pre-cooled to 90 K to minimize thermal effects. It is seen that, in spite of the care taken, there was extensive recrystallization for the higher-pressure (57 GPa) experiments. The specimens were monocrystalline Cu with two crystalline orientations: [0 0 1] and [2 2 1].

6.1.1. [0 0 1] copper impacted at 30 GPa
Fig. 19 shows the scanning electron microscope – electron channeling contrast (SEM-ECC) pictures from a 30 GPa post-shocked [0 0 1] Cu specimen. Fig. 19(a) reveals that the back surface of the sample was full of slip band traces. Fig. 19(b) provides a more detailed view of the area with slip band traces. The presence of two sets of lines, which are spaced almost exactly 90° apart, is clear evidence for {1 1 1}
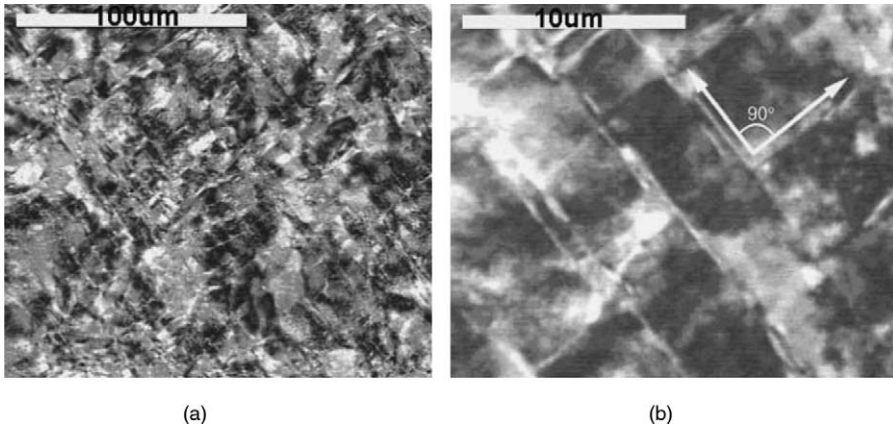
Fig. 19. SEM pictures of the residual microstructure from [001] Cu shocked at 30 GPa, driven by an HE-accelerated flyer plate. (a) Back surface of Cu sample showing traces of slip bands; (b) detailed view of slip bands forming a 90° angle [87,88].
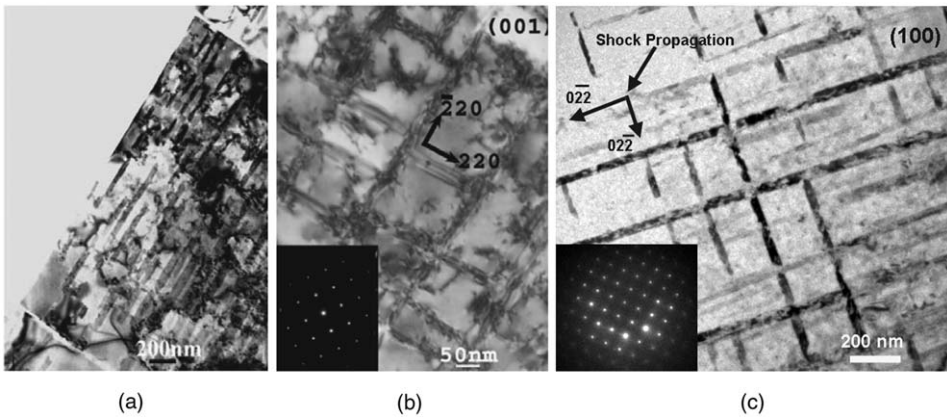
Fig. 20. (a) Stacking faults were observed in 30 GPa post-shocked [001] copper samples. (b) Two sets of perpendicular traces of the stacking faults were shown on the (001) plane when the TEM electron beam direction is $B = [001]$; (c) detailed view of the stacking faults [87,88].

traces on the plane of observation, (001). The microstructure shown by TEM for the same specimen (not shown) confirms that the deformation markings are slip bands and stacking faults. Fig. 20(a) shows traces of the stacking faults. The thin foil has straight ''boundaries'' resulting from fracture along the slip bands, which were also found by SEM [as in Fig. 20(a)]. Fig. 20(b) shows the two sets of stacking faults as [$\bar{2}$20] and [220] traces in the (001) plane when the TEM electron beam direction is $B = [001]$. It seems that the stacking faults in [$\bar{2}$20] direction were formed before the [220] ones, because they are continuous, while the [220]

stacking faults are segmented. The occurrence of stacking faults is comparable to that found by Meyers and co-workers [37] on laser-induced shock compression of monocrystalline copper.

Very little work has been done using TEM to provide the three-dimensional (3D) picture of microstructural evolution during plate impact. Fig. 20(c) reveals the microstructure along the [1 0 0] crystal orientation shocked to 30 GPa. The [1 0 0] crystal orientation is perpendicular to the [0 0 1] shock direction ((0 0 1) shock-front plane). Stacking faults similar to the ones on the (0 0 1) plane were observed on the (1 0 0) plane [Figs 20(a) and 20(b)], which may indicate the stacking faults are distributed throughout the sample for the 30 GPa case. The traces of these stacking-fault packets form an angle of 90°, which is exactly the expected angle. Later, in Section 7 (Fig. 51(a)), a montage is presented.

6.1.2. [2 2 1] copper impacted at 30 GPa

Fig. 21 shows a SEM–ECC picture for the [2 2 1] orientation. At higher magnification (not shown), the details are illustrated more clearly. Two traces of slip bands are present with an angle of 56°. They are the traces of {1 1 1} planes on (2 2 1). Although the substructure of the [2 2 1] copper shocked at 30 GPa is full of bands, the morphology of these bands varies throughout the sample. The formation of similar bands in shocked samples has been described by Gray and Huang [89]. Microbands having widths of 20–30 nm were found within the larger bands. Fig. 22(a) shows the regular slip band morphology. In Fig. 22(b), slip bands were found inside some larger bands.

The microstructure on the (1 $\bar{1}$ 0) plane in the 30 GPa impacted [2 2 1] sample is shown in Fig. 22(c). Similar bands as shown in Fig. 22(a) were also observed. These bands align with [$\bar{1}$ 1 2] orientation, which indicates that they might be the traces of (1 1 1) planes on (1 1 0). The basic difference with the [0 0 1] crystal is that two (or more) systems are simultaneously activated in the former, whereas

Fig. 21. SEM–ECC picture for 30 GPa shocked [2 2 1] Cu samples: front surface of the sample perpendicular to the shock propagation direction [87].

(a)   (b)

(c)
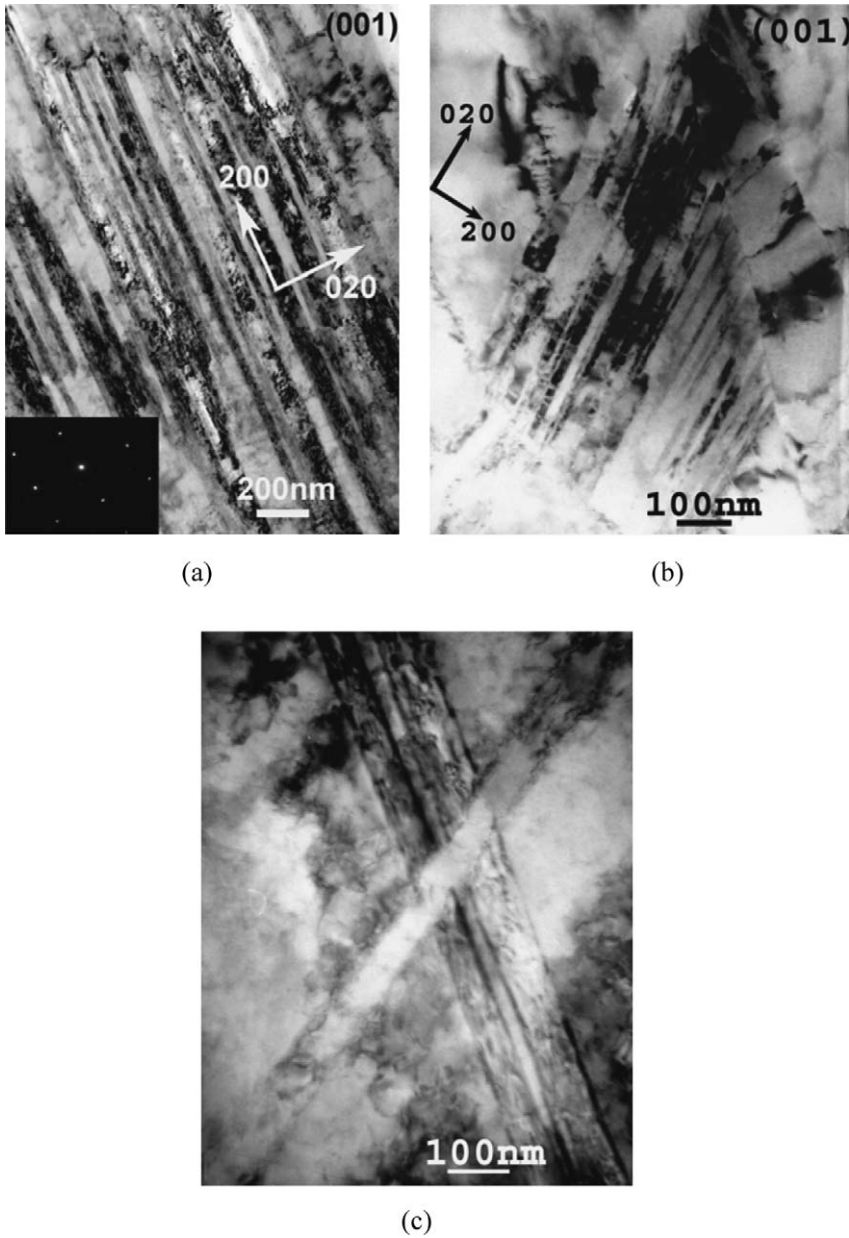
Fig. 22. (a) Regular slip bands in Cu; (b) the formation of bands when electron beam direction is $B = [\bar{0}01]$. Slip bands were formed inside those bands; (c) two sets of slip bands interact with each other [87].
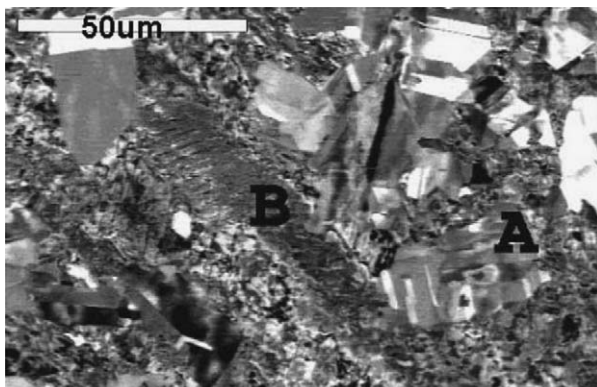
Fig. 23. SEM image of 57 GPa post-shocked copper sample with [0 0 1] orientation [87].

Figs 22(a) and 22(c) show primarily one trace. In contrast with [0 0 1], one slip system is highly activated with minor activity in the cross-slip system.

6.1.3. *[0 0 1] copper impacted at 57 GPa*

SEM–ECC analysis shows that the shock-induced structures of the surface perpendicular to the shock propagation direction (Fig. 23) consists of a mix of recrystallized grains (area A in the picture), and bands (area B) with a width of 15–16 μm. TEM confirms that the structure is not uniform. Microtwins, dislocation tangles, deformation bands, and slip bands are seen in the regions. The diversity of the post-shocked microstructures was induced by the high shock pressure and post-shock heating. Microtwins were observed throughout the sample [Fig. 24(a)]. The electron beam direction is [0 1 1]; they have a ($\bar{1}\,\bar{1}$ 1) habit plane, whose perpendicular is marked in figure. The sizes of these microtwins vary from 80 to 180 nm. Murr [18] and Johari and Thomas [8] showed that twinning is a favored deformation mechanism under shock loading. This is treated in Section 6.3, where a formal criterion is presented.

Fig. 25(a) shows the general view near the back surface of the specimen (foil parallel to shock-front plane). A shear band with a width of about a 1.5 μm crosses the foil. Compared with the slip bands around it, this shear band is larger and breaks the other slip bands. The microbands in Fig. 25(a) have distinct characteristics. The vertical bands are larger than the horizontal ones, whereas the number of horizontal ones is much higher than that vertical ones. Fig. 25(b) is a detailed image of these slip bands. Two sets of slip bands having a width of about 0.5 μm are shown. The direction of vertical slip bands was identified as [1 $\bar{1}$ 2], which might be the trace of a ($\bar{1}$ 1 1) plane. The horizontal bands seem to be cut by the vertical ones and recovery effects appear in these bands. By measuring the distances between the repeated structures in both Figs 25(a) and 25(b), we found that they have the same width of around 500 nm. The periodicity of the features of both the dislocations and bands is remarkable. We speculate that these dislocation features are due to the recovered slip traces seen in Fig. 25(a).

(a)
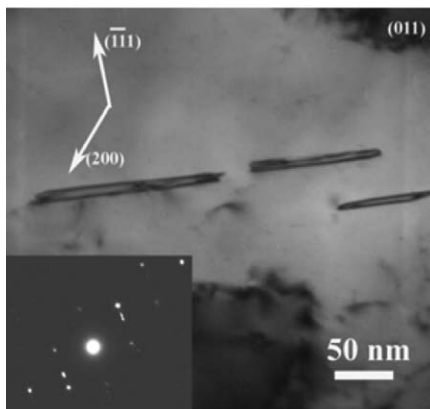
(b)

Fig. 24. Microtwins in 57 GPa post-shocked [0 0 1] copper samples: (a) image of microtwins; (b) microtwins with the habit plane of ($\bar{1}\,\bar{1}\,\bar{1}$) shown at the electron beam direction of (0 1 1) [87].

Deformation bands are shown in Fig. 25; these localized shear bands undergo thermal recovery in places [Fig. 25(c) and 25(d)]. Between these bands, there are dislocation tangles and in some places the dislocation density is very high. The dislocation density was lower and the arrays were extended in the second thin foil along the shock direction. Mughrabi et al. [90] found some dislocation cell structures very similar to our observations, but they are quite unlike the cells observed by other investigators (e.g., Johari and Thomas [8]). Gray and Follansbee [91] concluded that increasing peak pressure or decreasing pulse duration (dwell
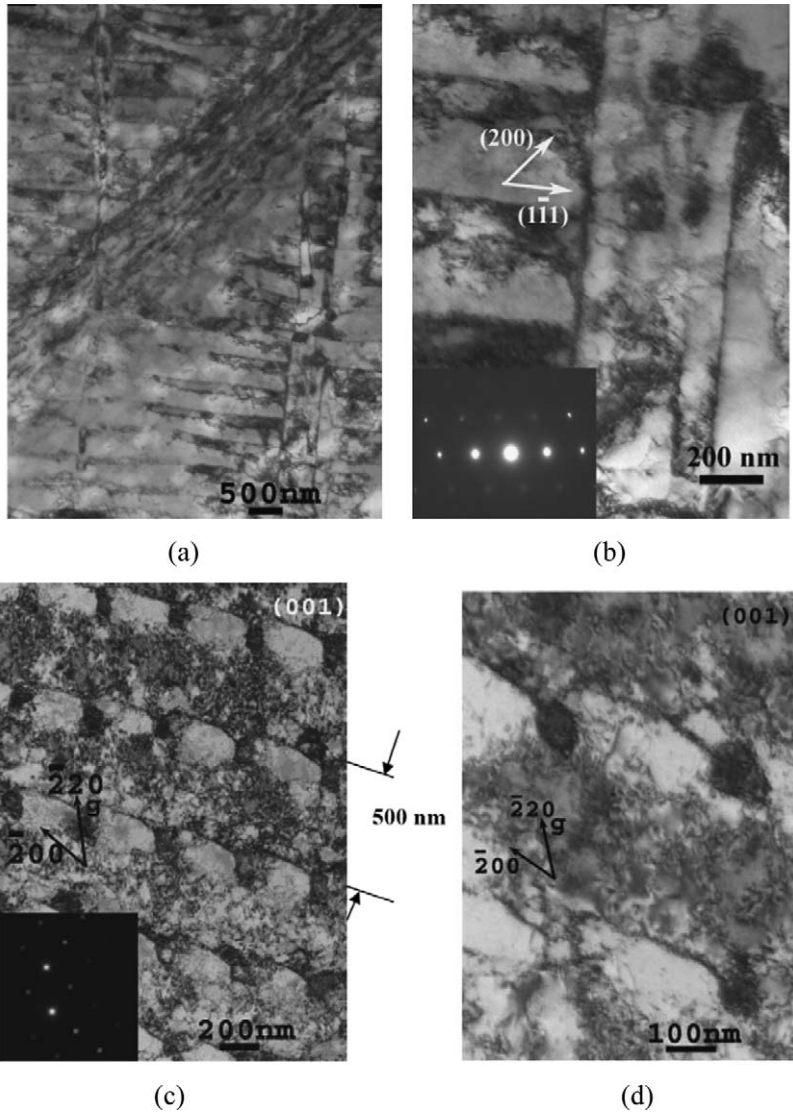
Fig. 25. TEM of 57 GPa post-shocked [0 0 1] copper samples: (a) overview of the sample (×10 K) showing shear bands; (b) slip bands; (c) bands that underwent recovery; (d) detail of recovered band from (c) [87].

time of pulse) decreased the observed dislocation cell size and increased the yield strength. The dislocation cells were extended and, therefore, showed some deformation characteristics. Murr [18] measured the dislocation cell sizes in shock-compressed Cu and Ni. For a shock pressure of 57 GPa, one would expect cell diameters around 90 nm. Cell-like structures with poorly defined cell walls are also observed in stainless steel [72]. If the shock-pulse duration is low, the

substructures are more irregular because there is insufficient time for the dislocations generated by the peak pressure (in the shock front) to equilibrate. Other studies confirm substructure consisting of tangled dislocations in cellular arrays.

6.1.4. *[2 2 1] copper impacted at 57 GPa*

The [2 2 1] copper samples shocked at 57 GPa were fully recrystallized. This recrystallization is consistent with post-shock cooling calculations conducted by Cao et al. [88]. For 57 GPa, the calculated residual temperature is 420 K. Although this is sufficient for recrystallization at long times, the post-shock cooling effectively returns the temperature to 300 K in 20–40 s. This would most probably not be sufficient for large-scale recrystallization. Cao et al. [88] proposed that shear localization can lead to temperature rises of up to 500 K above the predictions for shock compression/isentropic release.

6.2. Laser shock compression of copper

The principal results obtained by Meyers et al. [37] and Schneider et al. [92,93] are summarized here. Two orientations of single-crystal copper were investigated: [1 0 0] and [1 3 4]. The experiments were done on the Omega laser at the Laboratory for Laser Energetics (LLE) at the University of Rochester in New York. The high-power laser pulse was used to launch a strong shock into the Cu sample, which evolved into a decaying blast wave. The results from radiation–hydrodynamic simulations give the resulting pressure versus position in the sample, shown in Fig. 26.
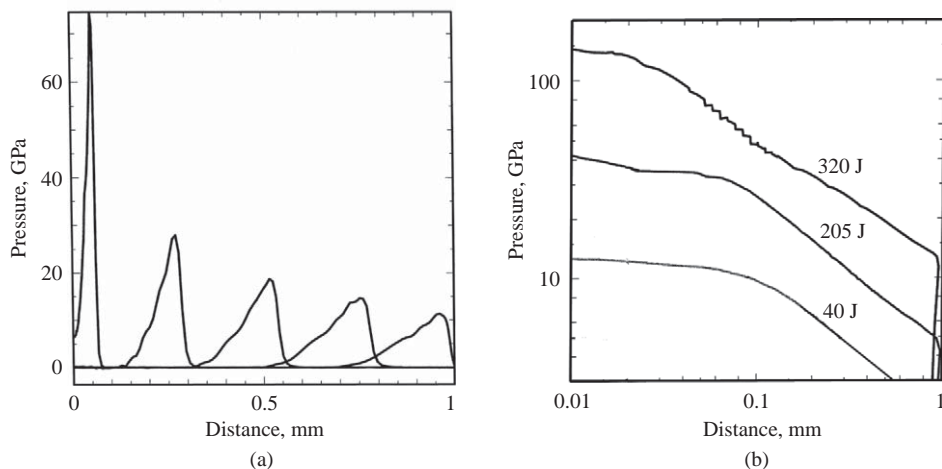

Fig. 26. (a) Simulated pressure profiles as a function of distance from the energy deposition surface for a laser energy of 200 J; (b) Maximum pressure as a function of distance from the laser driven surface for three laser energies. In all cases, the laser wavelength was 351 nm, pulse shape was 3 ns square, and the laser spot size on target was ∼2.5 mm in diameter [37].

Fig. 26(a) shows the decay of the shock pressure generated by an initial laser energy of 200 J, pulse shape of 3 ns square, and spot size (diameter) of ~2.5 mm. As the pulse attenuates, its length increases. The initial duration of the pulse is approximately 10 ns. It can be seen that the pressure is not maintained during the propagation of the pulse; the decay of the maximum pressure for pulses with laser energies of 40, 205, and 320 J is shown in Fig. 26(b).

   The shock strength at the surface of the Cu crystal can be extracted from the laser energy, pulse length, spot size, using hydrocode calculations. This can be verified by VISAR measurements. Due to the short duration of the shock created by the 3 ns laser pulse, the decay in the specimen is very rapid as shown by calculated pressure profile. Snapshots of these pressure profiles at various times up to a depth of 1 mm are shown in Fig. 26(a) for a laser energy of 200 J. The amplitude of the pressure wave in the sample decays substantially and the pulse duration broadens as a function of distance. Fig. 26(b) shows the decay of the maximum pressure in the specimens at these three laser energy levels.

6.2.1. TEM of pure copper

For the [0 0 1] orientation, shock experiments at 12 and 20 GPa pressures create a cellular organization with a medium density of ½[1 1 0]-type dislocations. The average cell size is between 0.2 and 0.3 μm for the 20 GPa case. Qualitatively, these results confirm previous observations, albeit at a pulse duration that is lower by a factor of 10–100 than that applied by Murr [18,70,73,94]. Fig. 27 shows a plot of that data. The predicted cell size from Murr's data, at a pressure of 12 GPa, is 0.4 μm. One interesting feature is the observation of a large number of dislocation loops. For example, loops as small as 25 nm and as large as 250 nm are indicated in
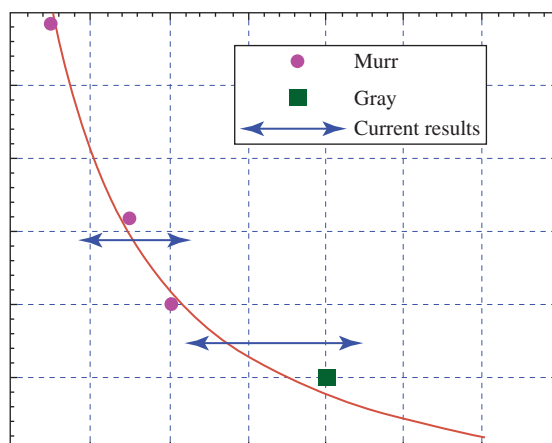
Fig. 27. Cell size as a function of pressure for shock-loaded copper [37]. Adapted from Murr [40] and Gray [20].

Fig. 28(a). Given the density of loops observed, far greater than that observed in undeformed Cu, we suggest that loop nucleation is an essential component of laser-induced shock compression. This is consistent with the mechanism of plastic deformation presented in Section 2.3 and schematically shown in Fig. 28(b). This mechanism for dislocation generation at the shock front, based on the nucleation of dislocation loops and their expansion behind the front, is still evolving.
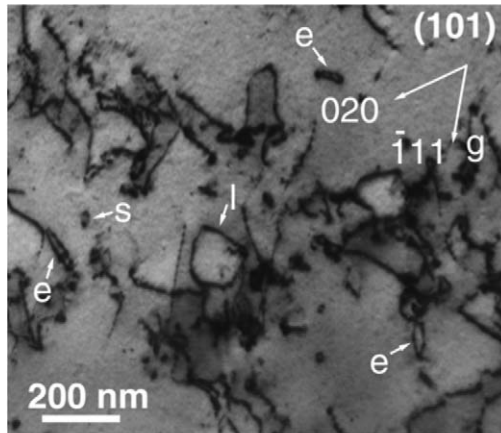
(a)
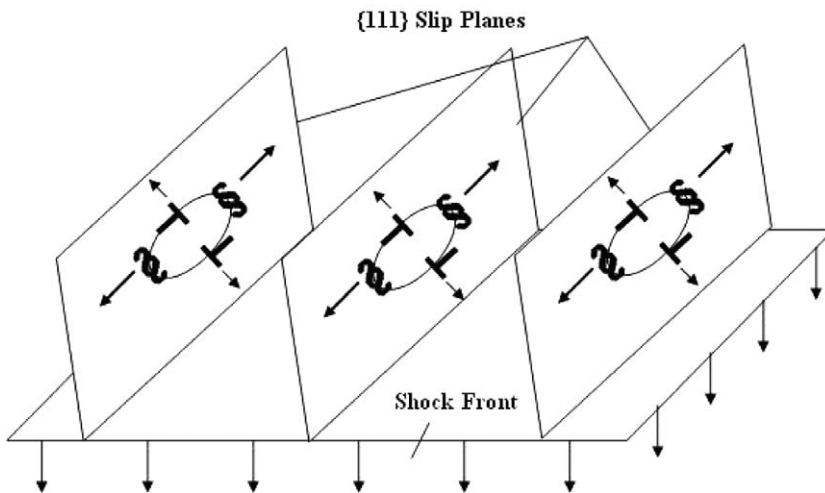
(b)

Fig. 28. (a) Observation of numerous loops in the 40 J shocked Cu specimens. The different sizes (l = large; s = small) and shapes (e = elongated) of the high density of loops are indicated in $B = [\bar{1}01]$. (b) Nucleation of dislocation loops behind the shock front [93].
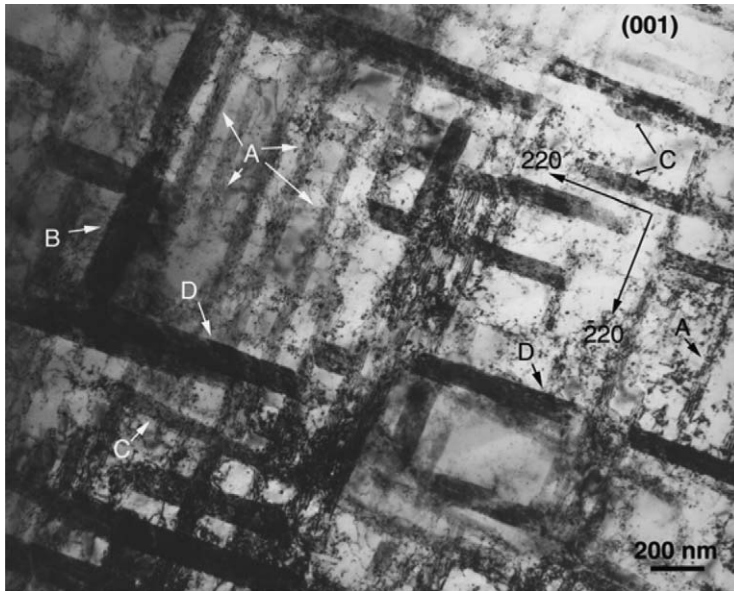
Fig. 29. Four sets of stacking faults (marked as A, B, C, D) are observed in [0 0 1] Cu at 200 J (20 GPa):
Variant A exhibits the highest density of occurrence, $g = 200$, $B = [0 0 1]$ [37].

A laser energy of 200 J (40 GPa initial pressure) created dense dislocation tangles and stacking faults. There are no readily discernible dislocation cells, but four variants of stacking faults are observed. These traces are analogous to previous observations by Murr [18,73]. The features are significantly different than the dislocation cells observed at the lower energy. These traces have orientations $\langle 2 2 0 \rangle$, as shown in Fig. 29.

Single-crystal copper samples with [$\bar{1}$ 3 4] orientation were shocked at energies of 70 and 200 J corresponding to initial pressures of 20 and 40 GPa. The specimens shocked at 20 GPa contained a well-defined cellular network comprised of $1/2 \langle 1 1 0 \rangle$ dislocations with a slightly larger (0.3–0.4 μm) average cell size (see Fig. 30), as compared to the [0 0 1] orientation. The dislocation density is on the order of 10^{13} m^{-2}. The cells are comprised primarily of three dislocation systems: (1 1 1)[$\bar{1}$ 0 1], (1 1 1)[1 $\bar{1}$ 0], and ($\bar{1}$ 1 1)[1 0 1].

At the higher energy of 200 J for the [$\bar{1}$ 3 4] orientation, the deformation substructure continued to be cellular, albeit with a finer (0.15 μm) average cell size and a significantly higher dislocation density, 10^{14} m^{-2} [Fig. 30(b)]. This is in direct contrast to the mechanism change observed in [0 0 1]. Again, the three slip systems previously described dominate the deformation substructure. A large number of loops are also visible. These were found to contribute to the cell walls and were often commonly found within the cells.

The difference observed between the defect substructure of the [0 0 1] and [$\bar{1}$ 3 4] orientations is due to the number of activated slip systems. Because of the
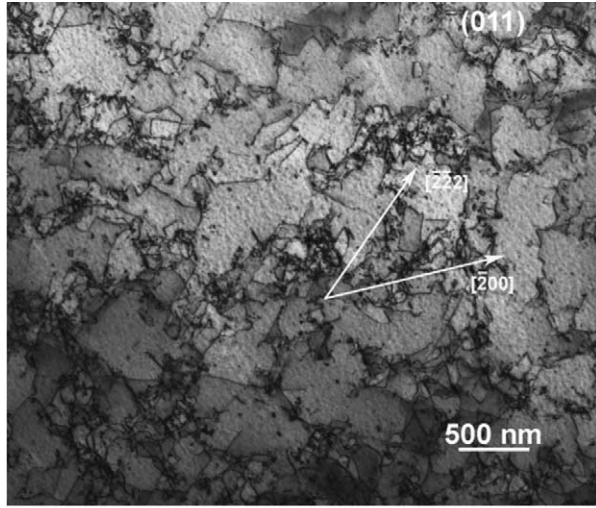
(a)
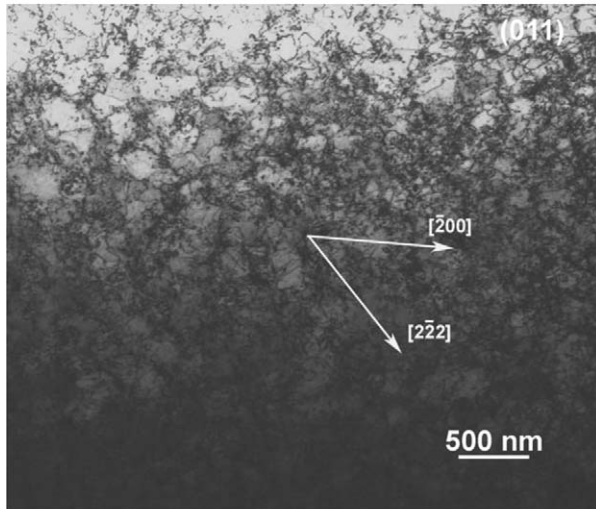
(b)

Fig. 30. (a) Defect substructure of monocrystalline copper with orientation [$\bar{1}$ 3 4], shocked with a laser energy of 70 J. Probed on the TEM with beam direction [0 1 1]; $g = [2\ \bar{2}\ 2]$; (b) defect substructure of monocrystalline copper with orientation [$\bar{1}$ 3 4], shocked with a laser energy of 200 J. Probed on the TEM with beam direction [0 1 1]; $g = [\bar{2}\ \bar{2}\ 2]$ [92,93].

symmetry of [0 0 1], multiple slip systems are activated, and interactions between dislocations are more common, which enable the defects to relax into a stacking-fault-dominated substructure. The [1̄ 3 4] orientation, consisting of dislocations with limited mobility and interaction, continues to form cells as the relaxed substructure to higher-pressure levels.

6.2.2. Pressure decay effects in pure copper

Figs 31(a)–31(c) show the dislocation cells for a laser irradiation energy of 200 J at three locations: A, C, and E, corresponding to distances into the sample of 0.25, 1.25, and 2.25 mm (see Fig. 3 in Ref. [92]). The decay in pressure, shown in Fig. 26, is accompanied as expected by an increase in cell size and decrease in dislocation density. The average cell sizes are: 0.14 μm for specimen A [Fig. 31(a)]; 0.22 μm for specimen B (at a distance of 0.75 mm from the driven surface, not shown); 0.41 μm for specimen C [Fig. 31(b)], 0.76 μm for specimen D (at a distance of 1.75 mm, not shown), and 1.43 μm for specimen E [Fig. 31(c)]. The dislocation densities decrease from $10^{14}\,\mathrm{m}^{-2}$ at the front to $10^{11}\,\mathrm{m}^{-2}$ at position E. In Fig. 32(a), the cell sizes as a function of distance from the laser irradiated surface are plotted for the three energies. The cell sizes vary consistently with the three energy levels. Fig. 32(b) shows that the cell size and pressure correlate at different locations within the specimen.

6.2.3. Copper–aluminum alloys

As previously mentioned, the addition of small amounts of aluminum ($<7\,\mathrm{wt.\%}$, the solubility limit) lowers the SFE of copper, which is approximately $78\,\mathrm{mJ/m}^2$. Early work by Johari and Thomas [8] demonstrated this effect on the defect substructure in copper–aluminum alloys. In this section, a detailed analysis of the effect of SFE on the threshold pressure for twinning is presented. Systematic differences were observed by transmission electron microscopy in the deformation substructures of the different compositions: copper–2 wt.% aluminum (Al) (4.2 atomic percent) and copper–6 wt.% Al (12.6 atomic percent). The experimentally obtained stacking-fault energies of the Cu–2 wt.% Al and (Cu–6 wt.% Al) are 37 and $5\,\mathrm{mJ\,m}^{-2}$, respectively.

Both pressure and crystal orientation significantly affected the deformation substructures of laser-shocked Cu–2wt.% Al. The samples with [0 0 1] orientation shocked at 70 J (20 GPa initial pressure) had regular cells with an average size of 250 nm and cell wall thickness of 50 nm. The average dislocation line length was considerably longer, 150 nm, and the dislocation density was on the order of $10^{14}\,\mathrm{m}^{-2}$. The dislocations were also observed to gather on the primary planes. The dislocation substructure for this condition (70 J) was made of the eight primary slip systems.

In the Cu–2 wt.% Al with [0 0 1] orientation and shocked at 200 J, stacking faults were readily observed as the dominant defect substructure (see Fig. 20 in Ref. [87]). Because of the 2 wt.% addition of aluminum, the SFE is nearly half that of pure copper, and one would expect to observe twinning. However, this is not the case. Instead, four stacking-fault variants are observed. These stacking faults are similar to those observed for pure copper (Fig. 29). The faults are well-defined with clean boundaries having a regular spacing of 250 nm.
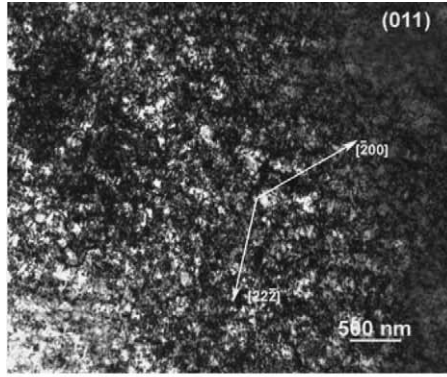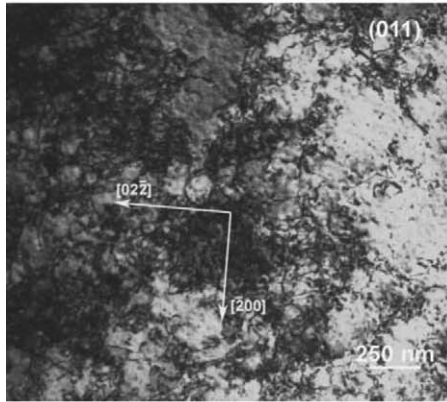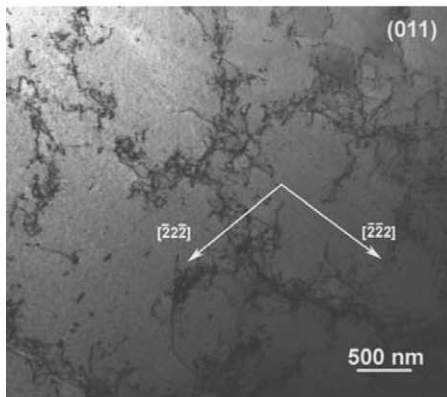
Fig. 31. TEM images of the defect substructures showing the pressure decay effects of [$\bar{1}$ 3 4] Cu at different distances from the laser-driven surface at $E_{Laser} = 200\,J$ (for each image, the TEM beam direction $B = [0\,1\,1]$): (a) 0.25 mm, $g = [2\,2\,\bar{2}]$; (b) 1.25 mm, $g = [0\,2\,\bar{2}]$; (c) 2.25 mm, $g = [\bar{2}\,2\,\bar{2}]$ [92].
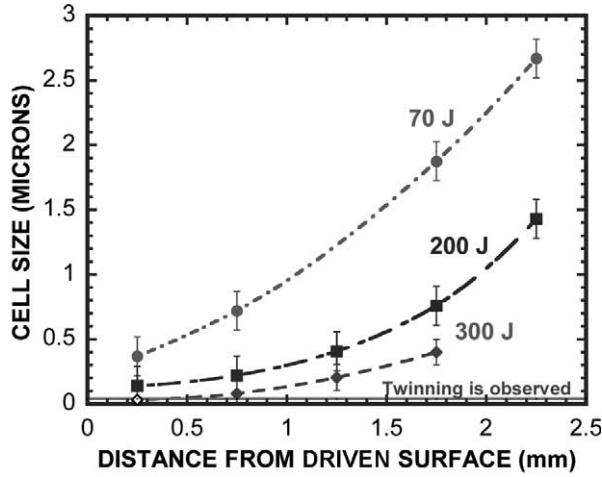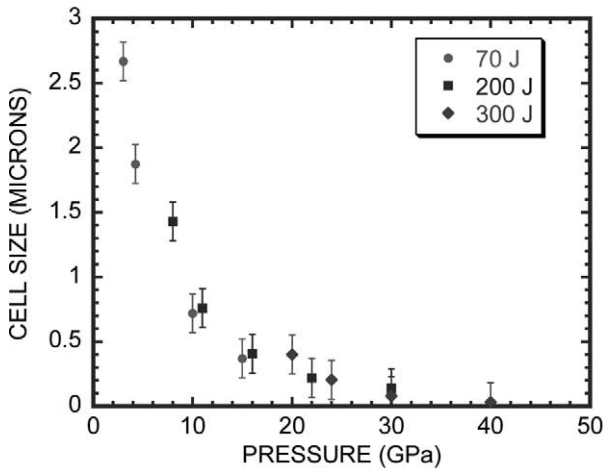
Fig. 32. (a) Cell size as a function of distance from the laser driven surface for the $[\bar{1}\,3\,4]$ crystal orientation at three initial energies: 70, 200, and 300 J. Twinning is observed when dislocation cell sizes fall below an average size of $0.05\,\mu m$ represented by the bottom line; (b) cell size as a function of estimated pressure for the three energy levels [92].

The Cu–2 wt.% Al with $[\bar{1}\,3\,4]$ orientation was observed to have a substantially different defect substructure than pure copper or Cu–2wt.% Al with $[0\,0\,1]$ orientation. The effects of the change in SFE were generally more pronounced. The dislocations were arranged in planar arrays. The defect substructure consisted of long dislocation lines as shown in Fig. 33. The dislocation line length averaged
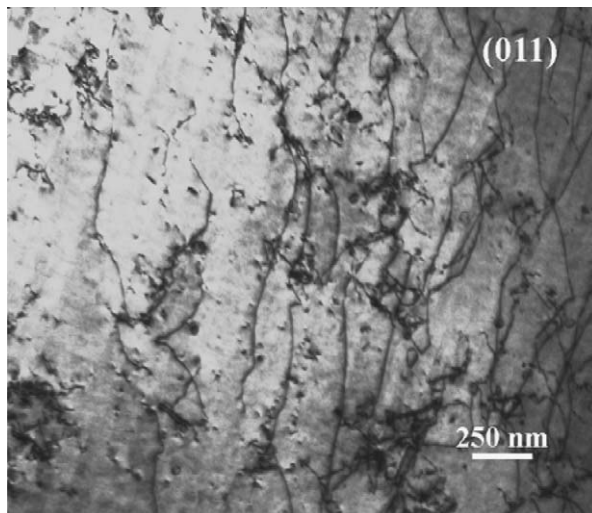
Fig. 33. Bright field images of Cu–2wt.% Al shocked at $E_{Laser} = 70$ J (20 GPa) along the $[\bar{1}\,3\,4] \leftarrow$ direction, and imaged with $B = (0\,1\,1)$ and $g = [0\,2\,\bar{2}]$ for all conditions: Specimen B ~ 0.75 mm from the driven surface [93].

500 nm and the dislocation density was $10^{13}\,\text{m}^{-2}$. Obviously, for this condition there is one dominant slip system $[\bar{1}\,0\,1](1\,1\,1)$; the two secondary systems are also observed, but in less proportions. A number of dislocation loops are also observed.

Cu–2wt.% Al with $[\bar{1}\,3\,4]$ orientation shocked at 200 J exhibited twinning (specimen A, ~ 0.25 mm from the laser-driven surface, Fig. 34). Two variants are observed. It appears that the larger twin may act as the nucleation site for the second twin. The twins were found in a relatively low proportion, but are the systems predicted by Schmid factor calculations. The twins varied in size and proportion with the primary variant, $(1\,1\,1)[\bar{2}\,1\,1]$, having an average length of 4 μm and a width of 20–30 nm. The secondary variant, $(1\,\bar{1}\,1)[\bar{1}\,\bar{1}\,\bar{2}]$, occurred in greater numbers, but with shorter lengths with an average of 2 μm. We expected that a co-secondary twinning variant, $(1\,1\,\bar{1})[1\,1\,\bar{2}]$, would also be found, but the occurrence of this system was relatively rare. This suggests that the sample may have been slightly misaligned from the $[\bar{1}\,3\,4]$ loading axis, and thereby favored the two observed twinning systems having higher Schmid factors than calculations indicate. A high density of dislocations was also observed (not shown here).

The defect substructure for all energies in Cu–6 wt.% Al with $[0\,0\,1]$ orientation consisted of either stacking faults or dislocations since, for this system, the SFE is less than $5\,\text{mJ}\,\text{m}^{-2}$. The dislocation structure consists of large planar arrays and regions of dislocation pileup since the low SFE inhibits cross-slip. Many of the dislocations observed were Shockley partials: $\{1\,1\,\bar{1}\}$ $1/6\langle 1\,1\,2\rangle$. The defect substructure was primarily made up of planar arrays of dislocations and had a dislocation density on the order of $10^{13}\,\text{m}^{-2}$ and a line length of 500 nm. The planar
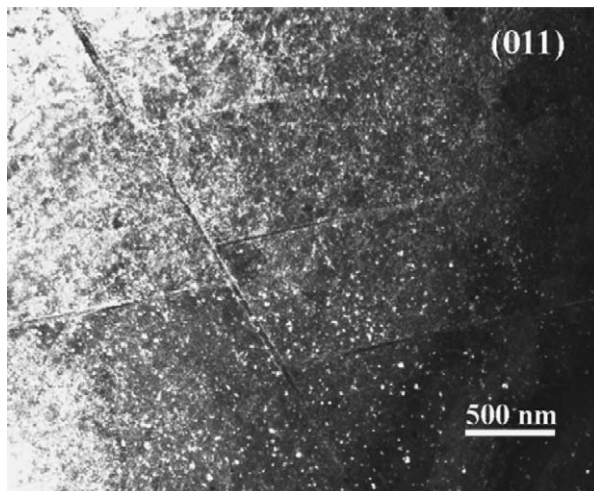
Fig. 34. Bright field images of Cu–2wt.% Al with [$\bar{1}$ 3 4] orientation shocked at $E_{Laser} = 200\,J$ (40 GPa) imaged with $B = (0\,1\,1)$ and $g = [0\,2\,\bar{2}]$ for all conditions: Specimen A $\sim 0.25\,mm$ from the driven surface [93].

arrays were spaced at a distance of 1 μm. Stacking faults and stacking-fault tetrahedra were also observed. The fault spacing was equivalent to the distance between planar arrays (1 μm).

For the Cu–6 wt.% Al with [0 0 1] orientation and laser shocked at 200 J, the defect substructure was predominantly stacking faults [Figs 35(a)–35(c)]. The stacking faults had a width of 100 nm, length of 1 μm, and spacing of 400 nm. The areal density was $0.84 \times 10^5\,m^{-1}$. Dislocations were also observed throughout the specimen, typically near the fault boundaries. For the [$\bar{1}$ 3 4] orientation of the Cu–6 wt.% Al, three variants of stacking faults were observed in the 70 J condition with one system preferred. Dislocations were also observed. The stacking-fault width was 250 nm on average and the spacing 300 nm. The areal density was on the order of $0.1 \times 10^5\,m^{-1}$. Dislocations were arranged in planar arrays and tangles with a density of $10^{13}\,m^{-2}$. The dislocation line length and planar spacing was about 1 μm and 250 nm, respectively.

The Cu–6 wt.% Al [$\bar{1}$ 3 4] specimens shocked at 200 J contained a residual defect substructure similar to the 70 J specimens. Partial dislocations dominate the defect substructure, which comprised a dislocation density of $10^{13}\,m^{-2}$ and an average line length of nearly 1 μm. The dislocations are preferentially aligned along specific planes with a spacing of 1 μm and there is one primary slip system, [$\bar{1}$ 0 1] (1 1 1). Some stacking faults were also observed with most being aligned to [$\bar{2}$ 1 1](1 1 1).

Stacking faults typically formed at high pressures and then were found to decay into either cells or planar arrays of dislocations as the pressure decayed through the sample. As expected, decreasing SFE enhanced the propensity to form stacking faults for both orientations. Similarly, cells and planar arrays became more clearly
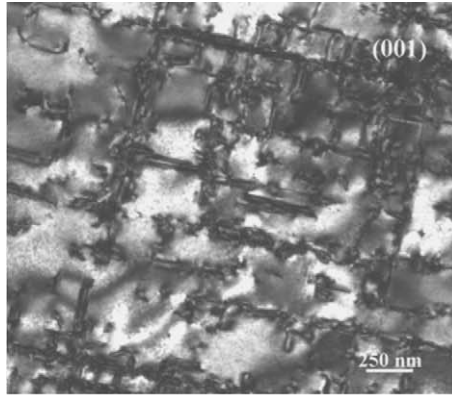
(a)
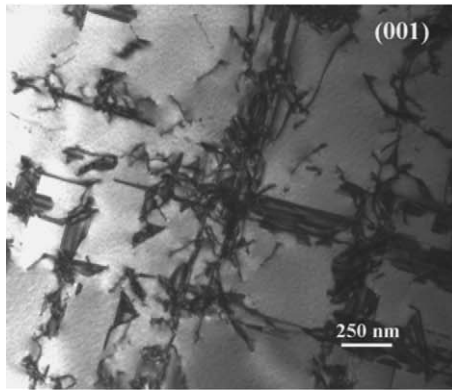
(b)
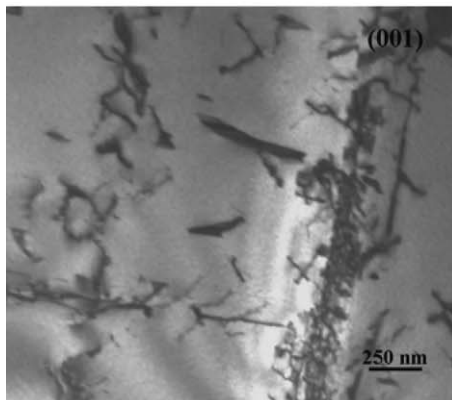
(c)

Fig. 35. Bright field images of Cu–6wt.% Al with [0 0 1] orientation shocked at $E_{Laser} = 200$ J (40 GPa) imaged with $B = (0\,0\,1)$ and $g = [0\,2\,0]$ for all conditions: (a) Specimen A ~0.25 mm from the shocked surface; (b) Specimen B ~0.75 mm from the shocked surface; (c) Specimen C ~1.25 mm from the shocked surface [93].

defined as the pressure decreased and pulse duration increased. Twinning was not readily observed in most of these conditions suggesting there may be some unresolved time dependence in twin nucleation, or more complex factors affecting twinning (Bernstein and Tadmor [41]). However, it is also possible that many of the stacking faults observed are actually nanotwins as the thickness of the twins could be so small that traditional transmission microscopy methods may be unable to resolve the changes in the structure.

The experimental results are plotted in Figs 36(a)–36(c). The positions A–D were converted into pressures through the radiation–hydrodynamics simulations. The transition from loose dislocations/cells to stacking faults/twins is approximately indicated in Fig. 36(a). Figs 36(b) and 36(c) show the change of dislocation densities and stacking-fault densities versus pressure, respectively. The energetics of loop nucleation for perfect and partial dislocations is discussed in Section 6.4. Both deformation twinning and stacking-fault formation are the direct consequence of partial dislocation loop nucleation and expansion. In the case of twinning, one has separated and prescribed arrays of partial dislocation loops on adjacent planes.

6.3. The slip–twinning transition in Cu and Ni

The primary aim of this section is to provide a constitutive description of the onset of twinning in both copper and nickel. Copper–aluminum and nickel–tungsten are also modeled. The parameters affecting slip and twinning will be discussed first, followed by modeling of the onset of twinning. Predictions of the model are compared to experimental work.

6.3.1. Modeling of the slip stress
6.3.1.1. Monocrystalline Cu and Cu–Al.
The constitutive response for slip in FCC metals is well-modeled by the Zerilli–Armstrong constitutive description [28], which captures the essential physical phenomena. For monocrystalline Cu, the equation used is as follows:

$$\sigma_S = \sigma_G + C_2 f(\varepsilon)\exp(-C_3 T + C_4 T\ln(\dot{\varepsilon})) + k_s d^{-1/2},\qquad(21)$$

where σ_G is the athermal component of stress, ε the strain, $f(\varepsilon)$ the work hardening factor, d the grain size, T the temperature, k_s the Hall–Petch slope, and C_2, C_3, and C_4 are constants. σ_G, C_3, and C_4 are adopted from Ref. [28] and $C_2 = 415$ MPa. The work hardening $f(\varepsilon)$ was incorporated by taking a polynomial representation of the stress–strain curve for single crystals with the $[0\,0\,1]$ and $[\bar{1}\,3\,4]$ orientations from Ref. [37]. This is the only manner by which three-stage response can be incorporated without excessive complexity. The $[0\,0\,1]$ orientation is expected to have the lowest threshold pressure for twinning of all orientations,
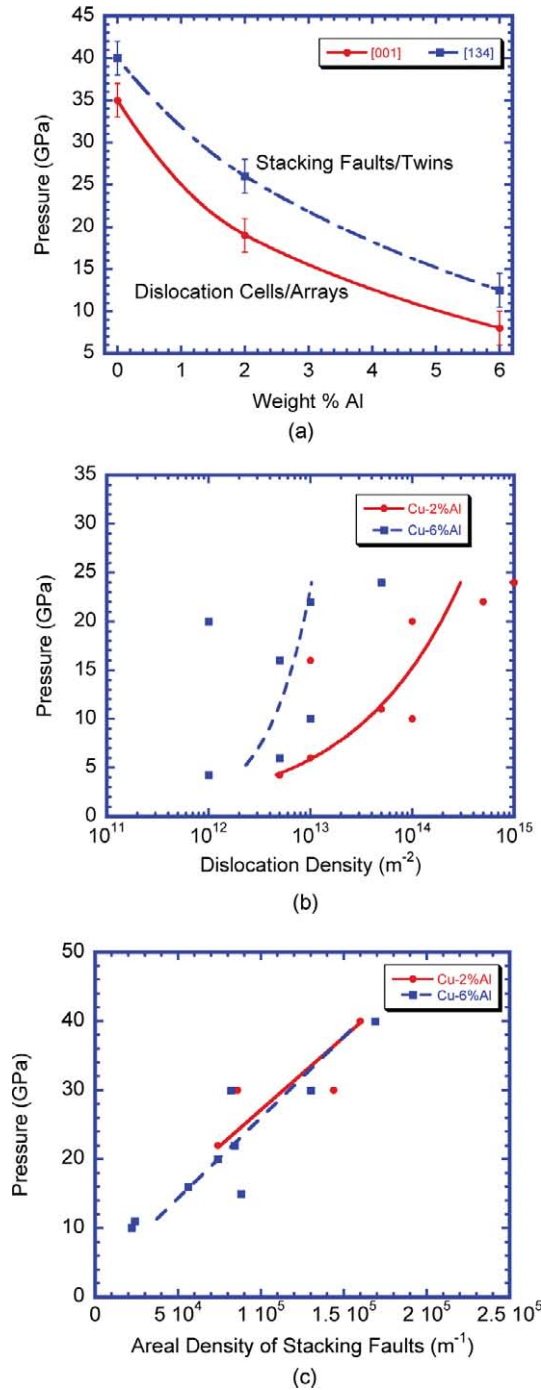
Fig. 36. Experimental results for laser-shocked Cu–Al alloys: (a) Experimentally observed transition from dislocation cells and planar arrays to stacking faults and twins as a function of composition and crystal orientation; (b) experimentally observed dislocation densities as a function of pressure and composition; (c) experimentally determined areal densities of stacking faults as a function of pressure and composition [93].

whereas [$\bar{1}\,3\,4$] should have a substantially higher threshold pressure due to its more gradual hardening. The polynomials used in these calculations are:

For [$0\,0\,1$]:

$$f(\varepsilon) = 19466.2\,\varepsilon^6 - 18522.2\,\varepsilon^5 + 7332\,\varepsilon^4 - 1582\,\varepsilon^3 + 189.5\,\varepsilon^2 - 2.4\,\varepsilon + 0.07. \tag{22}$$

For [$\bar{1}\,3\,4$]:

$$f(\varepsilon) = -6293\,\varepsilon^6 + 7441.4\,\varepsilon^5 - 3163\,\varepsilon^4 + 515.65\,\varepsilon^3 - 4\,\varepsilon^2 + 0.13\,\varepsilon^1 + 0.059. \tag{23}$$

The addition of small amounts of aluminum in copper not only lowers the SFE, but drastically influences the strength and hardness. In pure metals, dislocations are relatively mobile, but when solute atoms are added the dislocation mobility is greatly reduced. In these alloys, the solute atoms become barriers to dislocation motion and can have the effect of locking them. Substantial work has been done developing solid-solution theory for concentrated solid solutions [95–98]. The flow stress of concentrated solid solutions increases with the atomic concentration of the solute. For many systems, the following proportionality is observed:

$$\sigma_0 \propto [C_S]^m, \tag{24}$$

where σ_0 is the flow stress, and C_S the concentration of the solute, and m a parameter that is found to vary between ½ and 1. Copper–aluminum has been shown to follow this description [95] with $m = 2/3$. Therefore, we incorporated this compositional term into the modified Z–A equation as shown below

$$\sigma_s = \sigma_G + C_S^{2/3} C_2 f(\varepsilon) \exp(-C_3 T + C_4 T \ln(\dot{\varepsilon})) + k_s d^{-1/2}. \tag{25}$$

6.3.1.2. Ni. For Ni, $\sigma_G = 48.4\,\mathrm{MPa}$, $C_2 = 2.4\,\mathrm{GPa}$, $C_3 = 0.0028\,\mathrm{K}^{-1}$, $C_4 = \leftarrow$ $0.000115\,\mathrm{K}^{-1}$, and $k_s = 0.2\,\mathrm{MN\,m}^{-3/2}$ in eq. (21). A strain-hardening function is taken as $f(\varepsilon) = \varepsilon^n$ in the Z–A equation. The strain-hardening exponent, n, in the nc Ni regime was simply equated to 0 as determined by measurements carried out on the same material by Choi et al. [99]. The values of C_3 and C_4 used are those for copper [28] since data on Ni was not available. The nickel Hall–Petch slope for slip, k_s, has been established by several researchers [100–103] and Asaro and Suresh [104] compiled hardness data for nickel spanning both the micrometer and nanometer regimes. A k_s value of $\sim 0.2\,\mathrm{MN\,m}^{-3/2}$ was calculated from that set of data. Stress–strain plots of nickel with micrometer sized grains were utilized to establish C_2. The current model predicts a yield strength of $\sim 1.9\,\mathrm{GPa}$ for Ni having a grain size of 30 nm, which is in good agreement with the literature [104].

6.3.1.3. Ni–W, 13 at.%. Roth et al. [105] obtained the increase in yield stress in Ni as a result of alloying with different elements. They estimate that the flow stress of Ni increases from 100 to $\sim 450\,\mathrm{MPa}$ due to the addition of 13 at.% W. A plot of the increase in flow stress of Ni with tungsten content is shown in Fig. 37(a). The data
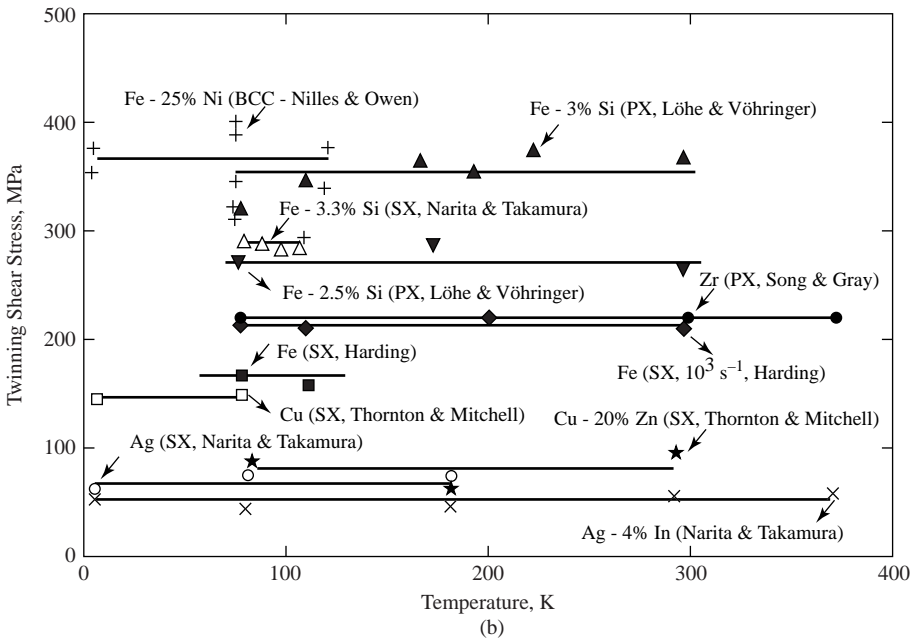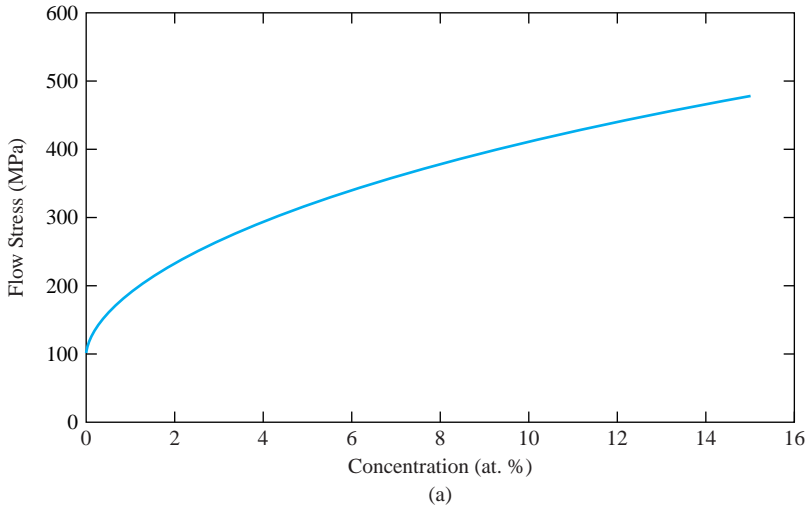
Fig. 37. (a) Slip stress of Ni as a function of the concentration of W (at.%). Adapted from Meyers et al. [106]; (b) twinning stress as a function of temperature for a number of metals – both mono and polycrystals. Adapted from Meyers et al. [106].

was extracted from work carried out on Ni having a grain size between 100 and 300 μm. The effect of solid–solution addition to the yield stress increment is as follows:

$$\Delta\sigma_{SS} = \leftarrow \sum_i \left(K_i^{1/m} C_i \right)^m, \tag{26}$$

where m is $\sim 1/2$, K_i is the strengthening constant for solute i, and C_i is the concentration of solute i (for W, $K_i = 977$ MPa at. fraction$^{-1/2}$). The Zerilli–Armstrong equation as a function of tungsten content is obtained by adding the solid–solution term into the athermal component of stress:

$$\sigma_{slip} = \sigma_G + \leftarrow \sum_i \left(K_i^{1/m} C_i \right)^m + C_2\varepsilon^n \exp(-C_3 T + C_4 T \ln\dot{\varepsilon}) + k_s d^{-1/2}. \tag{27}$$

The strain-hardening exponent, n, for the nc Ni–W samples was again equated to 0. The Z–A model predicts a yield strength of ~ 2.2 GPa for Ni–W with a grain size of 10 nm, very close to the 2.38 GPa value reported by Choi et al. [99]. We estimated the Hall–Petch, k_s, slope for Ni–W using yield strength data on Ni–W samples having grain sizes in the micrometer regime and microhardness measurements carried out on the nc Ni–W samples. A k_s value of 0.1 MPa m$^{-3/2}$ was estimated.

6.3.2. Modeling of the twinning stress

In shock loading, the dislocation arrangements are more uniform than after quasi-static deformation of the material. High SFE materials often are found to twin above a threshold pressure during shock compression whereas they may never twin at quasi-static conditions except at very low temperatures. Twinning propensity, however, increases in both modes of deformation (quasi-static and high strain rate) when the SFE is decreased. SFE can be manipulated in materials by alloying. For example, in copper, which has a relatively high SFE (78 mJ/m^2), the SFE is nearly cut in half by adding 2 wt.% Al. This effect can be correlated to the change in the electron to atom ratio (e/a) in an alloy as given by:

$$\frac{e}{a} = (1 - x)Z_1 + Z_2 = 1 + x\delta Z, \psi \tag{28}$$

where x is the atomic fraction of the solute in the alloy, Z_1 and Z_2 are the number of valence electrons for the solute and solvent atoms, respectively, and δZ equals $(Z_1 - Z_2)$.

Despite the fact that dislocation activity is directly associated with twinning, slip by dislocation motion is much more sensitive to strain rate and temperature [107–110], whereas twinning is much less sensitive to these parameters [106]. Fig. 37(b) shows the twinning shear stresses as a function of temperature for a number of metals, and clearly indicates that the twinning stress is temperature insensitive over the range considered. This trend is actually still subject to debate as results have been conflicting. In their review article on mechanical twinning, Christian and Mahajan [111] proposed that BCC metals have a negative

dependence of twinning stress on temperature, whereas FCC metals have a weakly positive dependence. In the analysis on the onset of twinning that follows, it is assumed that the twinning shear stress is insensitive to temperature, pressure (except in Section 6.5.4) and strain rate.

6.3.2.1. Grain-size and stacking-fault energy effects on twinning. The effect of grain size on the twinning stress has been found to be greater than that on the slip stress for many metals and alloys [106,111]. A Hall–Petch relationship can, thus, be ascribed to the twinning stress:

$$\sigma_T = \sigma_{T_0} + k_T d^{-1/2}, \tag{29}$$

where k_T is the twinning Hall–Petch slope (higher than the k_s slope for slip), σ_{T_0} is the initial twinning stress assumed for a monocrystal ($\lim_{d\Rightarrow\infty}(d^{-1/2}) = 0$), and d is grain size. The normal twinning stress (σ_T) used in this calculation was 300 MPa for pure copper. We assume that this critical stress remains constant. Haasen [112] carried out low-temperature tensile tests on monocrystalline Ni and observed twinning at 4.2 K and 20 K at a shear stress considerably higher than that for copper. This shear stress was estimated to be equal to 250–280 MPa, which is equivalent to a normal stress, σ_{T_0}, of 500–560 MPa.

Meyers et al. [113] conducted shock compression experiments on copper up to pressures of 35 GPa. They detected an abundance of twins for grain sizes between 100 and 300 μm, but found no traces of twinning at a grain size of ~ 10 μm. Similar results were obtained by Sanchez et al. [74]. Vöhringer [95] established that the twinning Hall–Petch slope for copper, k_T, is $\sim 0.7\,\text{MN m}^{-3/2}$, which is significantly higher than that for slip, $k_s \sim 0.3\,\text{MN m}^{-3/2}$. In the present modeling of nickel, we assume that k_T for nickel is three times k_s. Thus, a k_T value of $0.6\,\text{MN m}^{-3/2}$ is used for Ni.

Solid–solution strengthening and SFE effects are incorporated into the slip–twinning model as a result of alloying with tungsten. The addition of solute atoms hinders the movement of dislocations, hence, creating a strengthening effect [114]. Alloying also significantly reduces the SFE, γ_{SF}. For instance, it has been shown that the SFE of copper decreases by nearly 50% by the addition of 2 wt.% Al [115]. This effect is related to the change in the electron to atom ratio (e/a). Partial dislocations are under elastic equilibrium, where the repulsive forces between the bounding partials are balanced by the forces needed to minimize the stacking-fault area and maintain a minimum energy configuration. Thermodynamically, alloying can alter the difference in the free energy between the HCP (stacking-fault ribbon) and FCC structures and, therefore, the energy of the ribbon between two partials as well as their separation.

The twinning stress, τ_T, is shown to vary with SFE. Venables [116,117] and Vöhringer [118,119] performed extensive analyses on the twinning stress for a number of alloys and found that it varies with the square root of the SFE:

$$\tau_T = k\left(\frac{\gamma_{sf}}{G b_s}\right)^{1/2}, \tag{30}$$
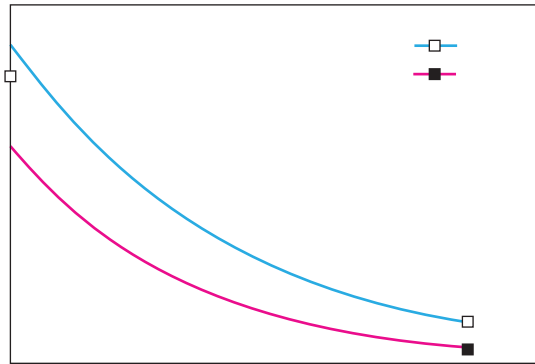
Fig. 38. Calculated critical shock pressures for the transition from slip to twinning for Cu-Al alloys as a function of increasing aluminum concentration.

where k is a proportionality constant and G is the shear modulus and $\boldsymbol{b}_s$ is the Burgers vector. A good fit is obtained for copper and nickel alloys with a k value of 6 and 6.8 GPa, respectively. Recently, there have been attempts to obtain twinning stresses by atomistic methods. The atomistic studies point to the relevance of the SFE, but also to the need to take into account other variables, like the unstable stacking-fault and twinning energies (Berstein and Tadmor [41], Van Swygenhoven et al. [120], Ogata et al. [121], and Siegel [122]).

Fig. 38 shows the critical twinning stresses for copper and copper–aluminum alloys. The following values for stacking-fault energies were used: Cu–2wt.% Al: 37 mJ/m^2; Cu–4wt.% Al: 7 mJ/m^2; Cu–6wt.% Al: 4 mJ/m^2. The twinning stresses are calculated based on the calculated stacking-fault energies using eq. (30), neglecting the grain-size differences.

For Ni–W, the shear modulus and the SFE, γ_{SF}, as a function of W were obtained by Tiearnay and Grant [123]. For Ni–13at.% W, G = 88 GPa and the γ_{SF} = 52.5 mJ/m^2 (a decrease of 60% over pure Ni).

Assuming a twinning Hall–Petch slope three times that of slip, we obtain a k_T value for Ni–W equal to 0.3 MPa/m$^{3/2}$. Just as in the case of pure Ni, a Hall–Petch behavior accounting for the effect of grain size on the twinning stress is adopted in predicting the critical twinning transition pressure in Ni–W (13 at.%). The following expression for the twinning stress was used:

$$\sigma_T = k\left(\frac{\gamma_{sf}}{Gb_s}\right)^{1/2} + k_{T_{NiW}}d^{-1/2}. \tag{31}$$

For Ni–13 at.% W, $k = 6.8$ GPa, $k_{T_{NiW}} = 0.3$ MPa, $\gamma_{sf} = 52.5$ mJ m^{-2}, $G = 88$ GPa, $\boldsymbol{b}_s = 0.249$ nm.

6.3.2.2. *Critical pressure for slip–twinning transition.* In this analysis, we assume that the transition from slip to twinning occurs when the shear stress for twinning, τ_T, becomes equal to or less than the shear stress for slip, τ_s:

$$\tau_T \leq \tau_s. \tag{32}$$

If one uses the same conversion parameters:

$$\sigma_T \leq \sigma_s. \tag{33}$$

This is a reasonable approximation since both mechanisms are subjected to the same stress system at the shock front. Since the criterion described here is based on the critical shear stresses for slip and twinning, the pressure only enters insofar as it determines the shear stress and strain rate.

We assume the twinning stress, σ_T, to be pressure and temperature independent. (Since the pressure dependence of both σ_{slip} and $\sigma_{twinning}$ is generally taken to scale with the shear modulus, $G(P)/G_0$, then it affects slip and twinning equally, and we can ignore pressure hardening in this slip–twinning analysis.) The dependence of shock pressure on strain rate for Ni, obtained through the Swegle–Grady relationship [124], is not available in the literature. As an approximation, the strain rate versus pressure behavior of copper is adopted. The reasoning for this approximation is that Al and Cu, both FCC metals, have a strain rate response to shock pressure that is very comparable even though the SFE of Al is much higher. One would expect that the behavior of Ni should not significantly deviate from that of Al and Cu. Thus, the Swegle–Grady relationship for Ni is given as follows:

$$\dot{\varepsilon} = 7.84 \times 10^{-33} \times P_{shock}^4, \tag{34}$$

where the pressure is in Pa and the strain rate in s^{-1}.

Two separate aspects have to be considered in the analysis: (a) plastic strain at the shock front and (b) shock heating. Both plastic strain by slip (and associated work hardening) and shock heating alter the flow stress of a material by slip processes and need to be incorporated into the computation. The total (elastic + plastic) uniaxial strain, ε, at the shock front is related to the change in specific volume by:

$$\frac{V}{V_0} = e^{\varepsilon}. \tag{35}$$

The pressure dependence on strain, determined from the Rankine–Hugoniot equations, equation of state (EOS), and eq. (14) is expressed as follows [37,19]:

$$P_{shock} = \frac{C_0^2(1 - e^{\varepsilon})}{V_0[1 - S(1 - e^{\varepsilon})]^2}. \tag{36}$$

The equations modeling the associated temperature rise in Cu and Ni as a function of shock pressure are represented below, which are second-order polynomials that were generated from thermodynamically calculated data in Ref. [19]:

$$T_{shock\ Cu} = 10^{-19}\ P^2 + 2 \times 10^{-9}\ P + 295.55\ K,$$

$$T_{shock\ Ni} = 8 \times 10^{-20} \times P_{shock}^2 + 9 \times 10^{-10} \times P_{shock} + 301.5\ K, \tag{37}$$

where the pressure is in Pa and the temperature is in K. For Ni–W, the temperature rise and strain associated with a given shock pressure are determined just as outlined in the case for pure Ni.

Fig. 39(a) shows both the slip stress, σ_s (incorporating thermal softening, strain rate hardening, and work hardening) and σ_T as a function of pressure for nickel. The point at which the horizontal line determined by σ_T, eq. (31), intersects the slip stress at a given shock pressure, is defined as the critical twinning transition pressure. This transition pressure for nickel having a grain size of 30 nm was found to be $\sim$78 GPa and is consistent with the fact that twins are not observed in experiments up to pressures of $\sim$70 GPa. The twinning transition pressure for nc Ni–W, 13 at.%, having a grain size of 10 nm is illustrated in the plot in Fig. 39(b).
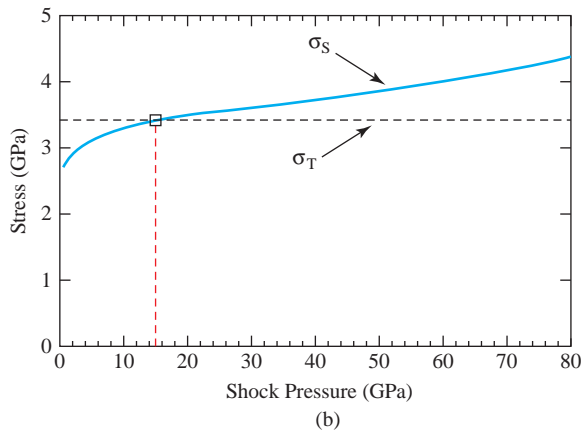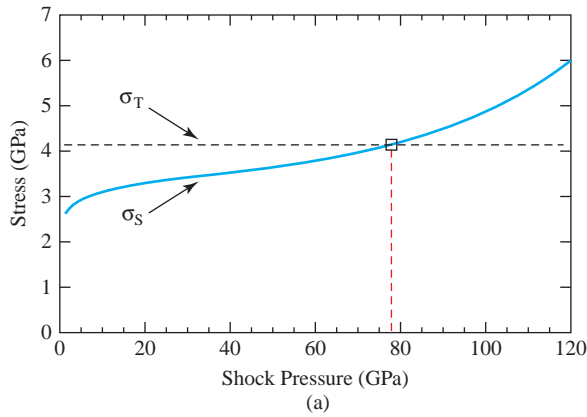

Fig. 39. (a) Slip and twinning stress versus shock pressure for nanocrystalline (nc) nickel (grain size = 30 nm); twinning threshold $\sim$78 GPa; (b) slip and twinning stress versus shock pressure for Ni–W (13 at.%) having a grain size of 10 nm; twinning transition takes place at $\sim$16 GPa.
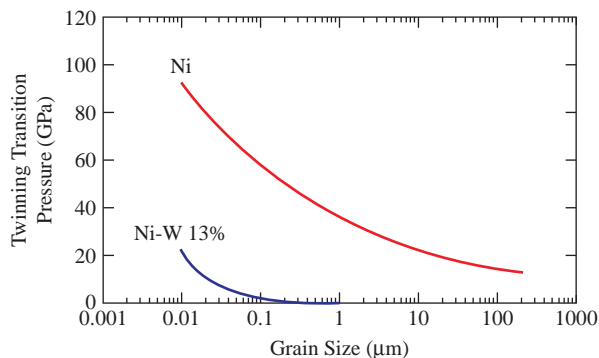
Fig. 40. Calculated twinning transition pressure versus grain size for Ni and Ni–13 at.% W.

It is equal to 16 GPa, and is consistent with experiments where twins were observed at pressures of $\sim$ 38 GPa.

The slip–twinning transition pressure as a function of grain size (micro to nanometer regime) was also calculated. The strain-hardening exponent was varied between $n = 0.5$ in the micrometer regime (as determined by fitting to stress–strain plots found in Andrade [103]) and $n = 0$ in the nanometer regime. The result, seen in Fig. 40, clearly shows the much higher transition pressure in Ni as compared to Ni–W as well as the effect of grain size on the slip–twinning transition.

6.4. Dislocation loop analysis: stacking-fault transition

The nucleation of dislocation loops was first treated by Cottrell [125] and later further developed by Xu and Argon [126], Rice [127], and others. A mechanism was also proposed by Khantha and Vitek [128] for the generation of dislocations under extreme conditions. At pressures above 3–3.2 GPa, the activation energy for loop nucleation is lower than the thermal energy; thus, nucleation becomes thermally activated, whereas under conventional deformation at ambient temperature, it is not activated. As previously mentioned, Meyers [36] proposed in 1978 that dislocations in shock compression were homogeneously generated by loop expansion. Fig. 41(a) shows shear loops generated on $\{1\,1\,1\}$ planes making an angle of $54.7°$ with the shock compression plane, $(0\,0\,1)$. Whereas the nucleation and growth of perfect dislocation loops can lead to the formation of a cellular structure after multiple cross-slip and relaxation of the dislocation configurations, the stacking-fault packets observed in shock compression above 20 GPa cannot be accounted for by this mechanism. The corresponding nucleation of partial loops is shown in Fig. 41(b).

The calculation introduced by Meyers et al. [19,129] for the energetics of nucleation of partial dislocation loops in copper was extended by Jarmakani et al. [130] to nickel. The analytical development is reproduced for the sake of clarity and continuity. The critical radius, r_c (Fig. 41), can be found from the maximum of the
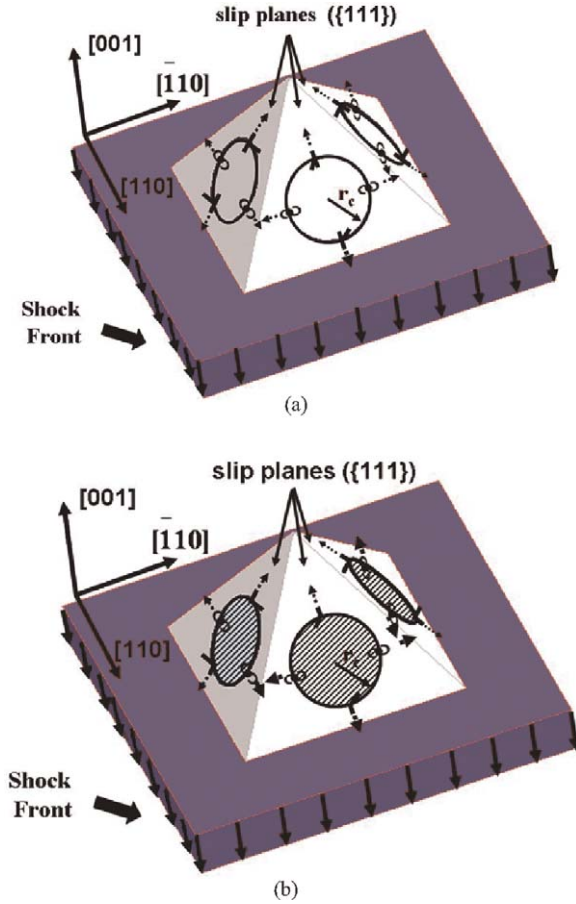
Fig. 41. Nucleation of dislocation loops along {1 1 1} slip planes behind the shock front, which is in red (propagation along [0 0 1]): (a) perfect dislocations and (b) partial dislocations ([139]).

energy versus radius curve (Kan and Haasen [96] and Hull and Bacon [131]):

$$\frac{dE}{dr} = 0. \tag{38}$$

The total energy of a perfect dislocation loop with radius r is the sum of the increase of the energy E_1, due to a circular dislocation loop (assumed to be one-half edge and one-half screw), and the work W carried out by the applied stress τ on the loop (assumed to be circular):

$$E = E_1 - W = \frac{1}{2}Gb^2 r \left(\frac{2-v}{1-v}\right) \left(\ln\left(\frac{2r}{r_0}\right)\right) - \pi r^2 \tau b, \tag{39}$$

where v is Poisson's ratio, G the shear modulus, $\boldsymbol{b}$ the Burgers vector, and τ the shear stress. The critical radius is obtained by taking the derivative of eq. (39) with respect to r and applying eq. (38):

$$r_c = \frac{Gb}{8\pi\tau}\left(\frac{2-v}{1-v}\right)\left(\ln\frac{2r_c}{r_0}+1\right) \tag{40}$$

To obtain the total energy of the partial dislocation loop [Fig. 41(b)], both the energy of the stacking fault, E_2, and work done by shear stress, W, have to be incorporated:

$$E = E_1 + E_2 - W. \tag{41}$$

Substituting the values of E_1, E_2, and W into eq. (41):

$$E = \frac{1}{4}Gb_p^2 r\left(\frac{2-v}{1-v}\right)\left(\ln\left(\frac{2r}{r_0}\right)+\pi r^2\gamma_{sf} - \pi r^2\tau b_p, \tag{42}$$

where γ_{sf} is the SFE and $\boldsymbol{b}_p$ is the Burgers vector for a partial dislocation. The critical radius is obtained by the same method:

$$r_c = \frac{G(b/\sqrt{3})^2}{8\pi[(\tau b/\sqrt{3})-\gamma_{sf}]}\left(\frac{2-v}{1-v}\right)\left(\ln\frac{2r_c}{r_0}+1\right) \tag{43}$$

For Ni, we have $v = 0.31$, $\gamma_{sf} = 130\ \text{mJ}\,\text{m}^{-2}$, and $G = 76\ \text{GPa}$ at zero pressure. G changes with pressure as follows [132]:

$$G = 76 + 1.37\ \text{P (GPa)}. \tag{44}$$

The Burgers vector; $\boldsymbol{b}_0$, at $P = 0$ is equal to $0.249\ \text{nm}$; it changes with shock pressure as:

$$\boldsymbol{b} = \left[\left(\frac{C_0^2}{2PS^2V_0}\right)\sqrt{1+\frac{4PSV_0}{C_0^2}}\left(+\frac{2S(S-1)V_0P}{C_0^2}-1\right)\right]^{1/3}b_0, \tag{45}$$

where C_0 is $4.581\ \text{km/s}$, S is 1.44, and V_0 is the specific volume of Ni (m^3/kg) at zero pressure. The shear stress, τ, assuming elastic loading can be calculated from the shock pressure through:

$$\tau = -\frac{1-2v}{2(1-v)}P_{\text{shock}}. \tag{46}$$

The calculated results are shown in the normalized plot of Fig. 42(a) (pressure and critical radius are divided by the shear modulus and Burgers vector, respectively). Evidently, the critical radius for perfect dislocations is lower than for partial dislocations at lower pressures; whereas with increasing pressure, partial dislocations become more favorable. The predicted transition pressure for Ni is $\sim$27 GPa, close to the experimentally observed twinning transition pressure,

(a)

(b)
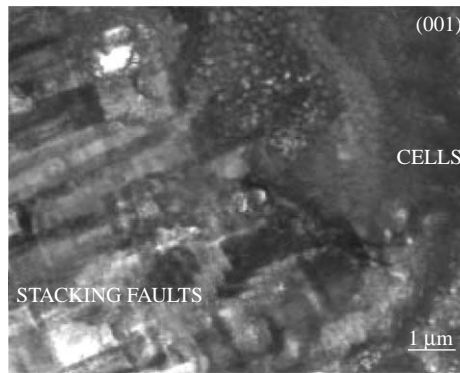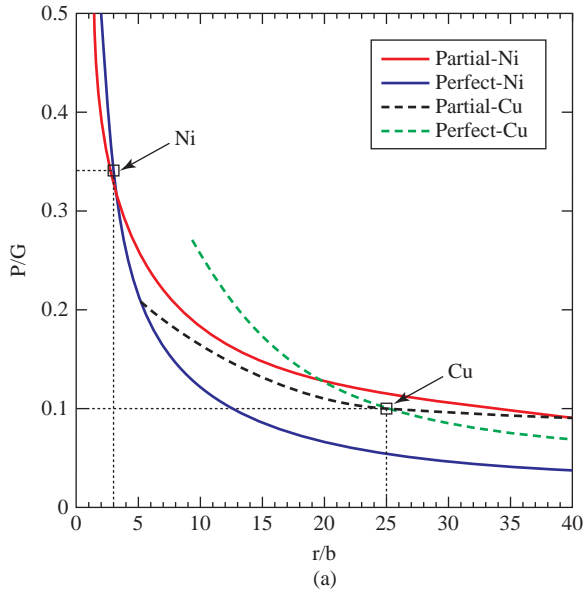
Fig. 42. (a) Theoretical result showing the critical radius of perfect and partial dislocations for Ni and Cu decreasing with shock pressure; (b) stacking faults and cells in the same TEM micrograph of laser driven, ramped compression of [0 0 1] Cu at $P_{max} = 24$ GPa, demonstrating that there is a critical value for the transition.

35 GPa [9,73,75,94], and about half the pressure at which stacking faults began to appear in our Ni MD study (Jarmakani et al. [130]). The predicted transition pressure for Cu, ~ 5 GPa, is also significantly lower than both MD and experimentally observed results [92,93]. Experimental evidence for the cell-stacking-fault transition has been gradually amassing for copper, and the TEM micrograph of Fig. 42(b) is clear. For Ni, the transition pressure is much higher (27 GPa). This exceeds the critical pressure for twinning ($P = 46$ GPa, calculated in Section 6) and

is consistent with the absence of stacking-fault observations in shock-compressed nickel. Thus, one has the following defect regimes as *P* is increased:

   Cu: cells→stacking-faults→twins
   Ni: cells→twins.

   The TEM micrograph from Fig. 42(b) comes from a quasi-isentropic laser compression experiment at a nominal pressure of 24 GPa for a [001] copper monocrystal. One sees adjacent regions of stacking faults and dislocation cells, with a well-defined discrete boundary. This was a fortuitous observation and the transition can be caused by pressure or strain rate. Nevertheless, it clearly illustrates the dual nature of the microstructure induced.

6.5. Quasi-isentropic compression of metals

ICE is a shockless process where very high-pressure conditions can be accessed in ramp wave loading, and the accompanying temperature rise is much less severe than during shock experiments. The main motivation behind such a process is that the solid state of a material can be retained at higher pressures due to the lower temperatures experienced, and an understanding and characterization of the material response is, therefore, possible. In fact, quasi-isentropic experiments come very close to simulating conditions that occur in the core regions of planets [123]. ICE experiments in the early seventies were aimed at mimicking these conditions.

   Quasi-isentropic compression conditions can be achieved by various methods: gas-gun, laser, and magnetic loading. Early work on ICE with a gas-gun by Lyzenga et al. [133] used a composite flyer plate with materials of increasing shock impedance away from the target material. Barker [134] placed powders of varying densities along a powder blanket and pressed the blanket to produce a pillow impactor having a smooth shock impedance profile. Similarly, this current effort uses density-graded impactors. In the case of ICE via laser, McNaney et al. [135] used a shockless laser drive setup to compress and recover an Al alloy. A smoothly rising pressure pulse is generated by focusing a laser beam on a reservoir material (carbon foam), creating a plasma that "stretches out" through a vacuum and stagnates or piles up onto the sample. In magnetically driven experiments [136], the *Z* accelerator at Sandia National Laboratories (SNL) is capable of producing quasi-isentropic compression loading of solids using magnetic pulses. An advantage of this method is that a smoothly rising pressure profile can be generated without the initial spike at low pressures seen during impact experiments. Control over loading pressures and a rise time is also possible in graded density impactors to meet experimental requirements [137].

6.5.1. Gas-gun ICE setup
Quasi-ICEs via gas-gun were carried out on [001] copper and the recovered deformation substructure was analyzed. A two-stage gas-gun setup located at LLNL provided for the quasi-isentropic loading. It employs functionally graded
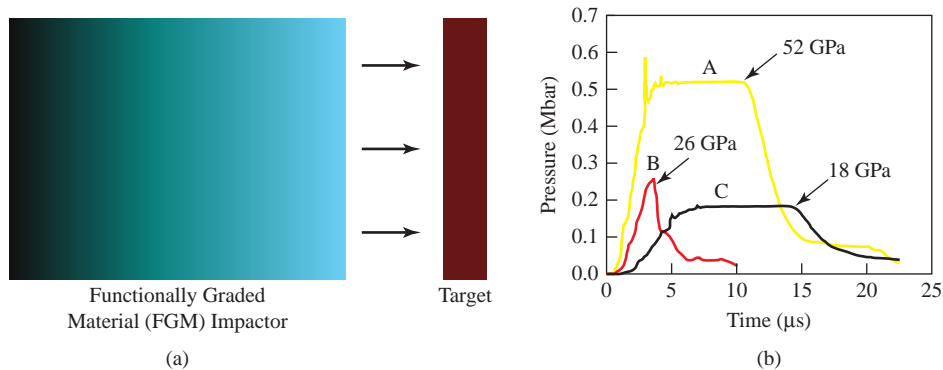
Fig. 43. (a) Illustration of a functionally graded material (FGM) impactor hitting a target (darkness proportional to density); (b) pressure versus time profile of gas-gun experiments using FGM impactors [137].

material (FGM) impactors designed with increasing density profiles (or shock impedance), as depicted in Fig. 43(a), to produce the smoothly rising pressure profiles. Three different FGMs were used, each providing a certain density range. A detailed description of the impactors can be found in Ref. [137]. Three experiments, A (52 GPa, 1700 m/s), B (26 GPa, 1260 m/s), and C (18 GPa, 730 m/s) are reported. The as-received samples belonging to each batch were in the form of cylindrical specimens having an average diameter and thickness of 6 and 3.6 mm, respectively. Two distinct pressure profiles were obtained using CALE, a hydro-dynamics simulation code; one having a hold time of approximately 10 μs (A and C) and one having relatively no hold time (B), as shown in Fig. 43(b). It should be noted that A exhibited a spike or slight shock at the onset of the pulse duration due to the experimental setup and the likely effect on the microstructural deformation process is briefly discussed in Section 6.5.4. Strain rates obtained via CALE were on the order of 10^4–10^5 s^{-1} lower than laser-driven ICE.

6.5.2. Laser ICE setup

The Omega Laser System at the University of Rochester, NY, was used to generate a smoothly rising pressure pulse in the material. This pulse is created by focusing a laser beam on a reservoir material (carbon foam) facing the sample and separated from it by a necessary vacuum gap (~ 300 μm). The beam creates a plasma that "stretches out" through the vacuum and stagnates on the front face of the sample. The strain rates achieved with this setup were on the order of 10^7 s^{-1}, three orders of magnitude higher than that of the gas-gun experiments. McNaney et al. [135] use the same shockless laser drive setup to compress and recover [0 0 1] copper and a more detailed description of the setup can be found in their publication. An illustration of the setup is provided in Fig. 44(a) accompanied by a typical pressure profile modeled by CALE [Fig. 44(b)] [135]. The three peak pressures reported for the laser ICE experiments are 18, 24, and ~ 59 GPa, very reasonably close to the
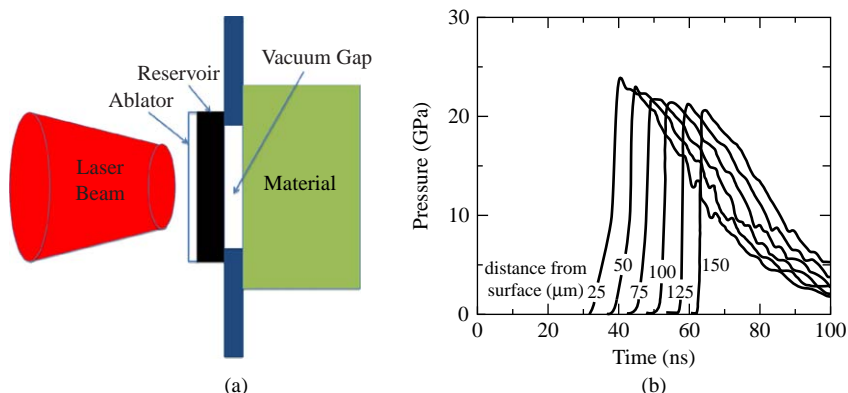
Fig. 44. (a) Schematic of the laser isentropic compression experimental setup; (b) typical pressure versus time profiles obtained (~ 24 GPa).
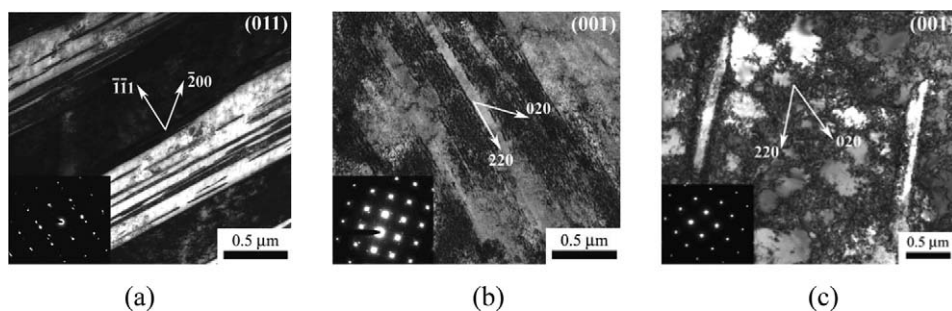
Fig. 45. (a) Twinned regions in Cu ~ 0.1 mm from surface, 52 GPa; (b) stacking faults at 1.3 mm running along $[2\,2\,0]$, 26 GPa; (c) elongated and regular cells at 0.13 mm, 18 GPa.

gas-gun pressures. The pressure estimate of 59 GPa is more uncertain than the others because of the lack of benchmarking the data for the reservoir used in the experiment. An extrapolation from higher-pressure data was done instead. Section 9 describes some attempts to reproduce ICE loading using MD simulations.

6.5.3. TEM
6.5.3.1. Gas-gun ICE. TEM samples in Cu analyzed from A (52 GPa) revealed various deformation substructures. Dislocation activity was most abundant, however, other deformation features were found. At approximately 0.1 mm from the impact surface, some limited evidence of twining was found. Fig. 45(a) shows very clear twinned regions. At a TEM beam direction of $B = [0\,1\,1]$, both small and large twins were observed having $(1\,\bar{1}\,1)$ twin habit planes. These microtwins are embedded within dislocated laths running along the same direction. The smallest twins measured had lengths of approximately 80 nm, and the longest twins were on

the order of 1.5 μm. TEM images (not shown here) taken at the same depth with $B = [001]$ showed twins running along the $[\bar{2}20]$ and $[220]$ at 90° to each other. In certain areas of the sample, single lath variants and stacking faults with thicker features running along the $[\bar{2}20]$ and $[\bar{2}\bar{2}0]$ directions were captured. We suggest that these substructures are due to thermal recovery. At 0.7 and 1.2 mm from the surface, heavily dislocated laths running along the $[220]$ direction were observed having an average thickness of 0.6 and 0.7 μm. Twinning, confirmed by a diffraction pattern, was evident at 1.2 mm. The average dislocation cell size at this depth was 0.15 μm. At 1.8 mm, dislocation cells with an average size of 0.2 μm were mostly abundant.

Foils from B (26 GPa) mostly revealed dislocation cells, where the average cell size increased from 0.4 μm at 0.25 mm within the sample to 0.5 μm at 2.7 mm. At 0.9 and 1.3 mm from the impact surface, stacking faults were evident in a few isolated regions running along the $[220]$ orientation [Fig. 45(b)]. Dislocated laths at 1.8 mm and elongated dislocation cells at 2.3 mm away from the impacted surface were observed stretched along the $[220]$ direction. For experiment C (18 GPa), relatively large dislocation cells were the most abundant deformation substructure [Fig. 45(c)]. The average dislocation cell size varied from approximately 0.5 μm at 0.13 mm within the specimen to 0.6 μm at 2 mm. Elongated cells along the $[220]$ direction were observed and some lath-like features were noticed in some regions, in particular closest to the impact surface at ∼0.1 mm within the sample. The elongated cells seem to have relaxed from the dislocated lath structures located at regions experiencing higher pressures closer to the impact surface.

6.5.3.2. Laser ICE. At the highest pressure of approximately 59 GPa for the laser-ICE experiments in Cu, a large number of faults/twins was observed [Fig. 46(a)]. They were preferentially oriented along the $[0\bar{2}2]$, identical to what has been reported in laser-shocked copper [92,93] and the gas-gun ICE experiments. They were found near regions of extremely high dislocation densities. Laths spaced at regular intervals of 500 nm (also their average width) were also observed with heavily dislocated regions in between. At a lower pressure of 24 GPa, stacking faults
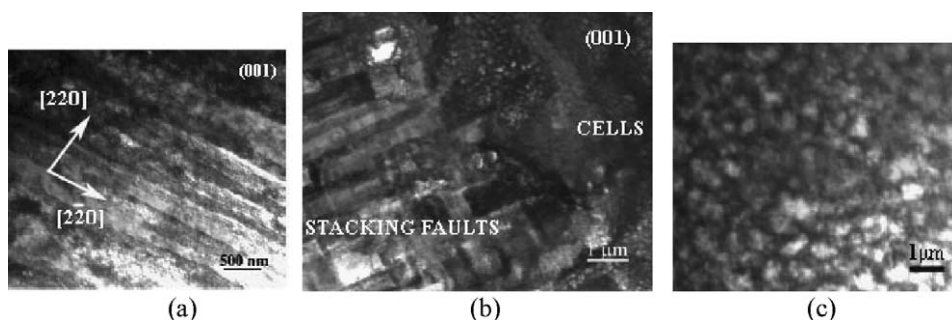

Fig. 46. Deformation structures of laser isentropically compressed Cu: (a) Twins/laths at 59 GPa; (b) dislocation cells and stacking faults at 24 GPa; (c) dislocation cells at 18 GPa.

were dominant. An interesting image, Fig. 46(b), was taken of a transitional substructure showing dislocation cells to the right and stacking faults to the left. The average dislocation cell size was 0.2 µm and the cells comprised of $\langle 110 \rangle$ type dislocations. The stacking faults were identical to the four variants observed in laser shock compression having a $\{111\}1/6\langle 112 \rangle$ nature. The average spacing was 650 nm with a width of nearly 150 nm. There was no visible difference in the material that contained cells and the area that contained stacking faults. The imaged area was taken from near the center of the sample and deepest part of the crater. This microstructure is also shown in Fig. 42(b).

Dislocation cells, Fig. 46(c), similar to those observed in shock loading were the predominant mode of deformation for the samples loaded to 18 GPa. The defects were primarily ½$\langle 110 \rangle$ type dislocations which have relaxed into cells. The cell sizes measured in the isentropic specimens at this pressure were approximately 0.3 µm. One unique characteristic of the isentropic compression was the uniformity of the cell sizes at the given pressure. Unlike shock loading where there was substantial variance between cell sizes [37], the quasi-isentropically loaded specimens were very similar in size and shape. Also, the dislocation cells were more clearly defined as compared to laser-shocked samples previously studied [37]. This is likely a result of the isentropic loading conditions.

6.5.4. Twinning threshold modeling: ICE and shock

The Preston–Tonks–Wallace (PTW) [138] constitutive description was used by Jarmakani et al. [139] to determine the critical pressure for twinning in both laser and gas-gun quasi-isentropic compression, as it is very suitable for the very high strain rates in these experiments. It takes into account both the thermal activation and dislocation drag regimes. The instantaneous flow stress in the thermal activation regime can be calculated from Eq. (7) in ref. [138], namely

$$
\begin{aligned}
\tau = \hat{\tau}_s + \frac{1}{p}(s_0 - \hat{\tau}_y)\ln\Bigg\{ 1 - \Bigg[1 - \exp\Bigg(\Bigg(&-p\frac{\hat{\tau}_s - \hat{\tau}_y}{s_0 - \hat{\tau}_y} \Bigg) \Bigg] \Bigg(\\
\times \exp\Bigg[\frac{-p\theta\psi}{(s_0 - \hat{\tau}_y)[\exp(p((\hat{\tau}_s - \hat{\tau}_y)/(s_0 - \hat{\tau}_y))) - 1]} \Bigg] \Bigg) \Bigg\},
\end{aligned}
\tag{47}
$$

where $\hat{\tau}_s$ and $\hat{\tau}_y$ are the work hardening saturation stress and yield stress, respectively. Separate expressions modeling $\hat{\tau}_s$ and $\hat{\tau}_y$ in both the thermal activation regime and strong shock regime are provided by PTW (not given here for conciseness). The s_0 parameter is the value of $\hat{\tau}_s$ taken at zero temperature, ψ and θ are the strain and work hardening rate, respectively, and p is a dimensionless material parameter. The flow stress is normalized to the shear modulus, G (e.g., $\hat{\tau}_y = \tau_y/G$). Where appropriate the temperature dependence of the shear modulus was approximated as $G(\rho, T) = G_0(\rho)(1 - \alpha\hat{T})$, where $G_0(\rho)$ is the zero temperature modulus as a function of density and α is a material constant. The pressure dependence of the model is due to the pressure dependence of the shear modulus.

The model parameters were slightly modified to match the low strain rate work hardening behavior for $\langle 100 \rangle$ copper. In particular, the work hardening rate, θ,
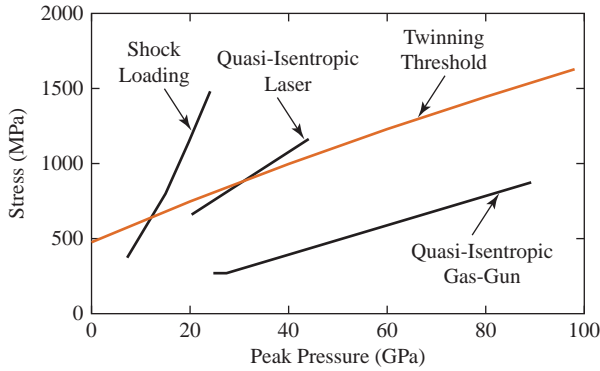
Fig. 47. Flow stress versus peak pressure for shock compression, gas-gun ICE and laser ICE experiments in Cu.

was adjusted to a value of 0.01 and saturation stress, s_0, to a value of 0.0045. All other parameters are as given in Jarmakani et al. [139]. In the shocked region, the temperature and strain were taken from the simulations while the strain rates were determined from the Swegle–Grady relation [32]. Jarmakani et al. [139] also assumed that the flow stress and twinning stress, being dependent on the atomic energy barrier, scale with the shear modulus, as is typical in high-pressure constitutive models. This was not done in Section 6.3.2.1. Results of these calculations are presented in Fig. 47, where the flow stress, as a function of peak drive pressure, for the shockless and shocked region are plotted for both quasi-isentropic gas-gun and laser compression. The twinning threshold was assumed to vary with pressure through the pressure dependence of G:

$$\sigma_{\mathrm{T}}(P) = \sigma_{\mathrm{T}}^0 \frac{G(T, P)}{G_0} \leftarrow ; \qquad (48)$$

where σ_{T}^0 and G_0 are the twinning threshold stress and shear modulus at ambient pressure, respectively. The quasi-isentropic gas-gun curve lies well below the twinning threshold curve at all pressures. Obviously, a slip–twinning transition is not predicted to occur during gas-gun loading, and a twinning threshold stress should, therefore, not be reached. This is inconsistent with experimental observations at $P_{\mathrm{max}} = 52$ GPa, since twinning was observed at that pressure. The presence of the shock at the start of the shock pulse for this pressure condition creates a deviation from quasi-isentropic conditions and may be accountable for the presence of the twins observed. In the case of laser ICE, the threshold lies at $P_{\mathrm{max}} = 32$ GPa, consistent with observations of the lack of twinning at 24 and 18 GPa, and their presence at 59 GPa. The steep shock loading curves in both cases arise due to the high strain rate dependence on both the shock pressure and flow stress [Fig. 43(b)]. Shown in these figures are a detailed set of plots from MD simulations of shocked Cu and Ni at various shock strengths (30–171 GPa),

propagation directions in the FCC lattice ([0 0 1, [2 2 1]), and in various presentation formats ($\sigma_{zz}(z)$, $\tau_{\text{shear}}(z)$, and pressure (z), at various time steps; τ_{shear} vs. σ_{zz}, etc.).

7. Molecular dynamics simulations of dislocations during shock compression

MD simulations of shocks have been carried out for decades, starting with shocks in unidimensional (1D) chains of atoms, [140] two-dimensional (2D) crystals (Mogilevsky [141,142]), and later leading to shocks in 3D crystals [143,144] and polycrystals [145]. Most simulations have been carried out [146] in crystals with fcc structure. However, there is a growing number of simulations for crystals with bcc and diamond structure (Zybin [147], C and Si), complex organic crystals (Strachan et al. [148] and even for quasicrystals [149]. MD simulations are ideally suited for comparison with laser-shock compression experiments because of similar time and length scales; thus, the combination of experiments and simulations provides valuable insight on the deformation processes involved. There are recent simulations reaching sample lengths of up to several micrometers along the shock loading direction [150], comparable to the thickness of some experimental samples, but with much smaller simulated cross-sections, tens of nanometers on each side and using periodic boundary conditions.

The difference between mono and polycrystals in MD simulations resides in the absence and presence of grain boundaries, respectively. A representative polycrystalline cross-section has to include several grains, and therefore the largest grain size simulated to date is only 50 nm [151], which is well-suited to model nanocrystals.

7.1. Computational methods

We have carried out MD simulations using the Large-scale Atomic/Molecular Massively Parallel Simulator (LAMMPS) code [152,153] with the EAM potentials for Cu (Mishin et al. [154,155], fitted to give a SFE of 45 mJ/m^2) and Ni (Mishin et al. [155], fitted to give a SFE of 125 mJ/m^2 [156]). These potentials give a Hugoniot along the main symmetry directions, which agrees with experimental data.

For better visualization, the "centro-symmetry" parameter is used to identify defective atoms (dislocation cores and stacking faults). It is of the form [152]:

$$\text{CSP} = \sum_{i=1}^{6} |\vec{r}_i + \vec{r}_{i+6}|^2, \tag{49}$$

where $\vec{r}_i$ and $\vec{r}_{i+6}$ are the vectors from the central atom to the opposite pair of nearest neighbors (six pairs in an fcc system, i.e., the coordination number). Atoms in perfect fcc lattice positions have a CSP equal to zero, whereas atoms having faulty stacking will generate a non-zero CSP.

In our MD simulations, two perfect fcc Cu crystals, [0 0 1] and [2 2 1], were shock-compressed at several pressures. Periodic boundary conditions were imposed on the lateral surfaces, and the surfaces normal to the shock-wave propagation direction were set as free surfaces. The [0 0 1] monocrystalline copper had dimension of $\sim 9 \times 9 \times 36 \, \text{nm}^3$ ($25 \times 25 \times 100$ fcc unit cells). This is sufficiently large to calculate the shock Hugoniot and study the early stages of shock-induced plasticity, given that much larger simulations produce similar results [142]. For [1 0 0] shock propagation, the three coordinate axes were [1 0 0], [0 1 0], and [0 0 1]. The [2 2 1] monocrystal had a dimension of $\sim 15.3 \times 15.3 \times 65 \, \text{nm}^3$ ($42.42 \times 42.42 \times 180$ fcc unit cells) along the three coordinate axes of [$\bar{1}\,\bar{1}\,4$], [$1\,\bar{1}\,0$], and [2 2 1]. These dimensions are required for periodic boundary conditions in the lateral directions. The shock waves were produced as described by Cao et al. [88] a piston applied to the material at a velocity U_p. The velocity of the shock wave, U_s, can then be calculated from the propagating front in our samples. The shock pressure can be calculated both from our MD simulations and from the Hugoniot relationship, once U_s and U_p are known.

The [0 0 1] monocrystalline nickel sample consisted of 2×10^6 atoms and had dimensions of $17.6 \times 17.6 \times 70.4 \, \text{nm}$ ($50 \times 50 \times 200$ unit cells). The three coordinate axes were oriented in the [1 0 0], [0 1 0], and [0 0 1] directions. Two nanocrystalline (nc) samples were also shock-compressed in this study, one having a grain size of 5 nm and the other 10 nm. The 5 nm grain-sized sample consisted of 1,980,372 atoms ($50 \times 50 \times 200$ unit cells, $17.6 \times 17.6 \times 70.4 \, \text{nm}$), and the 10 nm grain-sized sample had 7,942,605 atoms ($100 \times 100 \times 200$ unit cells, $35.2 \times 35.2 \times 70.4 \, \text{nm}$). Prior to compression, the specimens were first equilibrated to minimize their energy, and the initial temperature was set as 5 K. The velocity of the shock wave, U_s, was measured by analyzing the shock-front propagation in the sample at different time steps, and the shock pressure was calculated from the following Hugoniot relation (see, e.g., [158]):

$$P_{\text{shock}} = \rho_0 U_s U_p. \tag{50}$$

7.2. FCC single crystals

MD simulations of shock phenomena in perfect fcc single crystals have been carried out for just over 25 years [143]. Most of the simulations to date have used the Lennard–Jones (L–J) 6–12 pair-potential [154,157,159,160] and the more realistic embedded atom method (EAM) many-body potentials for copper [85,156], Ni (Koci [161]). The EAM approach [85,156] allows an accurate description of elastic properties, EOS, and defect energies in metals, particularly for fcc metals like Cu, Ni, Al, etc. However, most EAM potentials are fit to reproduce properties at ambient conditions and may lead to faulty results when used under shock conditions. Among the quantities that should be verified for an EAM potential which would be used for shock simulations are the EOS up to the desired simulation pressure, the shear stress versus pressure for uniaxial compression along the directions of interest, the elastic constants versus pressure, and the stacking fault and twinning energies [162].

Holian et al. [145] and Germann and co-workers [154,159] used a L–J potential with zero SFE at ambient pressure and showed that, at shock strengths above the Hugoniot Elastic Limit (HEL), shock waves traveling along the [0 0 1] orientation resulted in the emission of intersecting Shockley partial dislocations that slipped along all the {1 1 1} close-packed planes. Stacking faults were formed since the trailing partial was never released. The large mobility of the partials at the shock front was such that the plastic wave was always overdriven (i.e., no elastic precursor was observed). This dislocation behavior is very similar to the model proposed by Smith [163], except that partial dislocation loops are emitted in MD simulations rather than perfect dislocations as outlined by the Smith model.

Germann and co-workers [154,159] further studied shock propagation in the other [1 1 0] and [1 1 1] low-index directions, where they observed rather different behavior. An elastic precursor separated the shock front from the plastic region in the [1 1 1] case, and solitary wave trains were generated followed by an elastic precursor and a complex plastic zone in the [0 1 1] case. In both orientations, trailing partials were emitted leading to full dislocation loops bounded by thin stacking-fault ribbons. These loops were periodically nucleated at the shock front, as proposed by Meyers [36], since they grew at a slower rate than the plastic shock velocity. The reader is referred to Figs 3 and 4, which present the basic elements of the homogeneous dislocation model. Bringa et al. [164] also studied the effect of crystal orientation on the shock Hugoniot along the low-index directions ([0 0 1], [0 1 1], and [1 1 1]) using two EAM potentials for copper. The plasticity in the three orientations was qualitatively similar to that of Germann et al. [154,159].

The molecular dynamics calculational procedure presented in Section 7.1 with the use of the centro-symmetry filtering method was applied to copper and nickel and the results are presented in this section (Figs 48–56); the results by Cao et al. [88] and Jarmakani et al. [130] are summarized here. Cao et al. [88] investigated the non-symmetric [2 2 1] orientation of Cu, where a two-wave structure (elastic and plastic) was observed.

The progression of the shock front through copper specimens is shown in Fig. 48; Fig. 48(a) corresponds to [0 0 1] and Fig. 48(b) to [2 2 1]. The defect structure is relatively unchanged during the advance of the front. For both orientations, we observe nucleation and growth of stacking-fault loops. Sequential snapshots of the flow velocity of the atoms in the copper sample enable the calculation of the shock-wave velocity for the two orientations. Fig. 49 shows the shock wave at three times for (a) the [0 0 1] and (b) the [2 2 1] orientations at $U_p = 4$ km/s. The wave front is in the right-hand side, and the rigid piston on the left side. Note that a plastic front exists for [0 0 1], but does not lead to a two-front structure. On the other hand, for the shock along [2 2 1], the front splits into an elastic precursor and a plastic front, as shown Fig. 49(b). Splitting of the elastic and plastic shock has been observed for [1 1 1] and [1 1 0] directions.

Figs 50(a) and (b) show the pressure and the shear stress for the shock propagation along [0 0 1] (top) and [2 2 1] (bottom), for the three times shown in Fig. 49. The shear stress, s_{sh}, was calculated as $s_{sh} = 0.5[s_{zz} - 0.5(s_{xx} + s_{yy})]$, since the off-diagonal terms in the stress tensor were found to be negligible. For [2 2 1], the
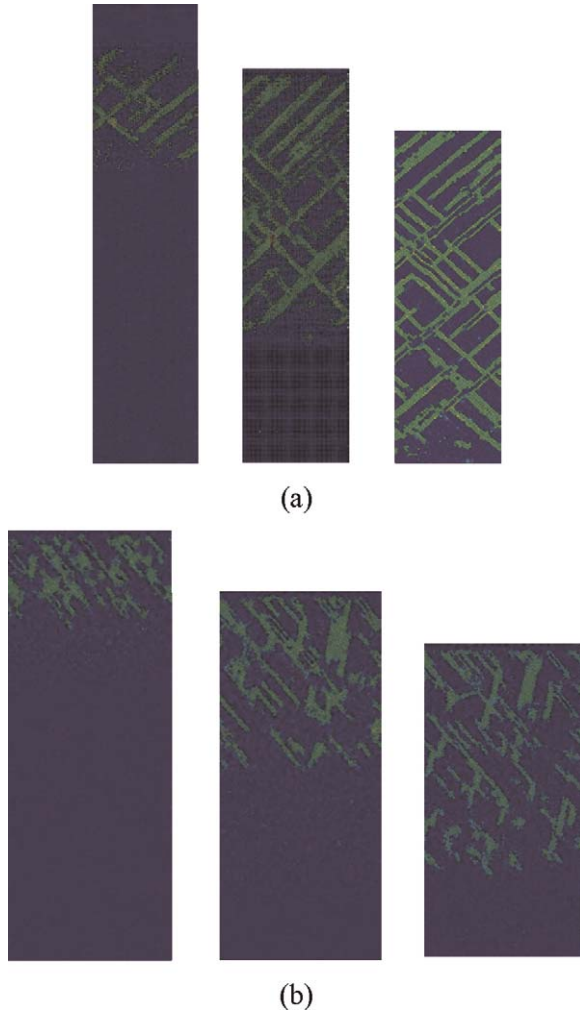
Fig. 48. MD simulation of the propagation of shocks in copper driven by a piston (particle) velocity of $U\mathrm{p} = 4\,\mathrm{km\,s^{-1}}$ ($P_{\mathrm{shock}} = 48.5$ GPa) for (a) [001] and (b) [221] Cu at increasing times: (1) 2 ps; (2) 4 ps; (3) 6 ps. Light colors indicate stacking faults and dislocations [88].

decrease in shear stress [Fig. 50(d)] coincides with the pressure rise that leads to dislocation nucleation and the formation of a plastic front; the shear stress relaxes because of dislocation loop nucleation and growth at the plastic front. For [001] [Fig. 50(c)], this relaxation occurs within a region extremely close to the shock front.

Figs 51 and 52 show the comparison of the computed and experimentally observed deformation features.

The deformation features and shock Hugoniot obtained compared very well with experimental results. However, upon comparing the density of the deformation
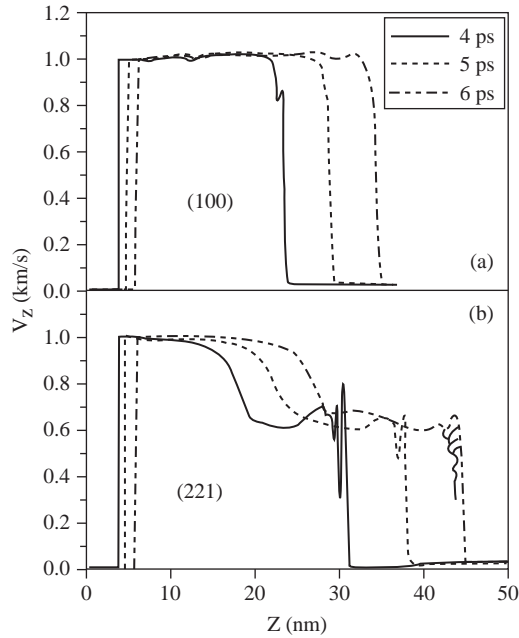
Fig. 49. Particle velocity versus distance for an MD simulation of shock propagation in (a) [0 0 1], and (b) [2 2 1] in single crystal Cu [88].
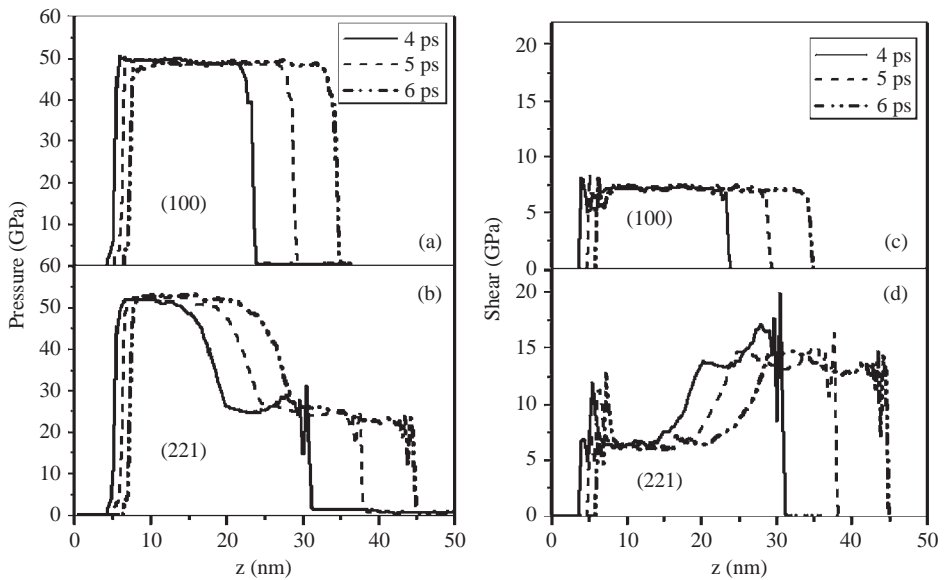

Fig. 50. (a, b) Pressure profiles at three different times for (a) [0 0 1], and (b) [2 2 1] Cu monocrystals; (c, d) shear stress profiles at different times for (c) [0 0 1], and (d) [2 2 1] Cu monocrystals [88].
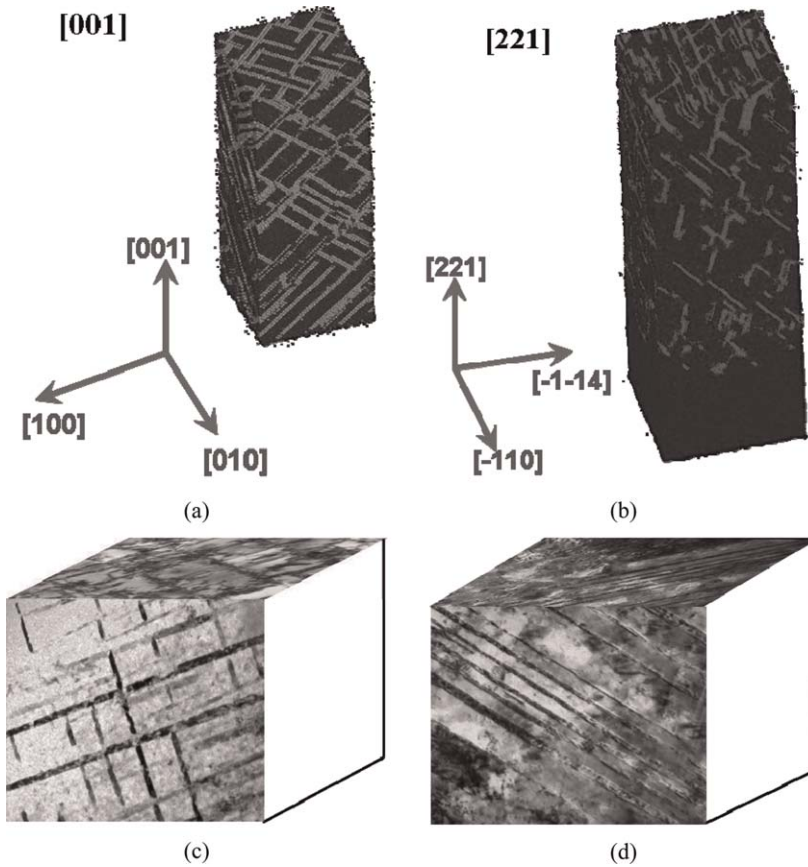
Fig. 51. Defect structures in Cu: (a) MD simulation results for the propagation of a 48.5 GPa shock along the [001] direction; (b) MD simulation for the propagation of a 48.5 GPa shock along the [221] direction; (c) TEM micrographs for [001] Cu monocrystal shocked at 30 GPa; (d) TEM micrographs on [221] monocrystal of Cu shocked at 30 GPa [88].

features with experimental observations in recovered samples, they found that the dislocation densities in the simulations were several orders of magnitude higher. Two reasons were suggested by Cao et al. [88] for the difference: (a) the much shorter rise time in the MD simulations and (b) the post-shock relaxation and recovery processes that take place in real experiments.

Kum [165] analyzed the deformation features in shock-compressed single-crystalline Ni along the three low-indexed orientations. Two Morse-type pair potentials and one EAM potential were used in that work. However, the study is limited to one piston velocity and does not calculate the Hugoniot obtained from the MD simulations. The Hugoniot of Ni using one EAM potential, was calculated by Koci et al. [161], but their focus was the study of shock melting.
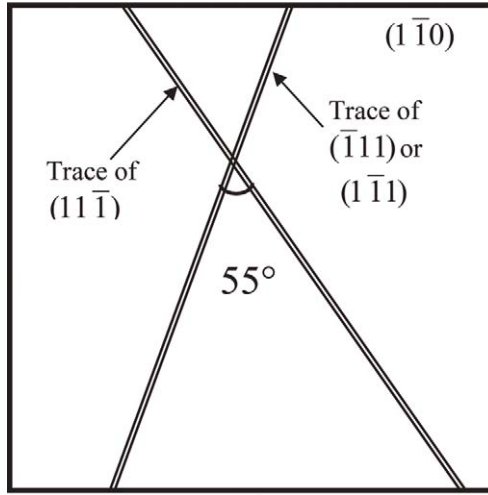
(a)
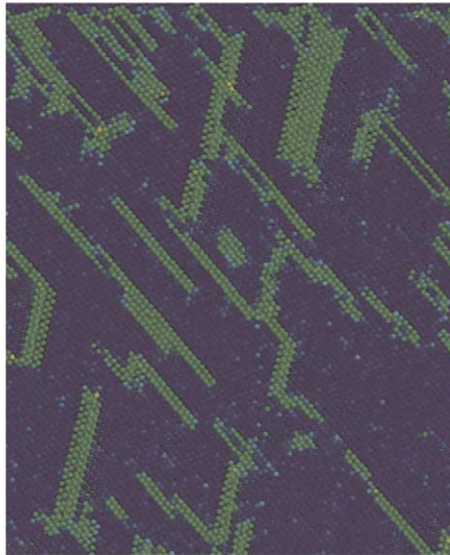
(b)

Fig. 52. (a) Schematic illustration of traces of Cu {1 1 1} slip planes on the surface of a $(1\,\bar{1}\,0)$ plane; (b) MD simulation showing traces of the stacking fault slip systems on the surface of $(1\,\bar{1}\,0)$ shown by an MD simulation for shock propagation along $[2\,2\,1]$ [88].
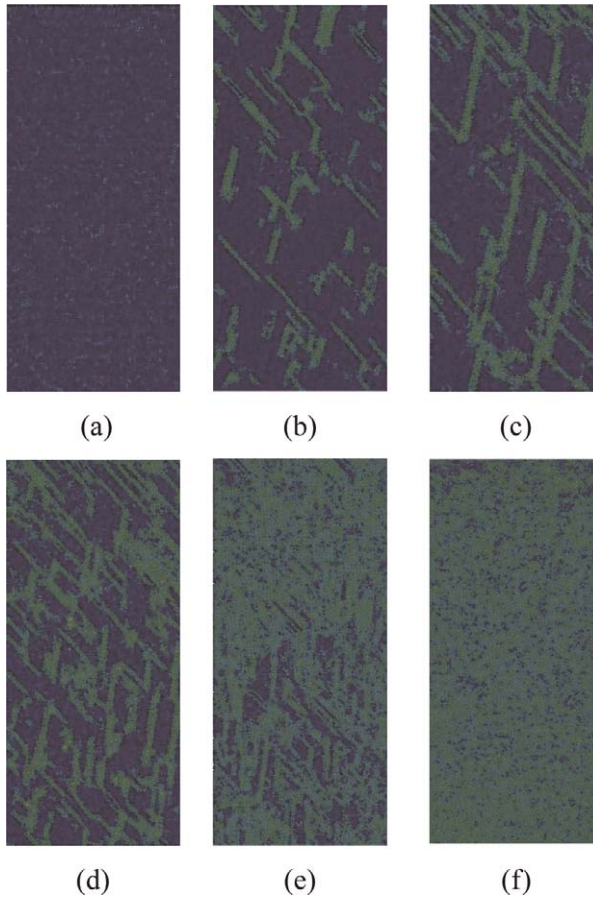
Fig. 53. MD simulation showing dislocation structures at 8 ps in shocked [2 2 1] Cu as a function of particle/piston velocity: (a) 0.75 km/s (33.9 GPa); (b) 1 km/s (48.5 GPa); (c) 1.25 km/s (64.8 GPa); (d) 1.50 km/s (82.8 GPa); (e) 2.00 km/s (123.7 GPa); and (f) 2.5 km/s (171.3 GPa) [88].

The simulations show that, as the piston (equivalent to particle) velocity is increased, the defect density increases. The sequence of snapshots in Fig. 53 represents a range of pressures from 33.9 to 171.3 GPa for the [2 2 1] crystal. Note that the density of defects for $P = 471.3$ GPa ($U_p = 2.5$ km/s) is extremely high and the material resembles a nearly amorphous material. The shock-melting pressure for this EAM copper was calculated as ~ 200 GPa. Hence, the melting as determined from hydrodynamic calculations and the extreme dislocation density observed in the computation of Fig. 53(f) are consistent.

A similar procedure was applied by Jarmakani et al. [130] to nickel, and the shock propagation profiles for [0 0 1] are shown in Fig. 54 for two pressures: 35 and 48 GPa. At 45 GPa, an elastic precursor is evident, which is absent at 35 GPa. The computations show that formation of dislocation loops behind the front, seen
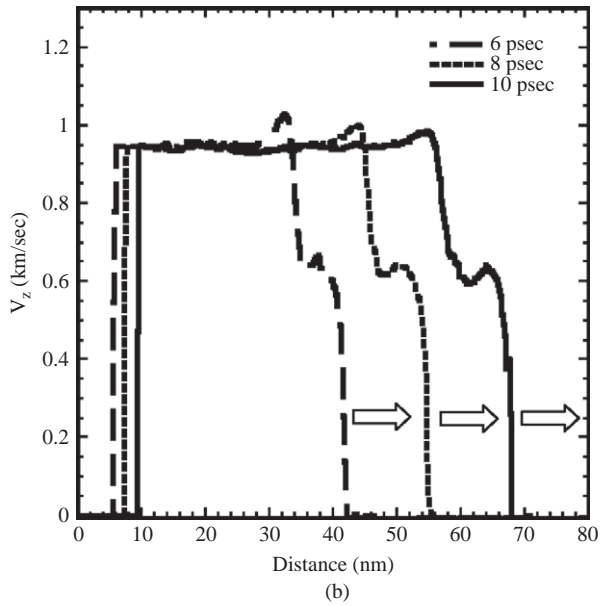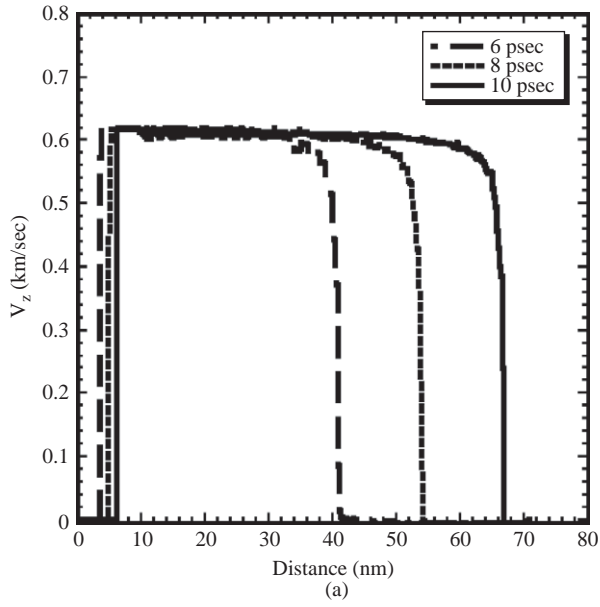
Fig. 54. MD simulations for shocked single crystal Ni along [0 0 1]; (a) piston (particle) velocity at 6, 8, and 10 ps versus distance (below the HEL) for $P \sim 35$ GPa; (b) piston (particle) velocity at 6, 8, and 10 ps versus distance (above the HEL) for $P_{shock} \sim 48$ GPa [130].

(a)

(b)

(c)
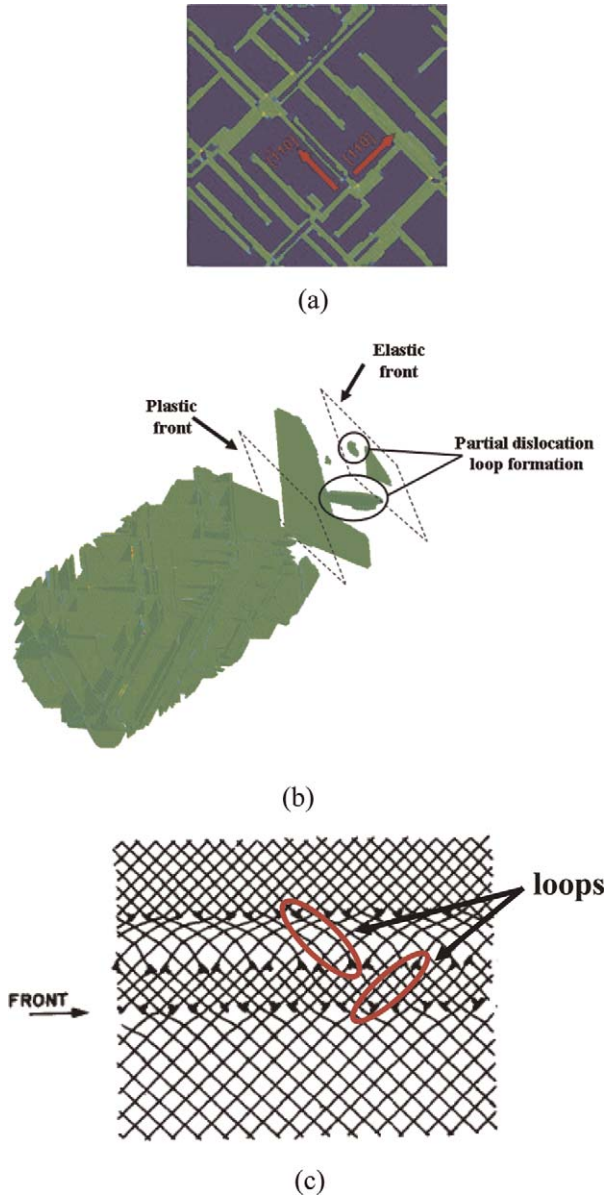
Fig. 55. MD simulation of shock compression of Ni along [0 0 1]; $U_\mathrm{p} = 0.786\,\mathrm{km/s}$: (a) Stacking faults, viewed along the longitudinal z direction; (b) plastic and elastic zone formation; notice the formation of dislocation loops; and (c) sketch of a dislocation interface in the homogeneous generation model (adapted from [36]).

(a)

(b)
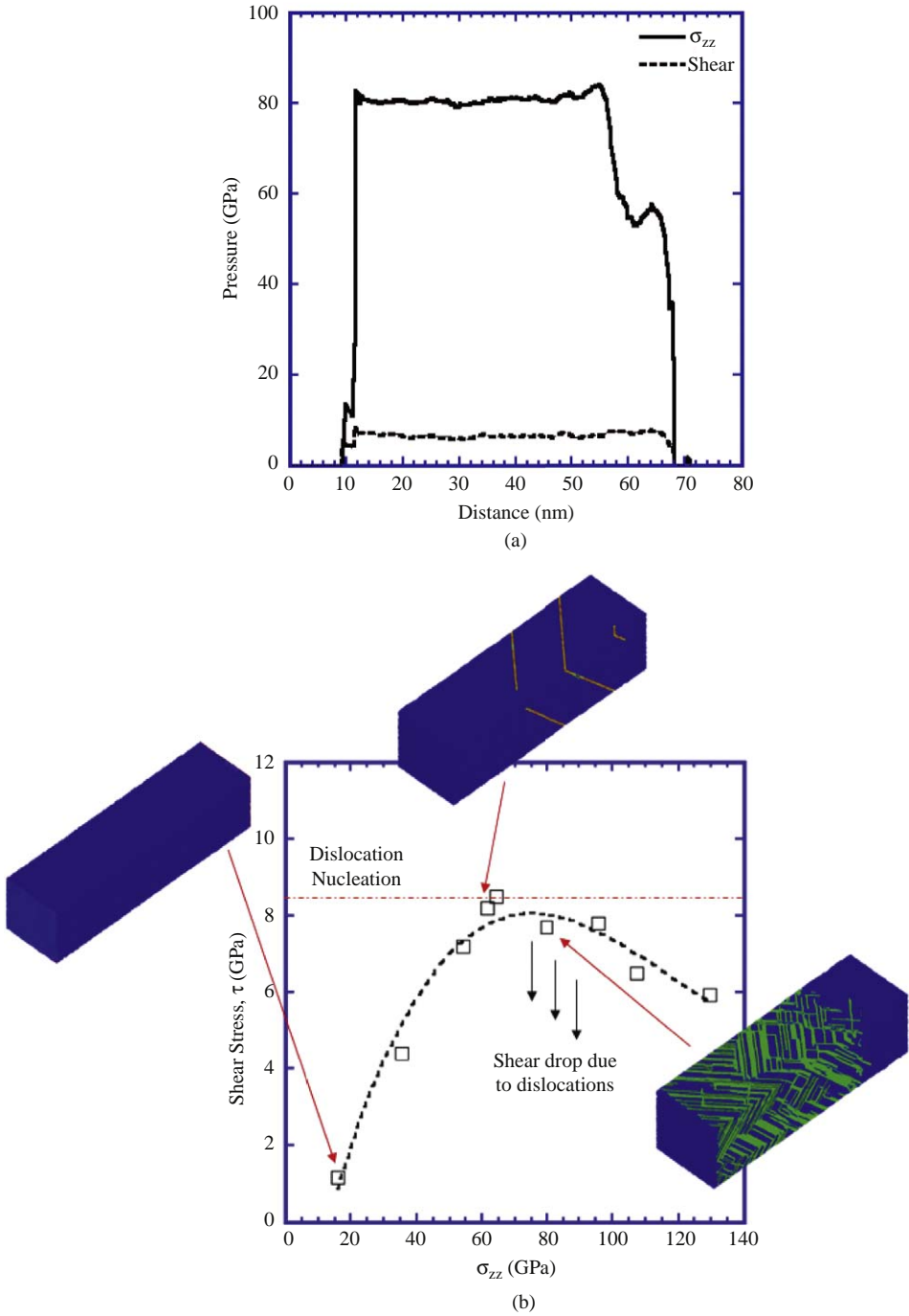
Fig. 56. (a) Shear stress and σ_{zz} versus sample depth for an MD simulation of single crystal Ni shocked along the [0 0 1] direction at $U_p \sim 0.945$ km/s; (b) shear stress versus σ_{zz}.

clearly in Fig. 55. The section in Fig. 55(a) shows the stacking faults on {111} planes whereas the 3D representation in which all atoms not belonging to dislocations were filtered out is shown in Fig. 55(b). The partial dislocation loops are nucleated between the elastic precursor and the plastic wave front and expand, creating a very high dislocation density in the shock compressed region. The mechanism by which these loops nucleate and grow is shown schematically in Fig. 55(c). The computations, which start from a defectless crystal, predict the initiation of plastic flow at exceedingly high pressures, that are indeed not realistic. This is shown in the simulation results shown in Fig. 56. Fig. 56(a) shows the normal and shear components of the stress. The shear component is shown in Fig. 56(b) as a function of increasing piston (or particle) velocity. Dislocation nucleation requires a shear stress of approximately 8 GPa in nickel ($\sim G/10$, since $G = 76$ GPa). It can be seen that a pressure of ~ 60 GPa is required to create a shear stress of 8 GPa. For lower pressures, there is no dislocation generation (tridimensional representation in left side of figure). At $P = 60$ GPa, a shear stress of 8 GPa is reached and one sees the first evidence of dislocations (top tridimensional figure). The shear stress decays beyond that, as the loops are nucleated and grow. This is accompanied by profuse partial dislocation activity in the slip planes.

The inclusion of defects like dislocation loops in single-crystal simulations allows reasonable agreement with experimental HEL results (Kubota et al. [166]), and a more realistic plastic relaxation description (Bringa et al. [167]). Therefore, there is still need for simulation of crystals with defects, and for further systematic research on MD shock simulations. For instance, in contrast with simulations using L–J potentials, simulations, using a Cu EAM potential showed nucleation of some full dislocations in shocks along [0 0 1] (Bringa et al. [167]), and simulations using a Ni EAM potential showed homogeneous nucleation of partial loops as the shock propagated (Koci et al. [161]). In addition, simulations using ramp loading do show an elastic precursor for rise times of ~ 50 ps or longer (Bringa et al. [167]) for EAM Cu loaded along [0 0 1].

8. Comparison of computational MD and experimental results

8.1. Comparison of monocrystals and polycrystals

The defect spacing as a function of shock pressure was analyzed in order to quantify the induced plasticity [see Fig. 57(a)]. Clearly, the spacing between stacking-faults decreases as the shock pressure increases. Copper data from Cao et al. [84,87,88] are plotted as well. Holian [144] introduced two fundamental deformation parameters: shock-induced plasticity and shock strength. Shock-induced plasticity is defined as a_0/l, where a_0 is the lattice parameter ($= 0.352$ nm for Ni), and l is the average lattice spacing between stacking faults. They defined shock strength as the ratio between particle velocity and speed of sound in the material, U_p/C_0 ($C_0 = 4.581$ km/s for Ni). This shock-induced plasticity as a function of shock strength is plotted in Fig. 57(b). MD data on Cu from Cao [84,87,88] and on Ni from
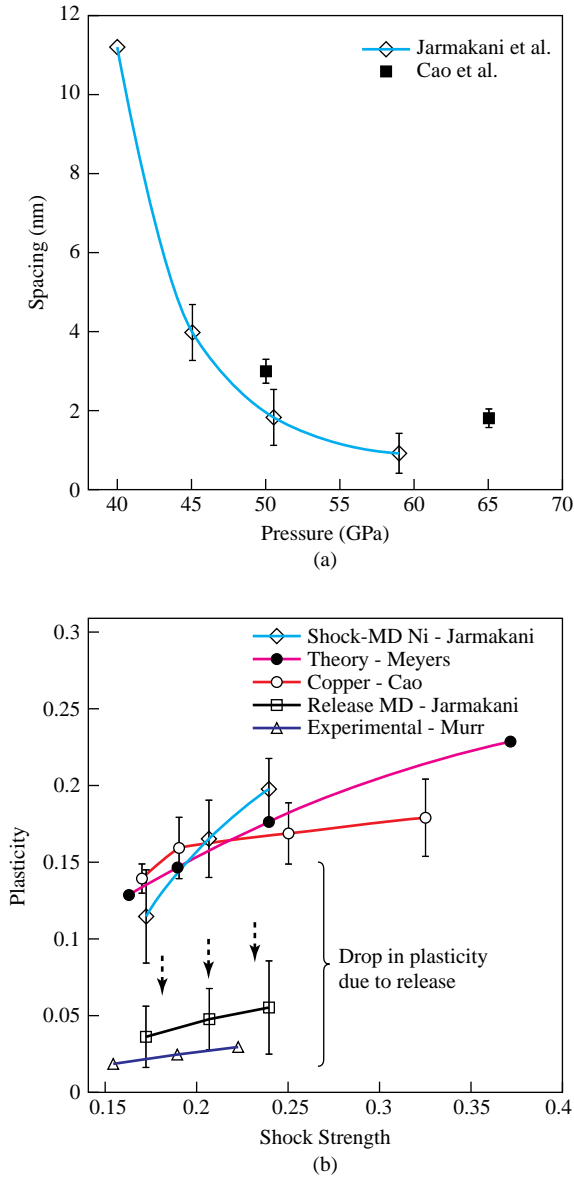
Fig. 57. (a) Spacing of dislocations versus shock pressure; (b) plot showing plasticity (a_0/l) versus shock strength (U_p/C_0), based on the analysis methods of Holian and Lomdahl [145].

Jarmakani et al. [130], predictions from the homogeneous nucleation model of Meyers [36], and experimentally measured data from Murr [40] are also shown on the plot. For the results from Meyers [36] and Murr [40], the dislocation spacing, *l*, was extracted from the reported dislocation densities, ρ, using the equation

$l = \sqrt{\rho^{-1}}.$ The plasticity results from the MD simulations of Jarmakani et al. [130] and Cao [84,87,88] are consistent. These predictions also agree with computations by Holian [144]. Interestingly, the early analytical model by Meyers [168] is in agreement with these MD calculations. The experimentally determined shock plasticity of Ni from Murr [40] is, however, lower than the theoretical and MD results by an order of magnitude. This is shown in greater detail in Fig. 58. This suggests that relaxation processes are clearly at play in real experiments resulting in lower dislocation densities, as will be shown below. One possibility to explain the experimental discrepancy between Ni and Cu is that electron–phonon coupling in Cu is much larger than in Ni, resulting in shorter heating periods and therefore, shorter thermal relaxation times. The role of electron–phonon coupling has been explored in Ni shock melting by Koci et al. [161], using a two temperature model coupled to their MD simulations. We note that laser experiments have explored different relaxation scenarios as a function of electron–phonon coupling [169,170].
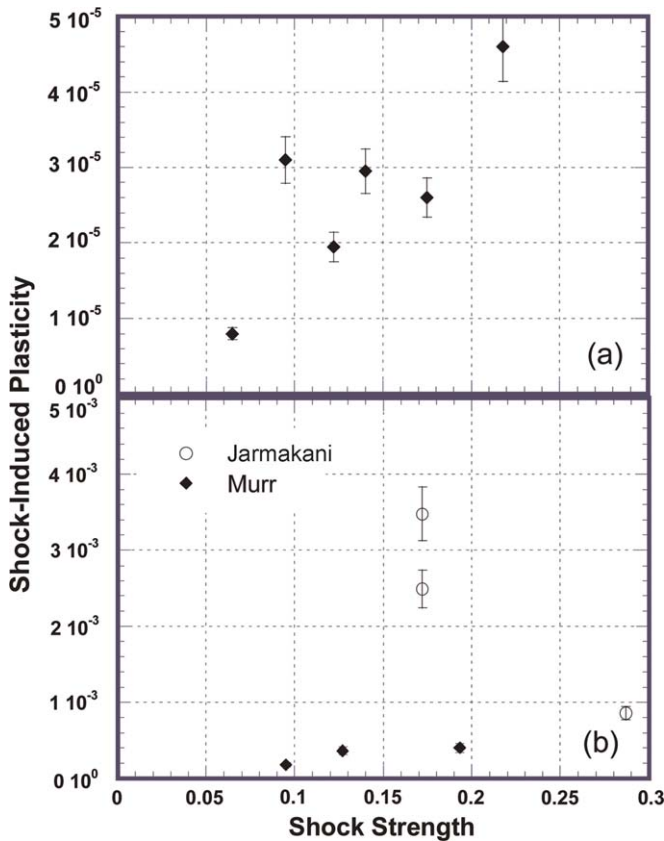

Fig. 58. Shock-induced plasticity calculated from experimental results for Ni: (a) Laser shock [37]; (b) plate impact [73].

The shock-induced plasticity increases monotonically with shock strength and follows closely the total volumetric strain U_p/U_s. Given that the total lateral strain in our simulations is zero due to periodic boundary conditions, the elastic strain has the same magnitude as the plastic strain, given by Orowan's equation [27]. The amount of dislocation motion needed to relax a given volumetric strain would be roughly the same for similar materials. Therefore, shock-induced plasticity would follow the total volumetric strain, even for different shock propagation directions and slightly different materials.

Experimental measurements in the literature extracted from TEM images for laser-shocked copper monocrystals subjected to a broad range of pressures [83,91,92,171] were converted into shock-induced plasticity, and the corresponding pressures were converted to shock strengths. The spacing between stacking-fault packets for the laser shock experiments are plotted in Fig. 58(a). The same monotonic increase in shock-induced plasticity with shock strength as shown for the MD simulations in Fig. 57(b) is observed. However, there is a major difference: the experimental values are lower by a factor of 10^4.

Plate impact [40,42,76,77,130,139,169,170,172–174] experiments on copper have been conducted since the seventies. Classic among these experiments are the systematic measurements made by Murr and co-workers [42,134–137] on inter-twin and inter-stacking-fault spacings. Fig. 57(b) shows the shock-induced plasticity calculated using the inter-twin spacings observed by Murr and co-workers [42,152,158,161,162], and the work to be reported in a paper by Cao et al. [172]. Jarmakani et al. [139] found similar results. The shock-pulse duration in Murr's experiments [40,42,76,77,173] was $\sim 2\,\mu s$, which is in the same range as our work by Cao et al. (1.4–2 μs) [172]. Work by Andrade et al. [174] confirms the twin spacing experimentally observed by Murr [40,42,76,77,169,173]. The calculated shock-induced plasticity from Murr's data is on the order of 10^{-4}, which is smaller than the experimental results in Cao et al. [172] ($\sim 10^{-3}$). These results, as well as the shock-induced plasticity in laser-shocked samples of $\sim 10^{-5}$ shown in Fig. 58(a) are compelling evidence for major effects that are not generally considered, leading to spacing between defects observed in simulations that is much smaller than that observed by TEM on recovered samples. There are several possible reasons for this discrepancy: (a) the higher strain rate in MD simulations; (b) simulation of only a small volume of perfect single crystal, without any initial defects [167]; and (c) the possibility that most defects are annealed out [167] and that TEM observations reveal a structure that is completely different from the one extant during shock compression. In our simulations, if we allow for the shock wave to reach the back of the sample and produce a rarefaction wave, most of the stacking-fault network disappears, making clear the important role that recovery can play in the TEM samples. Dynamic X-ray diffraction may be able to probe the dynamic dislocation generation seen in MD simulations in the future [167].

The effect of release (stress unloading) in the MD simulations was studied for comparison with experiments. The piston was released after 10 ps and the pressure ($P_{tot} = f(\sigma_{xx}, \sigma_{yy}, \sigma_{zz})$) was allowed to retract back to zero. Interestingly, almost all the partial dislocation loops disappear. The spacing between the few remaining
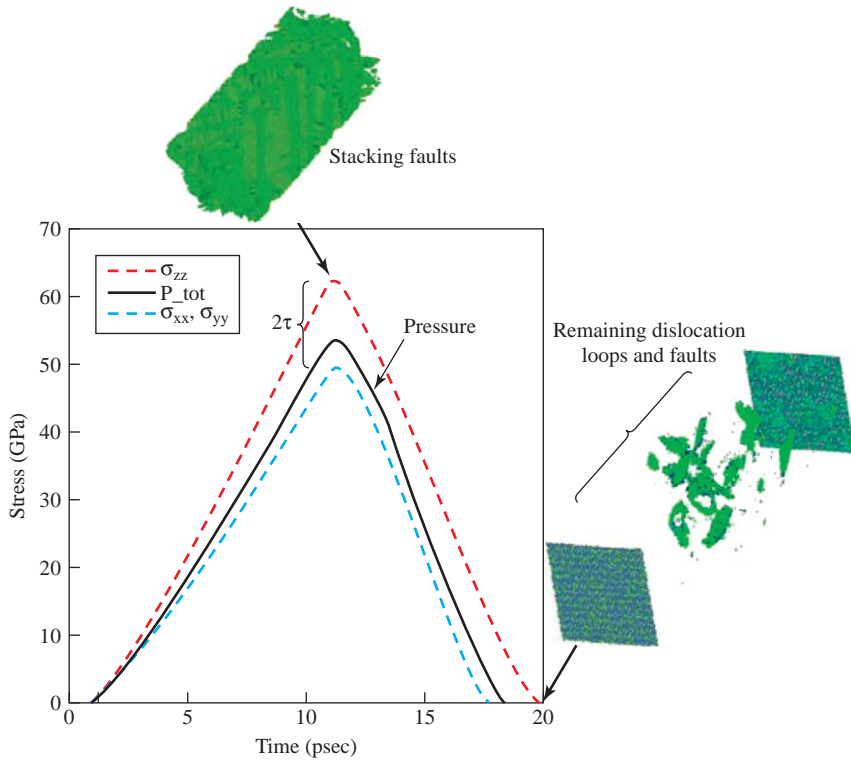
Fig. 59. P_{tot}, σ_{xx}, σ_{yy}, σ_{zz} versus time for monocrystalline Ni, $U_p \sim 1.1$ km/s.

stacking faults was measured, and the resulting residual plasticity was calculated. Fig. 57(b) shows the MD plasticity after release; an order of magnitude drop is evident, consistent with the experimental data by Murr [40]. The pressure rise due to compression and the accompanying drop due to release are shown in Fig. 59 for the case of $U_p = 4.1$ km/s. Only the defective atoms are shown. In experiments, the lower strain rate for unloading and the longer heating period will likely accelerate dislocation annihilation and lead to even lower residual dislocation densities than in our fast unloaded MD simulation.

8.2. MD simulations of shocks in nanocrystalline nickel

Bringa et al. [167] carried out simulations of shocks in nanocrystalline (nc) Cu and found that partial dislocations and grain-boundary sliding dominated at a grain size of 5 nm, with full dislocations contributing more to plasticity as grain size increased up to 50 nm. However, even for these relatively large grains, the number of full dislocations was modest. Shocks in nc Ni, which has a much larger SFE, were expected to give a greater contribution from full dislocations, based on experimental results [175]. The 5 nm grain-sized sample was subjected to piston

velocities between 0.2 and 1.3 km/s, and its Hugoniot was found to be very close to that of the monocrystalline sample. Fig. 60(a) provides an illustration of the shock wave for $U_p = 0.67$ km/s as it traverses the sample (average velocity vs. distance). The corresponding shock pressure within the sample is ~ 38 GPa, which is at the HEL limit for the monocrystalline sample. Since grain boundaries (i.e., defects) exist in the sample, the HEL is significantly lower than that in the single crystal. A single-wave structure is evident and not a two-wave structure as seen in the
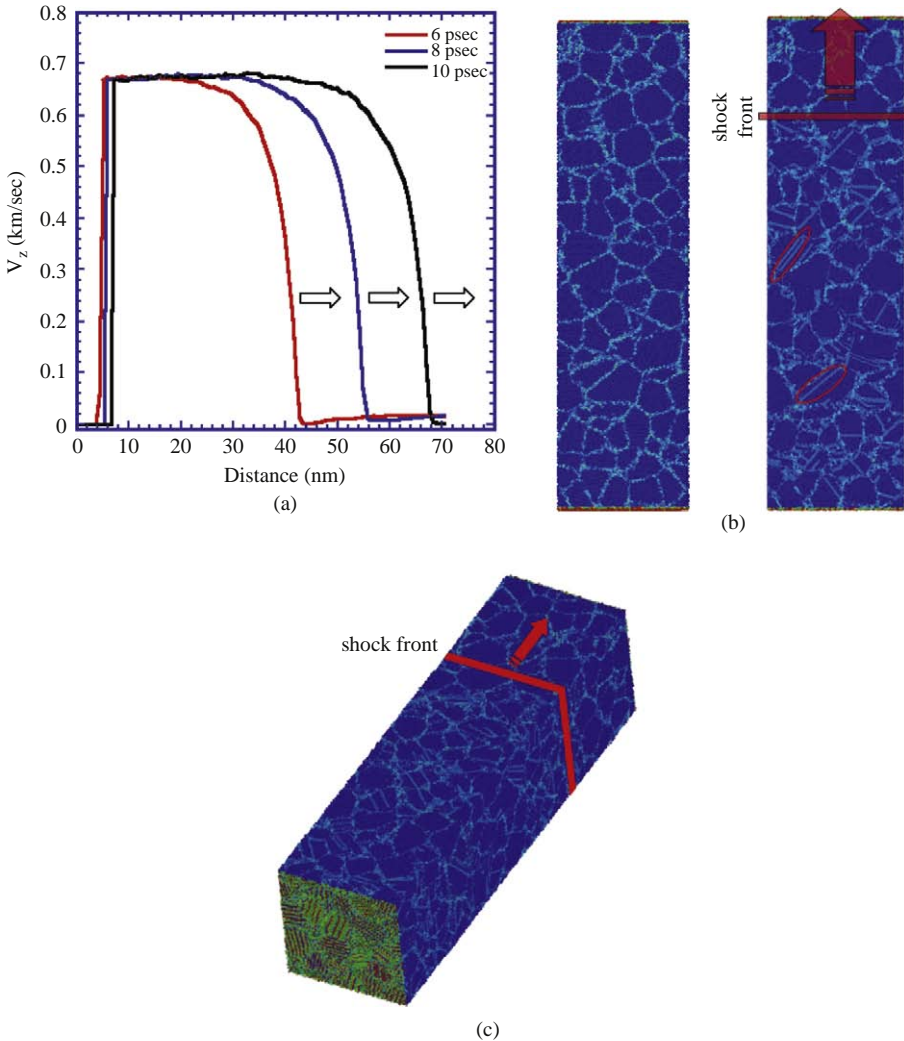

Fig. 60. Shock compression of a nc Ni specimen, with grain size = 5 nm, $U_p = 0.67$ km/s; (a) Z-component of velocity versus distance; (b) 5 nm grain-sized sample at 0 and 10 ps; (c) three-dimensional (3D) view of the sample at 10 ps.

single-crystalline results. This may be due to the fact that the particle velocities vary from grain to grain, introducing fluctuations in the front that do not allow the plastic and elastic components to be resolved. In comparison with the single-crystal profiles shown in Fig. 54(a), the front thickness is increased from ~2 to ~10 nm. Fig. 60(b) shows the nc sample at 0 ps, after it has been relaxed to minimize its internal energy prior to shock propagation (left) and after the shock-wave has traveled for 10 ps (right). Grain boundaries act as sources and sinks for partial dislocations, leaving stacking faults behind as they travel through the grains. Two of these are marked for clarity. This defect configuration is similar to the one observed by Van Swygenhoven et al. [176,177] in homogeneous tension simulations and by Bringa et al. [164,167] in shock simulations. Leading partials are mainly emitted from the grain boundaries, and trailing partials are seldom released. Limited evidence of twinning was also observed. Fig. 60(c) is a 3D view of the simulation shown in Fig. 60(b).

A quantitative analysis of the deformation mechanisms was carried out on MD simulations of three samples of different grain size that were shocked using the same piston velocity of $0.67 \, \mathrm{km \, s^{-1}}$ (~38 GPa): 5 nm Ni, 10 nm Ni, and 10 nm Cu. The three samples provide the means to study the effect of grain size and a different potential on the deformation behavior. We calculated the contributions to the effective strain introduced by shock compression from the various mechanisms of plastic deformation by determining the relative motion between nearest-neighbor pairs of atoms, and resolving this motion along the strain axis, as described by Vo et al. [178]. The procedure to quantify the dislocation contributions to the total plastic strain consists of three steps. The first step locates nearest-neighbor atom pairs that have been sheared on glide planes and assigns local Burgers vectors responsible for the shearing. This step requires correction for the strain caused by atom pairs that are cut by multiple dislocations with different Burgers vectors. The second step distinguishes atoms in grain interiors that are cut by lattice dislocations from those that are involved in grain-boundary mechanisms. The third step evaluates the strain caused by the motion of the dislocations identified. Detailed procedures can be found in Refs [178,179]. Using this method, the contributions from partial dislocations, perfect dislocations, multiple dislocations on the same slip plane, and twinning can be identified. The difference between the total plastic deformation and these other contributions can then be attributed to grain-boundary sliding.

Fig. 61 shows the three shocked samples. The color code is as follows: the blue atoms are not displaced and are in their original minimum energy state, the green atoms are displaced by the Burgers vector of a Shockley partial, the red atoms are displaced by a Burgers vector of a perfect dislocation, and the orange atoms are displaced by a Burgers vector larger than that of a perfect dislocation (due to grain-boundary sliding). Original color illustrations are found in Jarmakani et al. [130]. In these, orange, green, red atoms can be distinguished. For the 5 nm Ni, the total shock strain in the sample was calculated to be ~0.13. The total strain contribution due to dislocations (0.014) is dominated by partials, which makes up ~60% of the total strain due to dislocations; perfect dislocations account for ~10%.
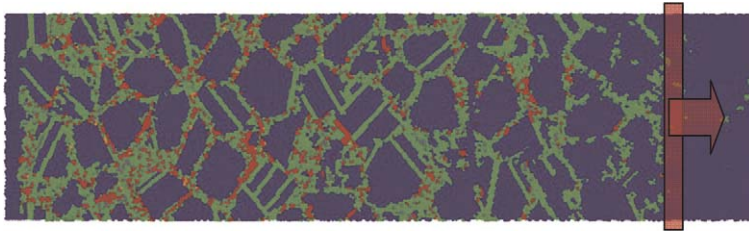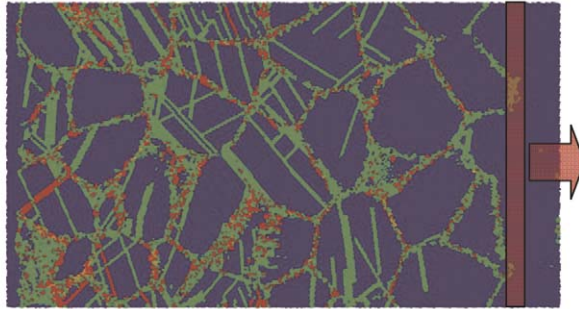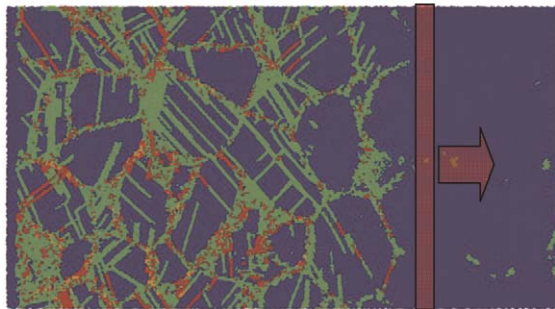
Fig. 61. Comparison of deformation stucture versus grain size for the same particle velocity of $U_p = 0.67$ mm/μs: (a) 5 nm Ni; (b) 10 nm Ni; (c) 10 nm Cu (the position of the shock front is marked for the three samples). Blue corresponds to atoms in their original minimum energy state, green to atoms displaced by the Burgers vector of a Shockley particial, red to atoms displaced by a Burgers vector of a perfect dislocation, and orange to atoms displaced by a Burgers vector larger than that of a perfect dislocation (implying grain-boundary sliding) (Original color illustrations in Jarmakani et al. [130]).

The contribution due to twinning is 26%. By subtracting the strain due to dislocations from the total strain, one obtains the strain due to grain-boundary sliding, 0.116; this represents approximately $\sim 90\%$ of the total strain.

In the case of the 10 nm samples, the strain contribution due to partials is 63% for Ni and 56% for Cu. Perfect dislocations account for 17.2% of the dislocation strain

in Ni and 21% in Cu. The twinning contribution is greater in Cu, 19% as compared to 16% in Ni. The greater incidence of twins is to be expected since the SFE of Cu is significantly lower. However, the difference in the contribution of full dislocations and twinning between Ni and Cu is marginal despite the fact that the SFE of Ni is nearly three times larger than in Cu. This points out to the complexity of dislocation nucleation in nanocrystals, as already pointed out by Van Swygenhoven et al. [177]. Grain-boundary sliding accounts for approximately 58% of the total shock strain in both 10 nm Ni and Cu in comparison with 90% for 5 nm Ni, signifying that it becomes more difficult for larger grains to slide past one another under compression (Bringa et al. [151,180]). Note that the front portions of the 10 nm Cu and Ni samples do not show the grain boundaries highlighted in green. This is due to the fact that no grain-boundary sliding is taking place because the shock front has not yet traveled through that region. The contribution due to partials is comparable in the 5 and 10 nm grain-sized samples, but that from perfect dislocations is greater in the 10 nm samples, as expected. The twinning contribution is greater in the 5 nm grain-sized sample (5 nm Ni: 25.7%, 10 nm Ni: 15.7%), due to the fact that partial dislocations are more abundant, and therefore lead to more twinning as in the Zaretsky model [44] and as described in Shehadeh et al. for single crystals [181]. This result is also in agreement with the models proposed by Chen et al. [182] and Zhu et al. [183], where they show that the propensity for twinning increases with decreasing grain-size. This result for nc twinning behavior is in distinct contrast to the result shown in Fig. 40 for conventional grain sizes, where larger grains twin more readily. Our results are consistent with simulations of tensile deformation of nanocrystals, where grain-boundary sliding was considered crucial at $d \sim 5$ nm (Schiøtz and Jacobsen [184]), mostly based on visual inspection of plasticity and on the observed rotation of certain grains. Recently, Vo et al. [185] carried out simulations of homogeneous uniaxial compression of nc Cu up to 20 nm grain size, and found similar results for the contributions of GB sliding and dislocations, with a cross-over to dislocation dominated plasticity at ~ 15 nm, at a strain rate of $10^{10}\,\mathrm{s}^{-1}$. Our analysis is the first to quantify slip and GB sliding for shocked nc samples.

In addition to the simulations of nanocrystals, laser shock compression experiments were carried out on nc Ni [175,186], with grain sizes between 30 and 50 nm. The samples in the experiments were prepared by electrodeposition at the Lawrence Livermore National Laboratory and were subjected to pressures between 20 and 70 GPa via laser irradiation [130]. The microhardness of the samples after shock compression was measured, and a 5–30% increase after being shocked was observed, clearly indicating dislocation storage. Fig. 62(a) shows a cross-section of a sample with microhardness measurements taken at five positions beneath the cratered surface. Fig. 62(b) shows the increase in residual hardness beneath the cratered surface where a maximum at position 3 occurs where laser intensity (i.e., deformation) is greatest. Fig. 62(c) shows the increase in residual hardness as a function of shock strength during shock compression of the samples. In congruence with the hardness data, TEM examination revealed heavy dislocation activity ($\rho \sim 10^{16}\,\mathrm{m}^2$) due to these laser-induced shocks. Full dislocations

(a)

(b)

(c)
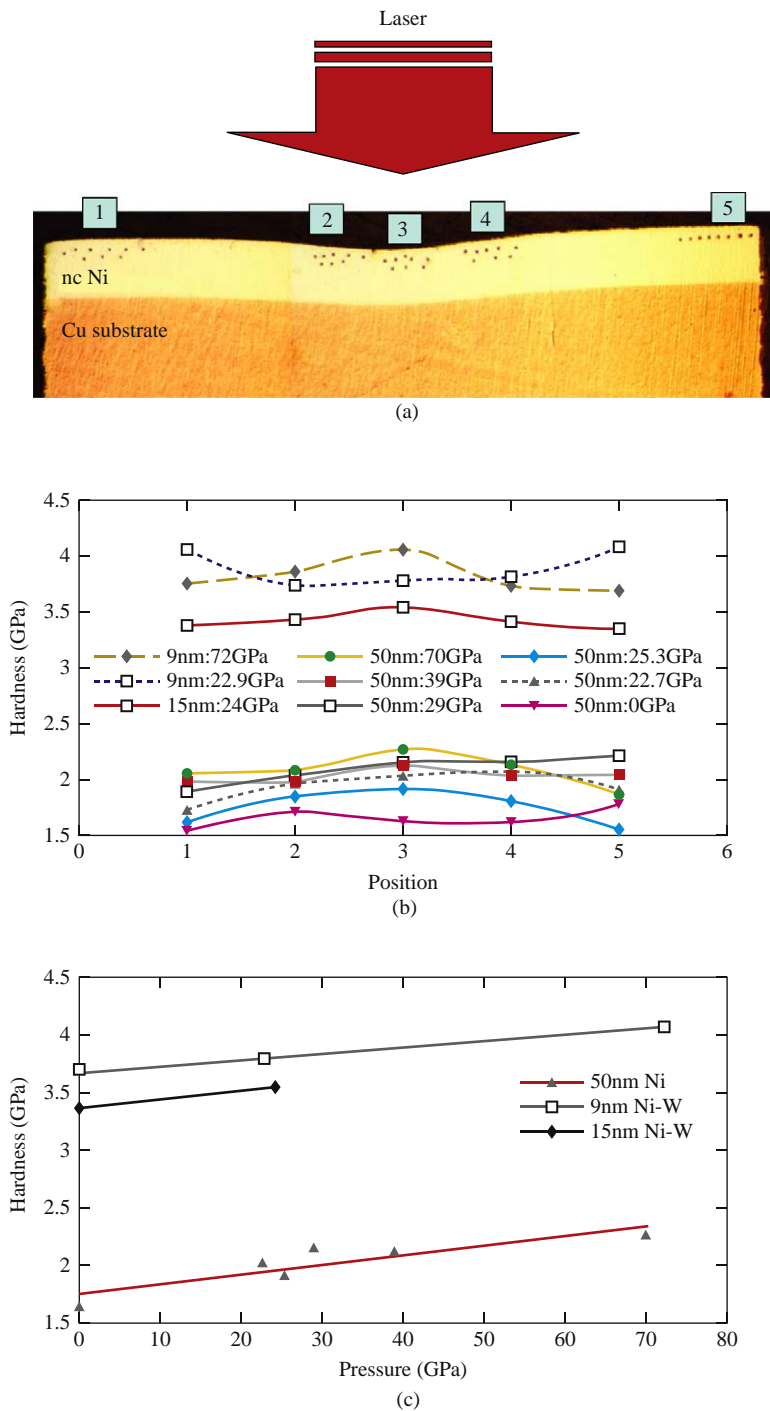
Fig. 62. (a) Cross-sectional microhardness measurements from five positions beneath the laser-shock induced crater; (b) hardness veruss position; (c) hardness versus shock pressure.

were the main carriers of plasticity [see Fig. 63(a)]. Interestingly, deformation twins were not observed in any of the samples, even at pressures up to 70 GPa. This is discussed in Section 6.

To further reduce the grain size to ~ 10 nm, tungsten (13 wt.%) was added to the nickel electrolyte during electrodeposition as outlined by Schuh et al. [187,188].
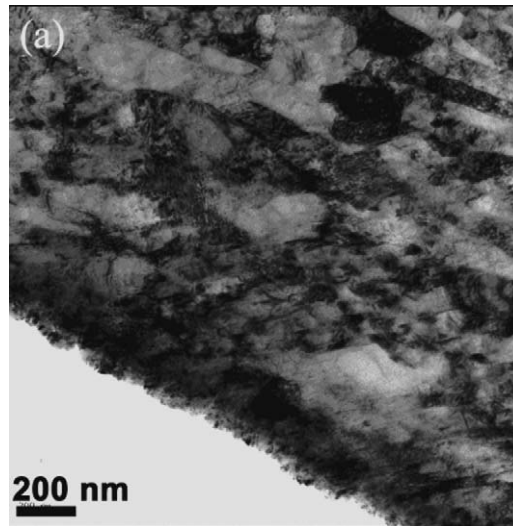
(a)
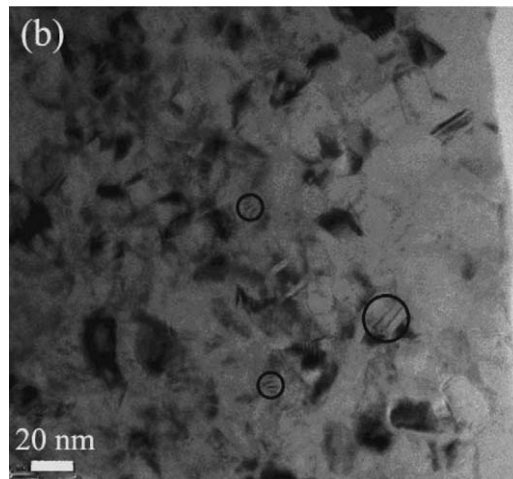
(b)

Fig. 63. (a) TEM image of nc Ni with grain sizes of 30–50 nm shocked at ~ 40 GPa showing dislocations; (b) TEM image of Ni–W (13 at.%) with grain sizes of 10–15 nm shocked at ~ 40 GPa; deformation twins are evident (circles) (Courtesy Y. M. Wang; from Jarmakani et al. [130]).

The Ni–W samples were loaded to pressures up to ~ 38 GPa, and a shift in deformation mechanisms was observed. TEM analysis revealed that deformation twins were the predominant defect structures, indicated by circles in Fig. 63(b). A very low density of pre-existing annealing twins was observed in the as-prepared samples, and the twin density increased dramatically after shock loading. However, the addition of W lowers the SFE, and the increased twinning cannot be attributed to the decreased grain size alone.

This discrepancy in dislocation behavior between MD simulations and actual experiments could be due to several factors. The samples in the experiments go through release, which leads to the annihilation and reabsorption of partials. There may be grain-size effects at play. Smaller grains favor partial dislocations, and one may have to go to larger grain sizes for perfect dislocations to be energetically favorable. For instance, Bringa et al. [167], showed significant dislocation activity and dislocation junctions being formed only for grains above 20 nm. In addition, the MD potentials may not be very accurate in describing the stacking-fault and twinning energy surfaces, and the value of these surfaces under stress could change considerably. Another possibility may be that the time needed for the emission of full dislocations is much longer than the timescales simulated in MD. Loading and unloading in the laser-shock experiments take place over 1–10 ns, whereas the MD simulations are in the range of picoseconds, only capturing the initial stages of deformation, and at much higher strain rate. Warner et al. [189] recently showed that a full dislocation takes much longer than partials and twins to be emitted from a crack tip, and something similar may be happening in nc materials.

8.3. Effect of unloading on nc Ni

In an analogous manner to the unloading MD simulations carried out on monocrystals (Fig. 59), the effect of unloading on the deformation structure of nc Ni was studied to provide a more realistic comparison with the experiments [130]. The sample shocked at 38 GPa, $U_p = 0.67$ km/s, was allowed to unload and the dislocation behavior within the grains was analyzed. Fig. 64(a) shows the average pressure within the sample as a function of time as it is loaded and unloaded. Fig. 64(b) shows the sample at 0 ps (before the shock), at maximum compression at 11 ps (first picoseconds consisted of equilibration) before it is unloaded, and 18 ps after it has been unloaded to zero pressure. The principal features are stacking faults, which are mostly emitted from grain boundaries during compression. After unloading, $\sim 38\%$ of the partials are reabsorbed. The light ellipses show regions where partials are reabsorbed and the dark ellipses indicate the partial dislocations that survive after unloading. Unloading at experimental, much slower, rates may lead to further reabsorption. The reabsorbtion of partials causes the contribution due to perfect dislocations to increase from 10.3% before unloading to 18.2% after unloading. As expected from the loading simulations of nc samples, grain-boundary sliding dominates the plasticity for $d = 5$ nm. The phenomenon of reabsorption

(a)

(b)
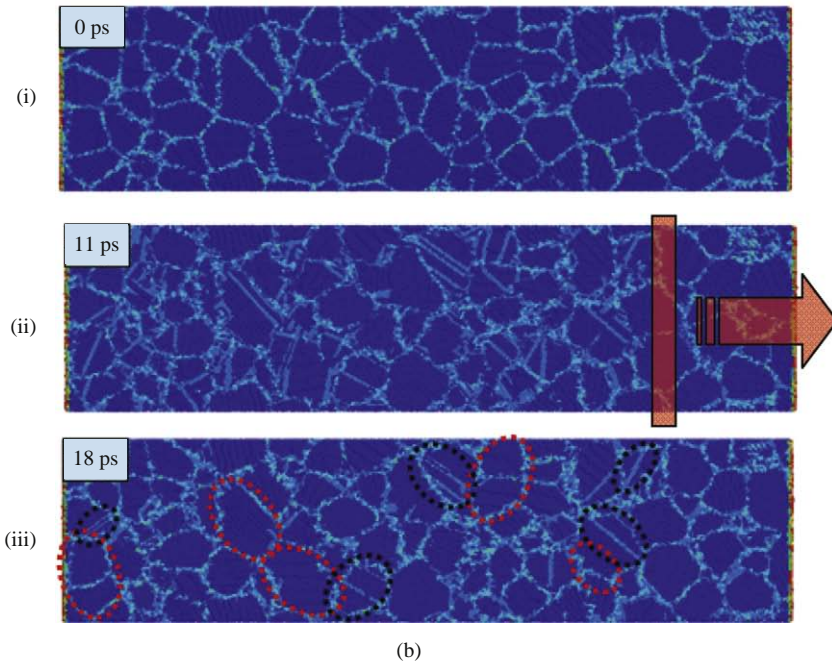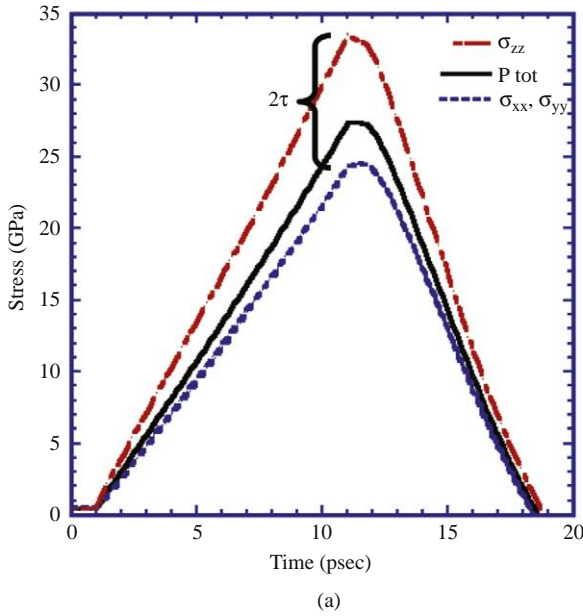
Fig. 64. (a) Average pressure rise and release in a nc Ni sample for $U_p = 0.67$ km/s; (b) deformation features in the nc Ni sample (i) before compression, (ii) at maximum compression, and (iii) after release back to zero pressure.

would explain the fact that partial dislocations are not observed in our experiments, only full dislocations. In addition, Bringa et al. [180] observed dislocation junctions forming inside grains with $d = 50$ nm, but never forming for smaller grains. Such junctions in larger grains might survive unloading.

For comparison, a smaller sample having $\sim 500{,}000$ atoms and dimensions of $17.6 \times 17.6 \times 17.6$ nm was compressed uniformly in uniaxial strain to a pressure of ~ 38 GPa and then allowed to unload. The final strain and strain rate applied were roughly the same as that experienced by the shocked sample, the principal difference being that there is no wave propagation in the latter simulations. Fig. 65(a) shows the average pressure within the sample as a function of time. The sample was compressed uniaxially for 4 ps to a strain of 0.13, held there for 10 ps, and released back to 0 strain within 4 ps. Fig. 65(b) shows the various stages of deformation. Partials are emitted and reabsorbed during this process. There are no major differences in defect distribution between uniform and shock compression. The percentage of strain corresponding to grain-boundary sliding is slightly decreased. Interestingly, approximately 39% of the partials disappear after unloading. Before unloading, grain-boundary sliding accounts for 79.2% of the total strain, in comparison with shock compression (90%).

9. Simulations of loading at different strain rates

MD simulations of shocks generally deal with square loading pulses. This leads to extremely high strain rates at the shock front, $\sim 10^{10}\,\mathrm{s}^{-1}$. In order to assess the effect of ramped pulses, Bringa et al. [167] carried out simulations with and without a ramp of 50 ps and a peak pressure of 35 GPa, slightly above the threshold for homogeneous nucleation of dislocations for the EAM Cu by Germann et al. [154]. They studied the influence of strain rate in the transition from a 1D compressed state to a quasi-3D compressed state, as shown in Fig. 66. Simulations found no difference between the ramped and unramped cases for a perfect single crystal. However, when dislocation sources were introduced, the ramp loading activated the sources before homogenous nucleation occurred, as shown in Fig. 67, and led to an early relaxation of the shear stress. This relaxation led in turn to a lower dislocation density in the region where homogeneous nucleation occurred once the peak pressure was reached. Despite the fact that the dislocation density was lower, stress relaxation was higher, because dislocation mobility was not impeded by the larger number of junctions produced at higher density. This is shown schematically in Fig. 68.

In order to simulate larger systems for longer times, Shehadeh et al. [190] have carried out dislocation dynamics embedded into finite element simulations of shock loading, where plasticity is due to dislocation multiplication by pre-existing sources [190,191]. A criterion for homogeneous nucleation was added to model high pressure by fitting MD results [181]. Results are shown in Fig. 69. They also found that lower strain rates lead to lower dislocation densities, as shown in Fig. 70, in agreement with experimental results by McNaney et al. [135]. Recent simulations by Hawreliak et al. [192], using a rise time of 300 ps and a sample of $\sim 4\,\mu\mathrm{m}$ along

(a)

10 ps   12 ps   14 ps

19 ps   24 ps   26 ps

28 ps
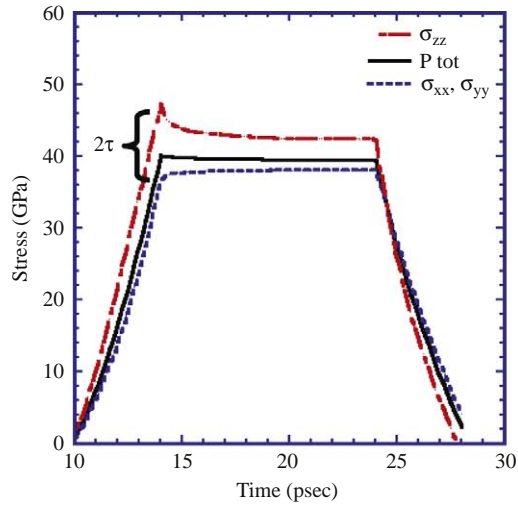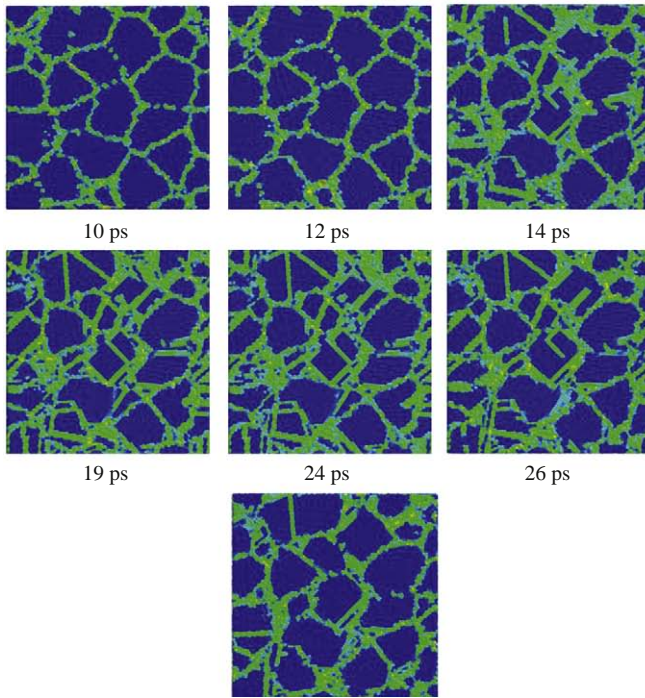
(b)

Fig. 65. (a) Uniaxial compression and relaxation of 5 nm grain-sized Ni sample; (b) frames at different times showing emission and annihilation by reabsorption of partial dislocations into grain boundaries.
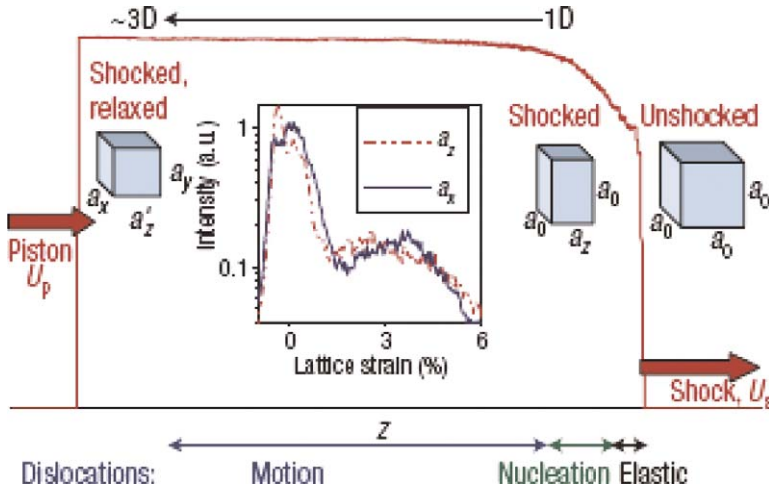
Fig. 66. Dynamic lattice compression during shock loading. The upper curve shows the particle velocity versus time behind a shock front moving to the right (z direction) at speed U_s. The response of an initially cubic unit cell of side a_0, is illustrated schematically by the blocks. The initial strain is uniaxial compression (1D), with $a_z < a_0$ and $a_x = a_y = a_0$ and large internal shear stress. The lattice responds by relaxing via volume-preserving dislocation flow to a more 3D-symmetric compression, $a_z \sim a_x \sim a_y$. The inset shows experimentally measured diffraction data with a peak corresponding to the unshocked material at zero strain and a peak corresponding to prompt (subnanosecond) 3D relaxation ($a_z \sim a_x$) for shocked copper at 3–4% strain, from Loveridge-Smith et al. [193]. Figure from Bringa et al. [167], where full colors are given.

the shock direction, showed that a large fraction of their Cu sample was kept solid at 3 Mbar, well above the shock-melting pressure of 2 Mbar, because of their off-Hugoniot loading.

10. Incipient spallation and void growth

The study of the nucleation and growth of voids in ductile metals is of significant interest for the understanding of failure under overall tensile loading. Such failure, for example, can occur upon reflection of tensile waves from a free surface of the shock-compressed plate. Material failure by void growth under dynamic loading conditions leads to spalling. Extensive analytical and computational research has been devoted to analyze ductile void growth and coalescence in various materials and under various loading conditions. Seitz [194] and Brown [195] postulated prismatic loops forming at the interface between a rigid particle and its matrix. In related work, Silcox and Hirsch [196] analyzed the dislocations that form the boundaries of stacking-fault tetrahedra in gold. These tetrahedra had sizes of approximately 35 nm. Later, Humphreys and Hirsch [197] analyzed copper-containing small alumina particles and observed the formation of prismatic loops
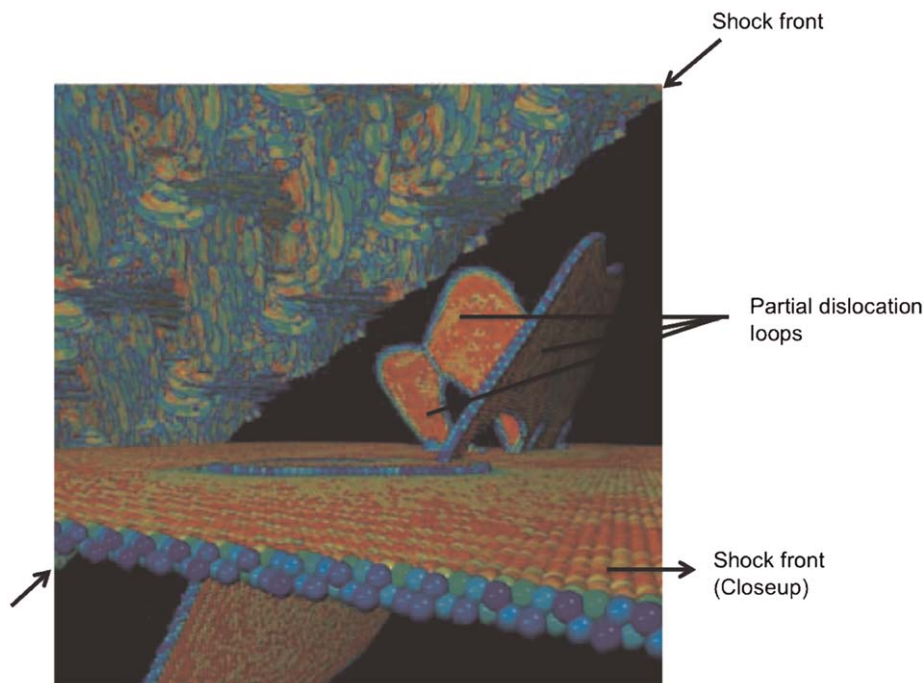
Fig. 67. Snapshot from our molecular dynamics (MD) simulation of a shock wave moving in the $[1\,0\,0]$ direction of single crystal Cu, with a maximum pressure of 35 GPa and a load rise time of 50 ps. The shock propagates approximately toward the bottom right of the figure. The simulation includes 256 million atoms, but only defective atoms are shown with a coloring scheme following the centro-symmetry deviation values. This close-up view shows a dislocation source activated by the ramp, producing partial dislocation loops in several available {1 1 1} planes. The ''butterfly'' shapes result from loops colliding and forming sessile junctions that impede dislocation motion. The top of the loading ramp is strong enough to induce homogeneous nucleation of dislocations, and this is the front seen behind the source, with an extremely high dislocation density. From Bringa et al. [167].

by a cross-slip mechanism. This study involved primarily the interaction of existing dislocations with rigid particles. More recently, Uberuaga et al. [198] observed the direct transformation of vacancy voids to stacking-fault tetrahedra by MD. In the area of initiation and growth of voids under tensile loading, there are only a few dislocation-based mechanisms (Wolfer et al. [199]).

   This section describes an alternative mechanism of void growth by dislocation emission from the surface of the void (Lubarda et al. [200]). We show analytically for a 2D configuration, that the imposed stresses in the laser shock experiments are sufficient for emitting dislocations from the void surface. The critical stress for dislocation emission is found to decrease with an increasing void size, so that less stress is required to emit dislocations from larger voids. Fig. 71 shows SEM images of (a) the initial specimen and (b) the recovered specimen with the bulged bottom surface. The laser-induced shock was driven from the upper surface. The reflected
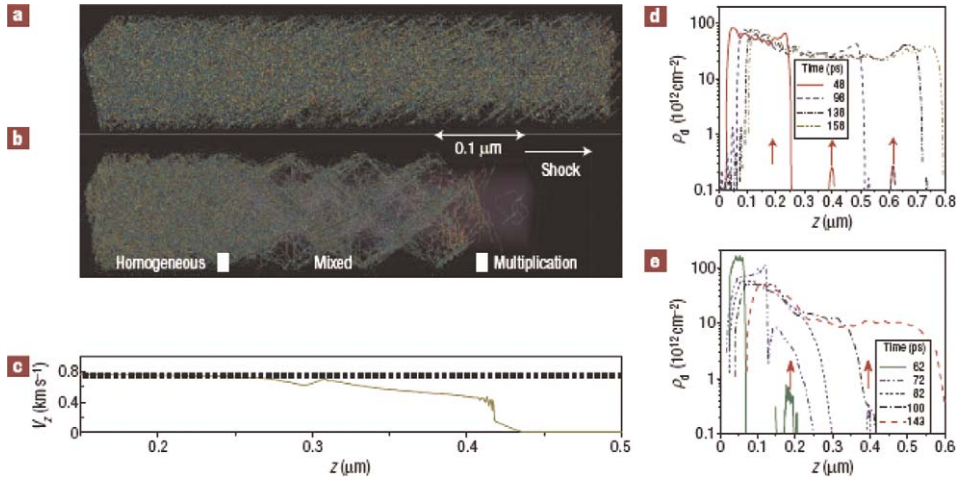
Fig. 68. Dislocation structure resulting from MD simulations of shocked [1 0 0] copper. (a) Snapshot of a simulation with a shock drive of 0 ps rise time after $t \sim 100$ ps, showing only dislocation atoms. (b) The same as (a) except that the shock drive had a 50 ps linear-ramp rise time. In both cases, the copper crystal included pre-existing dislocation sources. The three regions of dislocation activity – homogeneous, mixed, and multiplication – are marked. (c) The particle velocity, V_z, profile for the ramped shock, where the ramp extends over $z = 0.29$–0.43 μm. (d, e) The resulting dislocation density profiles for the 0 ps rise-time case (d) and the ramped case (e). The locations of the pre-existing sources are illustrated by vertical arrows. From Bringa et al. [167].

tensile pulse at about 100 μm from the rear surface can be calculated from the decay of the shock pulse. It is equal in magnitude, but opposite in sign, to the shock pressure. The latter is about 5 GPa in magnitude. Voids were observed in the cross-section, ranging in size from 25–50 nm to 1 μm. Fig. 72 is a TEM image showing what is believed to be a void near the back surface of the shocked specimen. Its diameter is approximately 500 μm. It may be argued that electropolishing produced the void, but a larger number of perforations were found close to the back surface of the specimen, where void formation is expected. There is a light rim around the void, indicating an extremely high dislocation density, below the resolution where individual dislocations can be imaged. This void is similar to the one observed earlier by Christy et al. [201] using high-voltage transmission electron microscopy. In that experiment, the foil was not perforated and the same intense dislocation density was observed. The diameter of this work-hardened layer is approximately twice the void diameter. Thus, a much higher dislocation density characterizes the region surrounding the void compared to regions without observable voids.

10.1. Dislocation emission and void growth

Void growth is indeed a non-homogeneous plastic deformation process. The plastic strains decrease with increasing distance from the void center. The far-field strains
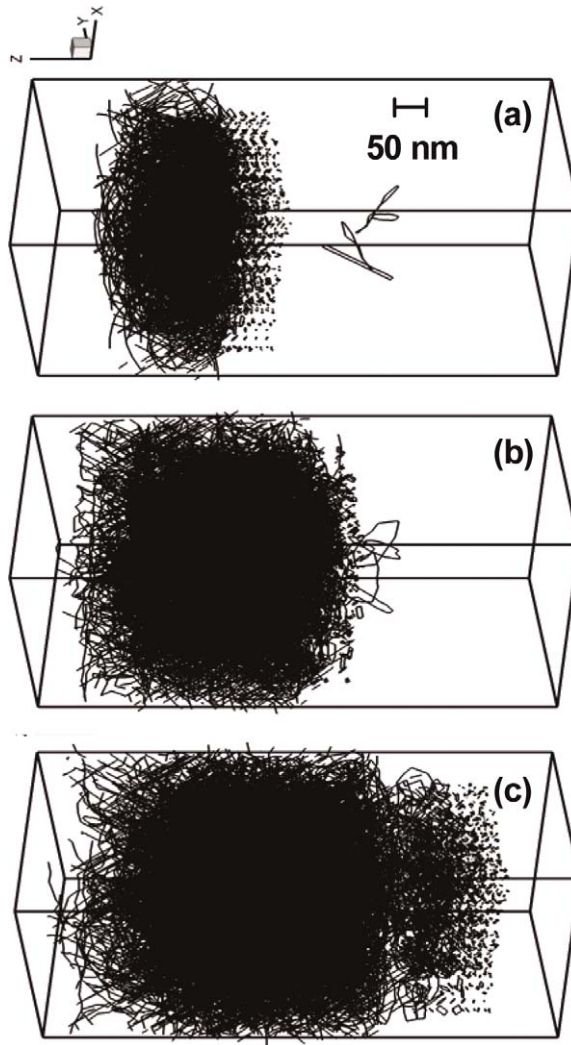
Fig. 69. Multiscale dislocation dynamics plasticity (MDDP) simulation of a 35 GPa, 50 ps rise time shock wave, showing individual dislocations for a block of $0.25 \times 0.25 \times 10 \,\mu m^3$. The shock-front moves from left to right. Loops are homogeneously nucleated as the wave travels through the material, while those previously nucleated grow as the crystal relaxes. Dislocation–dislocation interactions become dominant at high ρ, leading to the development of a 3D pattern of intersecting loops in all available {1 1 1} slip planes, with large numbers of jogs and junctions. (a) 67 ps: Pre-existing loops that will act as dislocation sources can be seen ahead of the shock front, (b) 90 ps: Initial stages of heterogeneous nucleation from the sources, and (c) 122 ps: There is a region with both homogeneous and heterogeneous nucleation, showing lower dislocation density than the region with only homogeneous nucleation. From Shehadeh et al. [190,191].
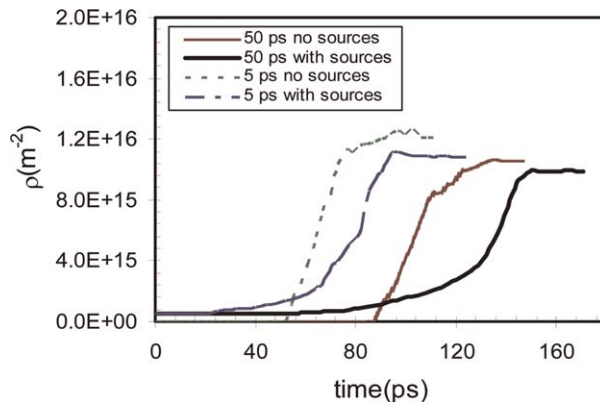
Fig. 70. Evolution of the average dislocation density within a thin slice calculated using MDDP simulations of 35 GPa shocks for 5 and 50 ps rise times. The initial dislocation microstructure affects the homogeneous nucleation (HN) process only at the early stages of the interaction process. The relaxed density of dislocations is affected by the shock wave rise time and the pre-existence of dislocation sources. From Shehadeh et al. [190].

are purely elastic, whereas plastic deformation occurs in the regions adjoining the surface of the void. Ashby [202] developed a formalism for the treatment of a non-homogeneous plastic deformation by introducing the concept of the generation of geometrically necessary dislocations. Two different mechanisms were envisaged by Ashby [202], based on prismatic or shear loop arrays. The void growth situation is quite different from the rigid-particle model used by Ashby [202]. One can still postulate arrays of line defects to account for the non-homogeneous plastic deformation. Of critical importance is the fact that the shear stresses at 45° to the void surface are maximum, since the normal stresses are zero at the surface of the void. These shear stresses decay to zero at large distances due to the assumption of a far-field hydrostatic stress state. Thus, the shear stresses are highest at the internal surface, triggering dislocation nucleation there. The mechanism of void growth derived by Lubarda et al. [200] for the emission of shear loops will be presented here.

The *shear loop* mechanism involves the emission of dislocations along the slip plane S, and is shown in Fig. 73(a). These loops form preferentially at planes intersecting the void along a 45° orientation to the radius. Fig. 73(b) shows two slip planes intersecting the void surface at 45°. This ensures a 45° angle between the slip plane S and the void surface, maximizing the driving force on the dislocation. The difference between this and the Ashby [202] loops is that the two opposite loops have dislocations of the same sign whereas Ashby's [202] opposite loops have opposite signs (Figs 73 and 74).

In the 2D case, four pairs of edge dislocations emitted from the surface of a cylindrical void under remote uniform tension give rise to an increase of the average void size by an amount approximately equal to the magnitude of the

(a)

Laser shock

Spall

(b)
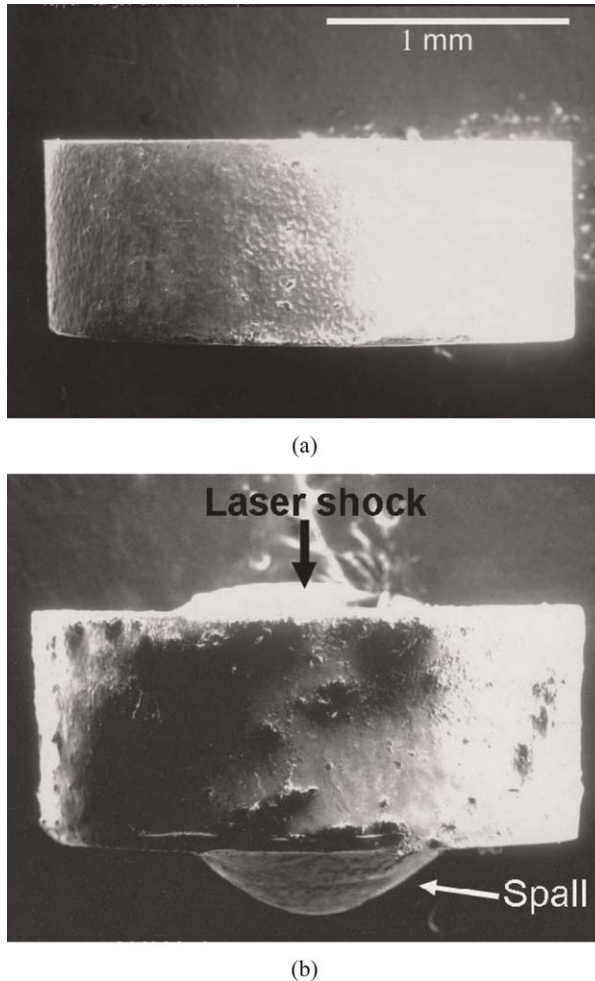
Fig. 71. A side view of the cylindrical specimen subjected to shock compression and subsequent tensile pulse reflection from the laser-induced shock wave: (a) Undeformed specimen, and (b) deformed specimen upon wave reflection with spall surface protruding in back.

dislocation Burgers vector. Other arrangements, involving more than four pairs of dislocations, can also be envisioned as giving rise to the expansion of the void [203]. After the void has grown a finite amount, the network of sequentially emitted dislocations may appear as depicted in Fig. 74. In an analytical treatment of the void growth by dislocation emission, we consider the emission of a single dislocation pair (shear loop) from the surface of a cylindrical void under far-field biaxial tension. The critical stress required for the emission of a shear loop is calculated as a function of the material properties and the initial size of the void. The analysis is
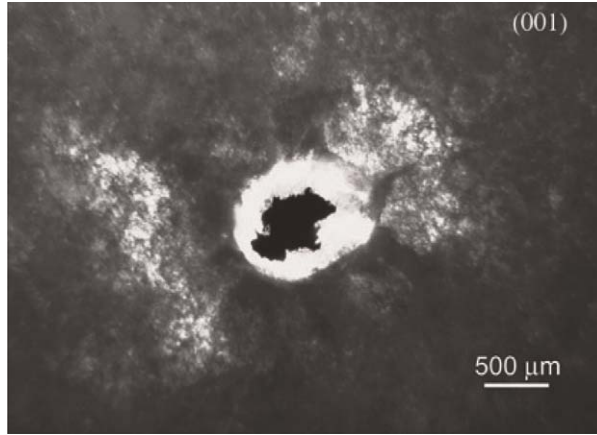
Fig. 72. Dark field image of an isolated void and associated work-hardened layer near the rear surface of the specimen.

based on the criterion adopted from a related study of the crack blunting by dislocation emission (Rice and Thomson [204]). It is shown that the critical stress for dislocation emission decreases with increasing void size, so that less stress is required to emit dislocations from larger voids. At constant remote stresses, this would imply an accelerated void growth by continuous emission of shear dislocation loops. However, this is opposed by an increasingly thick work-hardened layer.

The 2D problem was solved analytically by Lubarda et al. [200] and is presented here in a succinct fashion. Consider an edge dislocation near a cylindrical void of radius R in an infinitely extended isotropic elastic body. The dislocation is at a distance d from the stress-free surface of the void, along the slip plane parallel to the x axis. The stress and deformation fields for this problem have been derived by Dundurs and Mura [205]. The interaction energy between the dislocation and the void is:

$$E_{\text{int}} = \frac{Gb^2}{4\pi(1-v)} \left[\left(\frac{x^2}{(x^2+y^2)} \right) + \ln\left(\left(\frac{x^2+y^2}{x^2+y^2-R^2} \right) \right) \right] \left(y = \frac{R}{\sqrt{2}}, \right. \tag{51}$$

where b is the magnitude of the Burgers vector of the dislocation, G the elastic shear modulus, and v Poisson's ratio of the material. The shear stress along the considered slip plane acting on a dislocation due to the pressure of the far-field hydrostatic stress σ is equal to:

$$\tau = \sqrt{2}\sigma \frac{\xi}{\left((\xi+(1/2))^2\right)}, \tag{52}$$

where $\xi = x/R$.

(a)

(b)
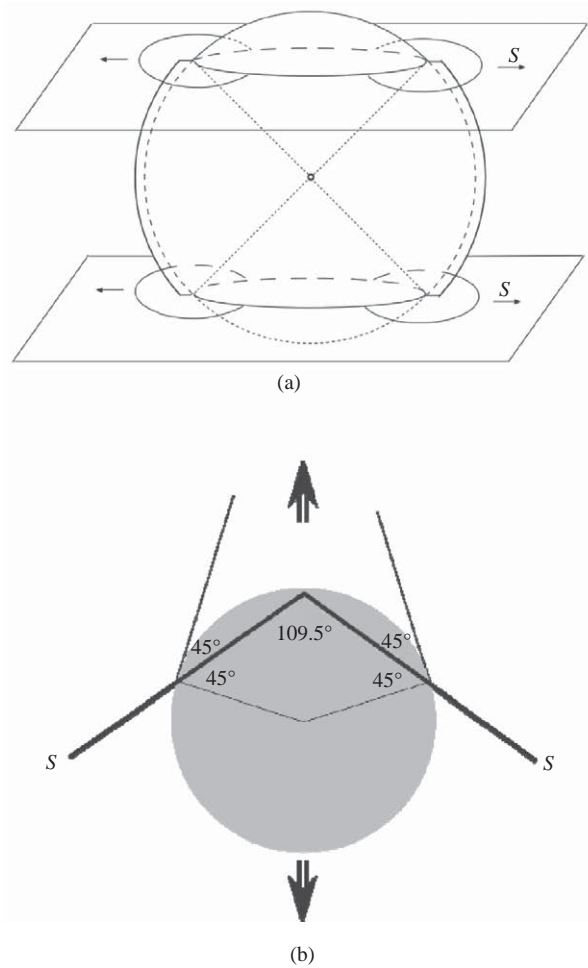
Fig. 73. Shear loop mechanism for the growth of voids. (a) Emission of two pairs of dislocation shear loops from the void surface along the indicated slip planes, S. (b) Two slip planes intersecting the void surface at 45°, the orientation that maximizes the force on the dislocation.

The total force on the dislocation due to both the applied stress and the interaction with the void (derivative of eq. (54)) is:

$$\frac{F_x(\xi)}{Gb} = \frac{\xi}{(\xi^2 + (1/2))^2} \left[\sqrt{2}\frac{\sigma}{G} - \frac{1}{\pi(1-v)}\frac{b}{R}\frac{\xi(\xi^4 + (1/4))}{(\xi^4 - (1/4))} \right] \cdot \left(\right. \tag{53}$$

The normalized force, F_x/Gb, versus the normalized distance, d/b, plot is shown in Fig. 75 for the case when $R = 40b$, $\sigma = 0.1\ G$, $v = 0.3$ and $d = x - R/(2^{0.5})$. The dislocation feels the maximum force of repulsion (from the void) at a position of $d \approx 2.11b$. For d smaller than ~ 1b, $F_x/Gb < 0$ and the dislocation is attracted
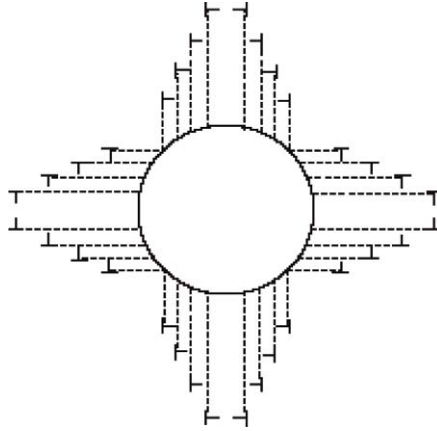
Fig. 74. Network of sequentially emitted shear loops.
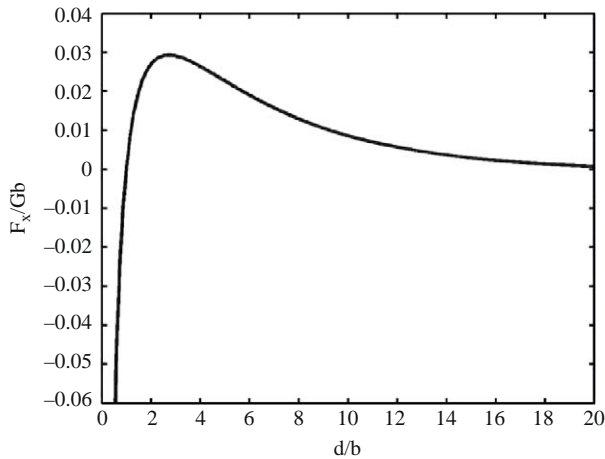
Fig. 75. Normalized dislocation force F_x/Gb versus normalized distance from the void d/b, according to eq. (56), for $R = 40\,b$, $\sigma = 0.1\,G$, and $v = 0.3$. The dislocation feels a maximum force of repulsion (from the void) at a position of $d/b = 2.1$.

to the void. For $d > \sim 1b$, $F_x/Gb > 0$, and the dislocation is repelled from the void. In the limit $d/b \to \infty$, the force on the dislocation vanishes since the dislocation is far from the void, and finds itself in the field of uniform biaxial tension σ.

In the equilibrium dislocation position, the attraction from the void is balanced by the applied stress, so that the force $F_x(\xi)$ in eq. (56) vanishes, that is,

$$\frac{\sigma}{G} = \frac{b/R}{\sqrt{2\pi}(1 - v)} \frac{\xi(\xi^4 + 1/4)}{(\xi^4 - 1/4)} \tag{54}$$

This was done using the Rice and Thomson [204] criterion for the spontaneous emission of a dislocation from a crack tip. The stress required to emit a dislocation is:

$$\frac{\sigma_{cr}}{G} \geq \frac{b/R}{\sqrt{2}\pi(1-v)} \frac{(1+\sqrt{2})(\rho b/R)^4 + 1}{(1+\sqrt{2})(\rho b/R)^4 - 1}. \tag{55}$$

The plot of σ_{cr}/G versus R/b is shown in Fig. 76 for a selected value of the material parameter, $R_{core}/b = \rho = 4.0$. It should be noted that ρ is the ratio between the radius of the core and the Burghers vector and not the dislocation density, as in previous sections. The results are meaningful for sufficiently large sizes of voids, typically $R > 3\rho b$ ($R > 3b–6b$). The critical stress required for dislocation emission decreases both with increasing ρ and R/b. The smaller the dislocation width, the higher the applied stress must be to keep the dislocation in equilibrium near the void. It is noted that the force on the dislocation at a given equilibrium distance from the void due to a remote stress increases more rapidly with the ratio R/b than does the force due to attraction from the void surface. More involved dislocation models based on the Peierls–Nabarro concept, as used by Rice [206] and Rice and Beltz [207] to study the crack blunting by dislocation emission, or by Xu and Argon [126] in their study of the homogeneous nucleation of dislocation loops in perfect crystals, may be needed to further improve the analysis of the void growth by dislocation emission. The model agrees extremely well with MD simulation data, both for void growth [203,208], shown in Fig. 76, and for void collapse (Davila et al. [209]).

Experimental data in the literature (e.g., Minich et al. [210]) indicate that the spall strength of high purity Cu single crystals is about 5 GPa. The spall strength of a polycrystalline Cu is about half that value, because of grain boundaries and intercrystalline defects, which promote void growth. Meyers and Zurek [211] and
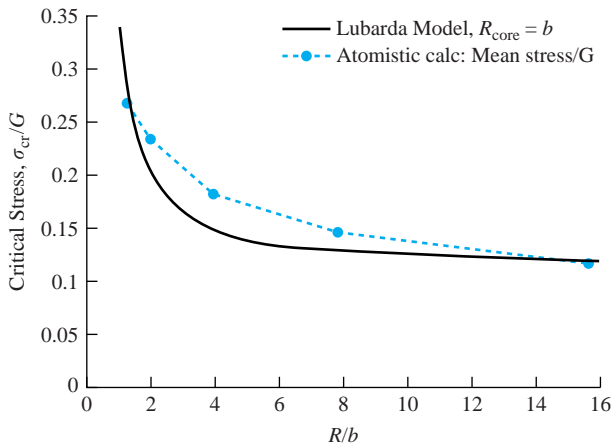


Fig. 76. Normalized critical stress σ_{cr}/G required to emit a dislocation from the surface of the void versus normalized radius of the void R/b, according to eq. (56) ($v = 4/3$, $R_{core}/b = 4$) and according to MD calculations. Adapted from Meyers et al. [203].

Meyers [212] discuss the effects of polycrystallinity and grain size on void growth during spall experiments and reconcile the contradictory results. The higher spall strength observed for monocrystalline copper is due to different nucleation sites. In polycrystals, there is segregation of impurities at the grain boundaries, providing favorable initiation sites. In monocrystals, these sites are absent and initiation must occur from vacancy complexes.

The 2D picture is somewhat more complex than the 1D one. Dislocation loops are emitted circumferentially around a void, along a plane intersecting it at 45°. Six loops, corresponding to the edge dislocations with directions $[1\,\bar{1}\,0]$, $[1\,0\,\bar{1}]$, $[0\,1\,\bar{1}]$, $[\bar{1}\,1\,0]$, $[\bar{1}\,0\,1]$, and $[0\,\bar{1}\,1]$, are shown in Fig. 77(a). As they expand, their extremities approach each other and eventually react; this is energetically favorable under zero-stress conditions:

$$Gb_1^2 + Gb_2^2 \geq \cancel{Gb_7^2}. \tag{56}$$

The dislocations that form on reaction have a screw character. Successive loops can form on the same $(1\,1\,1)$ plane, as shown in Fig. 77(c), or on adjacent planes, as the void grows.
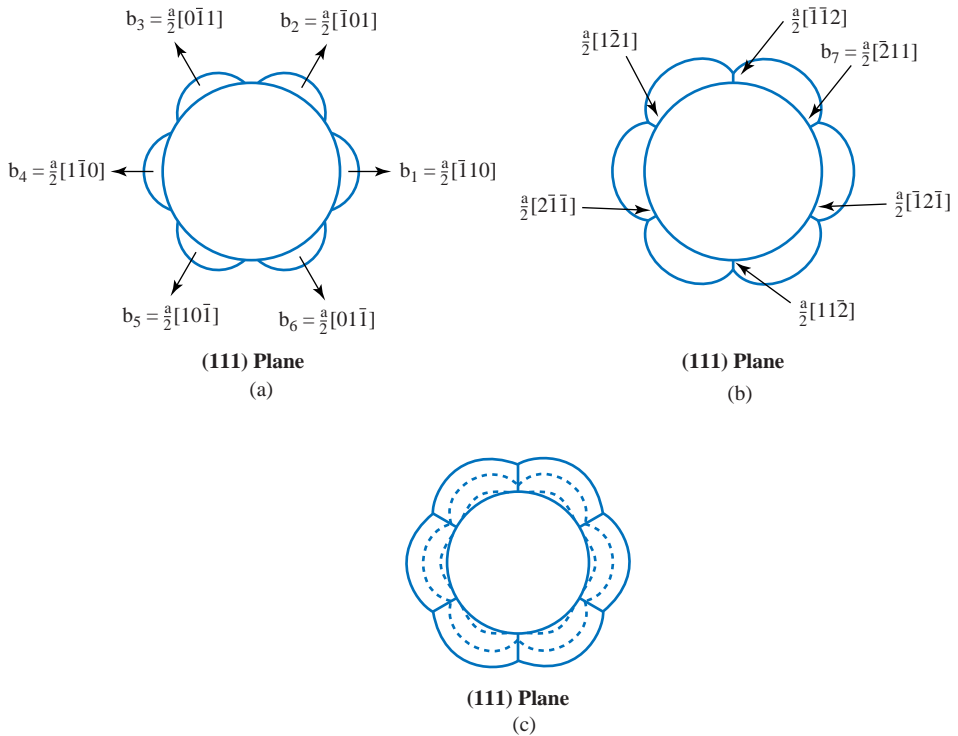

Fig. 77. (a) Six edge dislocation loops forming at the intersection of the void surface and the $(1\,1\,1)$ slip plan in a void subjected to hydrostatic expansion; (b) reactions between adjacent dislocation loops as they expand; (c) successive emission of loops. Adapted from Traiviratana et al. [203].

The intersection of a void with eight {1 1 1} slip planes at 45° forming an octahedron, is shown in Fig. 78. The dislocation interactions become rather complex at that level. Traiviratana et al. [208] analyzed the more complex situation in which the perfect dislocations formed partials. In this case, one has to consider the reactions between the leading partials and the reactions between the trailing partials.

Several researchers have simulated void growth using MD simulations [209,213–219]. Rudd, Seppälä, and Belak [216–219] were primarily interested in void growth and did not focus on the dislocations. Potirniche et al. [214] used a uniaxial stress
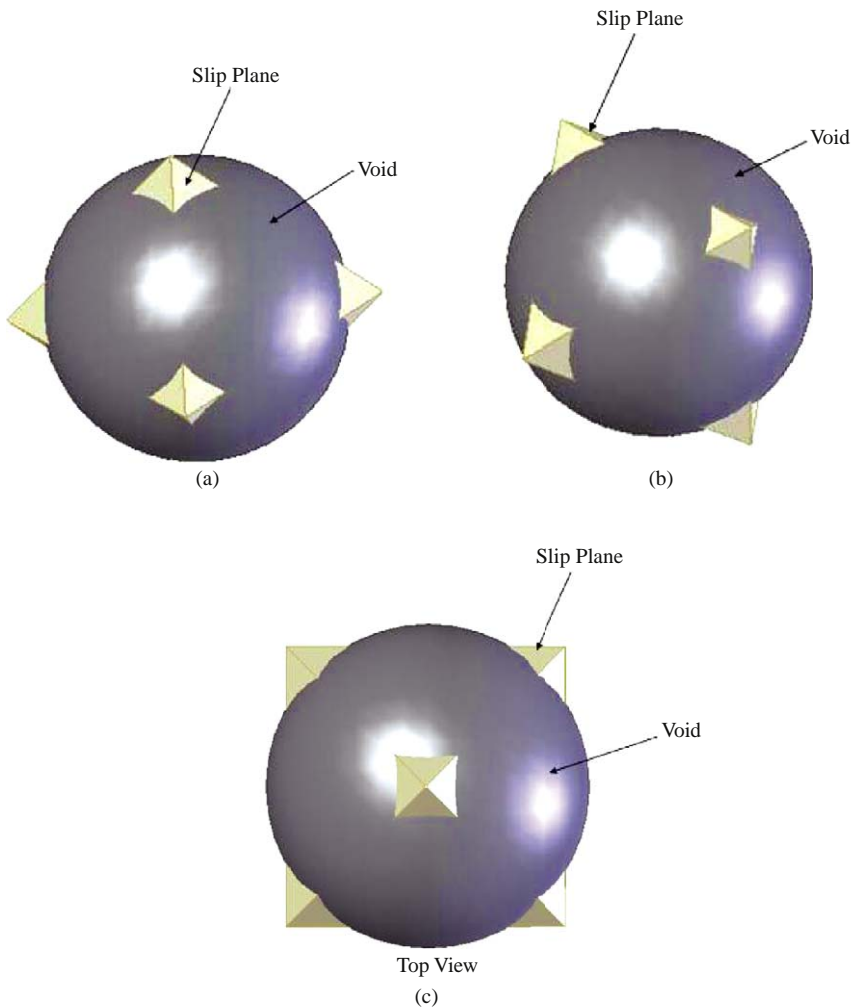

Fig. 78. (a) 3D model of a spherical void intercepting the eight slip planes that form an octahedron. (b) Another view of the 3D model of spherical void intercepting the eight slip planes. (c) Top view of the 3D model.
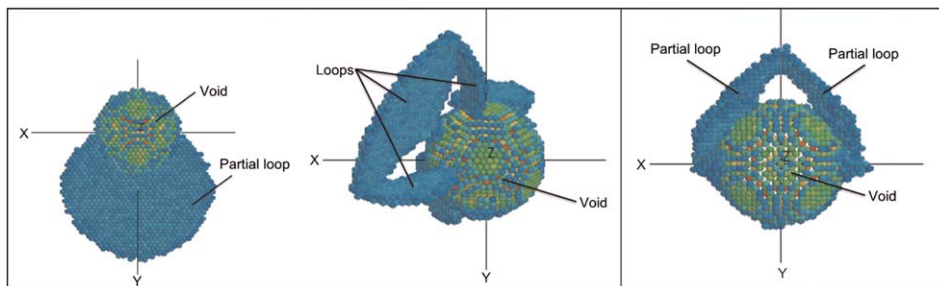
Fig. 79. Emission of partial dislocation loops with trailing stacking faults (blue atoms) for three orientations of the tensile axis: (a) [1 0 0]; (b) [1 1 0]; (c) [1 1 1] [2 2 2].

configuration, which led to necking and did not specifically analyze dislocation activity. Zhu et al. [215] modeled the void growth under shock loading and unloading conditions and obtained profuse evidence for shear loop emission. Marian, Knapp, and Ortiz [220,221] used the quasi-continuum simulation method and were indeed the first to identify shear loops and some of their reactions as the strain increased. However, quasi-continuum calculations perform energy minimization of the system at zero temperature and may give results that differ from MD simulations. Davila et al. [209] modeled the inverse problem: the collapse of a void. We have also carried out MD simulations of void growth, as in the work of Traiviratana et al. [208]. Fig. 79 shows 3D visualizations of MD simulations of the early growth of voids for three directions of the tensile axis: [1 0 0], [1 1 0], and [1 1 1]. Dislocation loops are emitted in the three cases but their configuration is more complex than in the simple 2D model of Section 8.2. The first significant difference is that partial dislocations are emitted instead of perfect dislocations assumed earlier. The blue atoms represent the stacking faults and the green atoms the surface of the voids. The original color illustrations can be found in Bringa et al. [222]. In Figs. 79(a) and 79(b) the trailing partial is also emitted while in Fig. 79(c) only one partial loop is seen. A second difference is that the loops combine to form biplanar (for [1 1 0], Fig. 79(b)) or triplanar (for [1 1 1], Fig. 79(c)) loops. It should be noted that none of our MD simulations showed mobile prismatic loops, thought by many to be the primary mechanism for loop expansion. Further analysis is provided by Meyers et al. [203].

11. Conclusions

(a) Shock-wave compression produces extreme regimes characterized by a state of uniaxial strain, high strain rates, high pressures, and high temperatures.

(b) The conditions are such that plastic deformation occurs primarily at the wave front and release portions and not homogeneously throughout the material, as is the case in conventional deformation.

(c) Dislocation generation and motion in shock compression is governed by these extreme regimes. At lower pressures (below $P/G \sim 1$) conventional dislocation sources are activated and multiplication processes of dislocations dominate the effects. At higher pressures ($P/G > 1$) homogeneous nucleation of dislocation loops takes place with the expansion of the loops through subsonic and possibly, in some cases, supersonic dislocation motion. Several mechanisms of dislocation accommodation are discussed.

(d) This profuse dislocation generation and motion leads to loose dislocation cells in FCC metals and a homogeneous dislocation distribution in other structures.

(e) As the SFE of metals is decreased, the tendency for planar dislocation arrays and stacking faults increases. A criterion for the transition from perfect dislocation loops to partial dislocation loops is presented.

(f) There is also a threshold for twinning, which is reached when the strain rate imparted by shock compression is such that the flow stress by dislocation flow becomes higher than the twinning stress. A criterion for the onset of twinning is presented, for the case in which the twinning stress is independent of strain rate and temperature whereas the flow stress by dislocation motion is determined by thermal activation.

(g) The results of MD calculations are presented. This is a powerful simulation technique that is helping to elucidate some of the thornier issues in shock compression. MD predicts an increasing dislocation density (and decreased spacing) with increasing pressure, in agreement with transmission electron microscopy characterization of recovered shocked specimens.

(h) Comparison of experimental results (by TEM) and MD simulations reveals that the dislocation spacings are orders of magnitude different, being much smaller in the MD simulations. The MD simulations reveal that the annihilation rate of dislocations upon unloading is very high. This suggests that the dislocation density during shock compression might be higher than the residual dislocation density after release.

(i) Controlled quasi-isentropic compression experiments-ICE (ramp-wave compression, in which the loading is adiabatic), provides a strain rate that is lower than shock compression at the same pressure. MD simulations of ramp-wave compression, were also carried out, and characterized. The residual dislocation densities are significantly lower for quasi-isentropic (ramp wave) compression than for shock compression, as predicted by McNaney et al. [135] and Shehadeh et al. [181].

(j) Upon being reflected at a free surface, a shock wave creates a tensile pulse which, if of sufficient magnitude, generates fracture of the metal either by crack or void nucleation, growth, and coalescence. The initiation and growth of voids is shown to occur by the formation and expansion of shear loops from the void surface. These shear loops, originally postulated by Lubarda et al. [200], are shown to be the principal mechanism of void expansion.

Acknowledgment

References

[1] G.A. Askaryon, E.M. Morez, JETP Lett. 16 (1963) 1638.
[2] R.M. White, J. Appl. Phys. 34 (1963) 2123.
[3] C.E. Bell, J.A. Landt, Appl. Phys. Lett. 10 (1967) 46.
[4] E. Panarella, P. Savic, Can. J. Phys. 46 (1968) 143.
[5] C.H. Skeen, C.M. York, J. Appl. Lett. 12 (1968) 369.
[6] N.C. Anderholm, Appl. Phys. Lett. 16 (1970) 113.
[7] W.C. Leslie, J.T. Michalak, F.W. Aul, Iron and Dilute Solid Solutions, Wiley, New York, 1963, p. 119
[8] O. Johari, G. Thomas, Acta Metall. 12 (1964) 1153.
[9] R.L. Nolder, G. Thomas, Acta Metall. 11 (1963) 994.
[10] M.A. Meyers, L.E. Murr, Shock Waves and High-Strain-Rate Phenomena in Metals, Plenum Press, New York, 1981, p. 487.
[11] R.W. Armstrong, C.C. Wu, J. Appl. Phys. 43 (1972) 821.
[12] G.E. Dieter, In Strengthening Mechanisms in Solids, ASM, Metals Park, OH, 1962, p. 279.
[13] G.E. Dieter, in: P.G. Shewmon, V.F. Zackay (Eds.), Response of Metals to High-Velocity Deformation, Interscience, New York, 1961, p. 409.
[14] E.G. Zukas, Met. Eng. Q. 6 (1966) 1.
[15] W.C. Leslie, in: R.W. Rohde, B.M. Butcher, J.R. Holland, C.H. Karnes (Eds.), Metallurgical Effects at High Strain Rates, Plenum Press, New York, 1973, p. 571
[16] L. Davison, R.A. Graham, Phys. Rep. 55 (1979) 255.
[17] M.A. Mogilevsky, P.E. Newman, Phys. Rep. 97 (1988) 359.
[18] L.E. Murr, in: S.C. Schmidt, N.C. Holmes (Eds.), Shock Waves in Condensed Matter, Elsevier, Amsterdam, 1988, p. 315.
[19] M.A. Meyers, Dynamic Behavior of Materials, Wiley, New York, 1994, p. 382.
[20] G.T. Gray III, Influence of shock-wave deformation on the structure/property behavior of materials, in: J.R. Asay, M. Shahinpoor (Eds.), High-Pressure Shock Compression of Solids, Springer, NY, 1993, pp. 187–215.
[21] G.T. Gray, R.S. Hixson, C.E. Morris, in: S.C. Schmidt, R.D. Tasker (Eds.), Shock Compression of Condensed Matter 1991, Elsevier, NY, 1992, p. 427.
[22] B.A. Remington, G. Bazan, J. Belak, E. Bringa, M. Caturla, J.D. Colvin, M.J. Edwards, S.G. Glendinning, D. Ivanov, B. Kad, D.H. Kalantar, M. Kumar, B.F. Lasinski, K.T. Lorenz, J.M. McNaney, D.D. Meyerhofer, M.A. Meyers, S.M. Pollaine, D. Rowley, M. Schneider, J.S.

Stölken, J.S. Wark, S.V. Weber, W.G. Wolfer, B. Yaakobi, Metall. Mater. Trans. 35A (2004) 2587–2608.

[23] R.W. Armstrong, S.M. Walley, Intern. Mater. Rev. 53 (2008) 105–128.

[24] Q. Johnson, A. Mitchell, R.N. Keeler, L. Evans, Phys. Rev. Lett. 25 (1970) 109.

[25] J.S. Wark, Phys. Rev. B 40 (1989) 5705.

[26] D.H. Kalantar, E.A. Chandler, J.D. Colvin, R. Lee, B.A. Remington, S.V. Weber, A. Hauer, J.S. Wark, A. Loveridge, B.H. Failor, M.A. Meyers, G. Ravichandran, Rev. Sci. Instrum. 170 (1999) 629.

[27] E. Orowan, Proc. Phys. Soc. Lond. 52 (1940) 8.

[28] F.J. Zerilli, R.W. Armstrong, J. Appl. Phys. 61 (1987) 1816.

[29] R. W. Armstrong, W. Elban, Dislocations in Solids, Vol. 12, Elsevier, Amsterdam, 2004.

[30] R.W. Armstrong, W. Arnold, F.J. Zerilli, Mater. Metall. Trans. 38A (2007) 2605.

[31] R. W. Armstrong, W. Arnold, F. J. Zerilli, J. Appl. Phys. 105 (2009) 023511.

[32] J.W. Swegle, D.E. Grady, J. Appl. Phys. 58 (1983) 941.

[33] C.S. Smith, Trans. AIME 212 (1958) 574.

[34] E. Hornbogen, Acta Metall. 10 (1962) 978.

[35] M.A. Meyers, in: P. Haasen, V. Gerold, G. Kostorz (Eds.), Strength of Metals and Alloys, Pergamon, New York, 1979, p. 547.

[36] M.A. Meyers, Scripta Metall. 12 (1978) 21.

[37] M.A. Meyers, F. Gregori, B.K. Kad, M.S. Schneider, D.H. Kalantar, B.A. Remington, G. Ravichandran, T. Boehly, J.S. Wark, Acta Mater. 51 (2003) 1211.

[38] G. Xu, A.S. Argon, Philos. Mag. Lett. 80 (2000) 605.

[39] J.P. Hirth, J. Lothe, Theory of Dislocations, McGraw-Hill, New York, 1968.

[40] L.E. Murr, Shock Waves and High-Strain Rate Phenomena in Metals, Plenum Press, New York, 1981, pp. 607–673.

[41] N. Berstein, E.B. Tadmor, Phys. Rev. B 69 (2004) 094116.

[42] L.E. Murr, D. Kuhlmann-Wilsdorf, Acta Metall. 26 (1978) 847.

[43] L.F. Trueb, J. Appl. Phys. 40 (1969) 2976.

[44] E. Zaretsky, J. Appl. Phys. 78 (1995) 1.

[45] J. Weertman, Moving dislocations in the shock front, in: M. A. Meyers, L. E. Murr (Eds.), Shock Waves and High Strain Rate Phenomena in Metals, 1981, p. 469.

[46] J. Weertman, P.S. Follansbee, Mech. Mat. 2 (1983) 265.

[47] P.S. Follansbee, J. Weertman, Mech. Mat. 1 (1982) 345.

[48] J.D. Eshelby, Proc. Phys. Soc. A 62 (1949) 307.

[49] J. Weertman, in: P.G. Shewmon, V.F. Zackay (Eds.), Response of Metals to High-Velocity Deformation, AIME, Interscience, New York, 1961, p. 205.

[50] J. Weertman, J.R. Weertman, in: F.R.N. Nabarro (Ed.), Dislocations in Solids, vol. 3, North-Holland Publishing, Amsterdam, 1980, pp. 1–59.

[51] F.C. Frank, Proc. Phys. Soc. A 62 (1949) 131.

[52] P. Gumbsch, H. Gao, Science 283 (1999) 965.

[53] J.P. Hirth, H.M. Zbib, J. Lothe, Model. Simul. Mater. Sci. Eng. 6 (1998) 165.

[54] J.J. Gilman, Metall. Mater. Trans. A 31 (2000) 811.

[55] M.A. Meyers, A "wavy wave" model for the shocking of polycrystalline metals, in: Proceedings of the 5th International Conference on High Energy Rate Fabrication, Denver Research Institute, Denver, CO, June 1975, pp. 1.4.1–21.

[56] M.A. Meyers, Mater. Sci. Eng. 30 (1977) 99.

[57] M.A. Meyers, M.S. Carvalho, Mater. Sci. Eng. 24 (1976) 131.

[58] R.J. De Angelis, J.B. Cohen, J. Metals 15 (1963) 681.

[59] A.G. Dhere, H.J. Kestenbach, M.A. Meyers, Mater. Sci. Eng. 54 (1982) 113.

[60] F.J.C. Braga, Deformacao por Choque de Cobre Bi e Policristalino, M. Sc. Thesis, Instituto Militar de Engenharia, 1977.

[61] H.J. Kestenbach, M.A. Meyers, Metall. Trans. A (1976) 7.

[62] M.A. Meyers, L.E. Murr, C.Y. Hsu, G.A. Stone, Mater. Sci. Eng. 57 (1983) 113.

[63] K.C. Hsu, K. Robino, M.A. Meyers, Mater. Sci. Eng. 59 (1983) 235.
[64] C.Y. Hsu, K.C. Hsu, L.E. Murr, M.A. Meyers, in: M.A. Meyers, L.E. Murr (Eds.), Shock Waves and High Strain-Rate Phenomena in Metals: Concepts and Applications, Plenum Press, New York, 1981, pp. 433–452.
[65] E.M. Bringa, A. Caro, M. Victoria, N. Park, JOM 57 (2005) 67.
[66] O.E. Jones, J.R. Holland, Acta Metall. 16 (1968) 1037.
[67] J.L. Barber, K. Kadau, Phys. Rev. B 77 (2008) 144106.
[68] C.A. Haynam, P.J. Wegner, J.M. Auerbach, et al., Appl. Opt. 46 (2007) 3276.
[69] L.E. Murr, M.A. Meyers, in: T.Z. Blazynski (Ed.), Explosive Welding, Forming, and Compaction, Applied Science, Elsevier, London, UK, 1983, p. 83.
[70] L.E. Murr, H.R. Vydyanath, J.V. Foltz, Metall. Trans. 1 (1970) 3215.
[71] B. Gonzalez, L.E. Murr, O.L. Valerio, E.V. Esquivel, H. Lopez, Mater. Charact. J. 49 (2003) 359.
[72] L.E. Murr, K.P. Staudhammer, Mater. Sci. Eng. 20 (1975) 35.
[73] L.E. Murr, Residual microstructure-mechanical property relationships in shock-loaded metals and alloys, in: M.A. Meyers, L.E. Murr (Eds.), Shock Waves and High-Strain-Rate Phenomena in Metals, Plenum Press, New York, 1981, p. 607.
[74] J.C. Sanchez, L.E. Murr, K.P. Staudhammer, Acta Mater. 45 (1997) 3223.
[75] E.V. Esquivel, L.E. Murr, E.A. Trillo, M.J. Baquera, Mater. Sci. 38 (2003) 2223.
[76] B. Kazmi, L.E. Murr, Scripta Metall. 13 (1979) 993.
[77] E. Moin, L.E. Murr, Mater. Sci. Eng. 37 (1979) 249.
[78] W.P. Longo, R.E. Reed-Hill, Metallography 4 (1974) 181.
[79] W.P. Longo, R.E. Reed-Hill, Scripta Metall. 4 (1970) 7.
[80] M.A. Meyers, Metall. Trans. 8A (1977) 1583.
[81] G.T. Gray Jr., in: J.R. Asay, M. Shahinpoor (Eds.), High Pressure Shock Compression of Solids, Springer-Verlag, New York, 1993.
[82] D.H. Lassila, T. Shen, M.A. Meyers, Metall. Mater. Trans. A 35 (2004) 2729–2740.
[83] M.S. Schneider, Laser Shock Compression of Copper and Copper-Aluminum Alloys: The Slip to Twinning Transition in High-Strain Rate Deformation, Doctoral dissertation, University of California, San Diego, CA, 2004.
[84] B.Y. Cao, An Experimental and Computational Investigation of Shock Effects in Monocrystalline Copper, Doctoral dissertation, University of California, San Diego, CA, 2006.
[85] M.S. Daw, M.I. Baskes, Phys. Rev. B 29 (1984) 6443.
[86] H. Jarmakani, Quasi-Isentropic and Shock Compression of FCC and BCC Metals: Effects of Grain-Size and Stacking-Fault Energy, Doctoral dissertation, University of California, San Diego, CA, 2008.
[87] B.Y. Cao, D.H. Lassila, M.S. Schneider, B.K. Kad, C.X. Huang, Y.B. Xu, D.H. Kalantar, B.A. Remington, M.A. Meyers, Mater. Sci. Eng. A 409 (2005) 270.
[88] B.Y. Cao, E.M. Bringa, M.A. Meyers, Metall. Mater. Trans. A 38 (2007) 1073.
[89] J.C. Huang, G.T. Gray III, Acta Metall. 37 (1989) 3335.
[90] H. Mughrabi, T. Ungar, W. Kienle, M. Wilkens, Philos. Mag. A 53 (1986) 793.
[91] G.T. Gray III, P.S. Follansbee, in: C.Y. Chiem, H.D. Kunze, L.W. Meyers (Eds.), Impact Loading and Dynamic Behavior of Materials, Informationsgesellschaft Verlag, Germany, 1988, p. 541.
[92] M.S. Schneider, B.K. Kad, D.H. Kalantar, B.A. Remington, M.A. Meyers, Metall. Mater. Trans. A 35 (2004) 2633.
[93] M.S. Schneider, B. Kad, D.H. Kalantar, B.A. Remington, E. Kenik, M.A. Meyers, Int. J. Impact Eng. 32 (2005) 473.
[94] F. Greulich, L.E. Murr, Mater. Sci. Eng. 39 (1979) 81.
[95] O. Vöhringer, Z. Metallk. 67 (1976) 51.
[96] T. Kan, P. Haasen, Mater. Sci. Eng. 5 (1969–1970) 237.
[97] R. Labusch, Phys. Status Solidi 41 (1970) 659.
[98] P. Jax, P. Kratochvil, P. Haasen, Acta Metall. 18 (1970) 237.

[99] I.S. Choi, A.J. Detor, R. Schwaiger, M. Dao, C.A. Schuh, S. Suresh, J. Mech. Phys. Sol. 56 (2008) 172.
[100] A.W. Thompson, Acta Metall. 23 (1975) 1337.
[101] A.W. Thompson, Acta Metall. 25 (1977) 83.
[102] A.W. Thompson, M.I. Baskes, W.F. Flanagan, Acta Metall. 21 (1973) 1017.
[103] U. Andrade, High Strain, High-Strain Rate Deformation of Copper, Doctoral thesis, University of California, San Diego, CA, 1993.
[104] R.J. Asaro, S. Suresh, Acta Mater. 53 (2005) 3369.
[105] H.A. Roth, R.C. Davis, R.C. Thomson, Metall. Trans. A 28 (1997) 1329.
[106] M.A. Meyers, O. Vöhringer, V.A. Lubarda, Acta Mater. 49 (2001) 4025.
[107] R.Z. Becker, Phys. Z. 26 (1925) 919.
[108] A.Z. Seeger, Naturf 26 (1954) 758.
[109] A.Z. Seeger, Naturf 26 (1954) 818.
[110] A.Z. Seeger, Naturf 26 (1954) 851.
[111] J.W. Christian, S. Mahajan, Prog. Mater. Sci. (1995) 39.
[112] P. Haasen, Philos. Mag. 3 (1958) 384.
[113] M.A. Meyers, U.R. Andrade, A.H. Chokshi, Metall. Mater. Trans. A 26 (1995) 2881.
[114] R.W.K. Honeycombe, The Plastic Deformation of Metals, Edward Arnold Ltd., London, UK, 1984, p. 163.
[115] L.E. Murr, Interfacial Phenomena in Metals and Alloys, Addison-Wesley, Reading, MA, 1975, p. 142.
[116] J.A. Venables, Philos. Mag. 6 (1961) 379.
[117] J.A. Venables, in: R.E. Reed-Hill, J.P. Hirth, H.C. Rogers (Eds.), Deformation Twinning, Gordon and Breach, New York, 1964, p. 77.
[118] O.Z. Vöhringer, Z. Metallk. 65 (1974) 352.
[119] O.Z. Vöhringer, Z. Metallk. 11 (1972) 1119.
[120] H. Van Swygenhoven, P.M. Derlet, A.G. Froseth, Nat. Mater. 3 (2004).
[121] S. Ogata, J. Li, S. Yip, Phys. Rev. B 71 (2005) 224102.
[122] D. Siegel, Appl. Phys. Lett. 87 (2005) 121901.
[123] T.C. Tiearney, N.J. Grant, Metall. Trans. A 13 (1982) 1827.
[124] J.W. Swegle, D.E. Grady, in: Y.M. Gupta (Ed.), Shock Waves in Condensed Matter – 1985, Plenum Press, New York, 1986, p. 353.
[125] A. Cottrell, Dislocations and Plastic Flow in Crystals, Clarendon Press, Oxford, UK, 1953, p. 54.
[126] G. Xu, A.S. Argon, Philos. Mag. 80 (2000) 605.
[127] J.R. Rice, J. Mech. Phys. Sol. 40 (1992) 256.
[128] M. Khantha, V. Vitek, Acta Mater. 45 (1997) 4675.
[129] M.A. Meyers, M.S. Schneider, H. Jarmakani, B. Kad, B.A. Remington, D.H. Kalantar, J. McNaney, B. Cao, J. Wark, Metall. Mater. Trans. A 39 (2008) 304.
[130] H.N. Jarmakani, E.M. Bringa, P. Erhart, B.A. Remington, Y.M. Wang, N.Q. Vo, M.A. Meyers, Acta Mater. 56 (2008) 5584.
[131] D. Hull, D.J. Bacon, Introduction to Dislocations, Butterworth-Heinemann, Oxford, UK, 2001, p. 147.
[132] D.L. Preston, D.C. Wallace, Solid State Commun. 81 (1992) 277.
[133] G.A. Lyzenga, A.J. Ahrens, in: W.J. Nellis, Seaman, R.A. Graham (Eds.), American Institute of Physics Conference Proceeding No. 78, 1982, p. 231.
[134] L.M. Barker, in: J.A. Asay, R.A. Graham, G.K. Straub (Eds.), Shock Waves in Condensed Matter, Elsevier, Amsterdam, 1984.
[135] J.M. McNaney, M.J. Edwards, R. Becker, K.T. Lorenz, B.A. Remington, Metall. Trans. A 35A (2004) 265.
[136] C.A. Hall, J.R. Asay, M.D. Kundson, W.A. Stgar, R.B. Spielman, T.D. Pointon, Rev. Sci. Instrum. 72 (2004) 265.
[137] J.H. Nguyen, D. Orlikowski, F.H. Streitz, N.C. Holmes, J.A. Moriarty, in: M.D. Furnish, L.C. Chhabildas, R.S. Hixson (Eds.), AIP Conference Proceedings, Melville, NY, 2004.
[138] D.L. Preston, D.L. Tonks, D.C. Wallace, J. Appl. Phys. 93 (2003) 211.

[139] H. Jarmakani, J.M. McNaney, B. Kad, D. Orlikowski, J.H. Nguyen, M.A. Meyers, Mater. Sci. Eng. A 463 (2007) 269.
[140] B.L. Holian, G.K. Straub, Phys. Rev. Lett. 43 (1979) 1598.
[141] M.A. Mogilevsky, in: M.A. Meyers, L.E. Murr (Eds.), Shock Waves and High-Strain Rate Phenomena in Metals, Plenum Press, New York, 1981, p. 531.
[142] M.A. Mogilevsky, V.V. Efremov, I.O. Minkin, Fizika Gorenyai Vzryva 13 (1977) 750.
[143] B.L. Holian, W.G. Hoover, B. Moran, G.K. Straub, Phys. Rev. A 22 (1980) 2498.
[144] B.L. Holian, Phys. Rev. A 37 (1988) 2562.
[145] B.L. Holian, P.S. Lomdahl, Science 280 (1998) 2085.
[146] D.H. Tsai, C.W. Becket, J. Geophys. Res. 71 (1966) 2601.
[147] V. Zybin, M.L. Elert, C.T. White, Phys. Rev. B 66 (2002) 220102.
[148] A. Strachan, D. van Duin, S.D. Chakraborty, W.A. Goddard, Phys. Rev. Lett. 91 (2003) 098301.
[149] A.P. Dremov, P. Sapozhnikov, M. Smirnova, D.L. Preston, M.A. Zocher, Phys. Rev. B 74 (2006) 144140.
[150] K. Kadau, T.C. Germann, P.S. Lomdahl, B.L. Holian, Phys. Rev. B 72 (2005) 064120.
[151] E.M. Bringa, A. Caro, Y. Wang, M. Victoria, J.M. McNaney, B.A. Remington, R.F. Smith, B.R. Torralva, H. Van Swygenhoven, Science 309 (2005) 1838.
[152] C.L. Kelchner, S. Plimpton, J.C. Hamilton, Phys. Rev. B 58 (1998) 11085.
[153] S.J. Plimpton, J. Comput. Phys. 117 (1995) 1–19, http://lammps.sandia.gov
[154] T.C. Germann, B.L. Holian, P.S. Lomdahl, D. Tanguy, M. Mareschal, R. Ravelo, Metall. Mater. Trans. A 35 (2004) 2609.
[155] Y. Mishin, D. Farkas, M.J. Mehl, D.A. Papaconstantantopoulos, Phys. Rev. B 59 (1999) 3393.
[156] M.S. Daw, M.I. Baskes, Phys. Rev. Lett. 50 (1983) 1285.
[157] B.L. Holian, Shock Waves 13 (2004) 489.
[158] M.H. Rice, R.G. McQueen, J.M. Walsh, Solid State Phys. 6 (1958) 1.
[159] T.C. Germann, B.L. Holian, P.S. Lomdahl, Phys. Rev. Lett. 84 (2000) 5351.
[160] D. Tanguy, M. Mareschal, P.S. Lomdahl, T.C. Germann, B.L. Holian, R. Ravelo, Phys. Rev. B 68 (2003) 14111.
[161] L. Koci, E.M. Bringa, D.S. Ivanov, Phys. Rev. B 74 (2006) 12101.
[162] R. Ravelo, Shock Compression of Condensed Matter, 2007.
[163] C.S. Smith, Response of Metals to High Velocity Deformation, Interscience Publishers, New York, 1961, pp. 483–486.
[164] E.M. Bringa, J.U. Cazamias, P. Erhart, J. Stolken, N. Tanushev, B.D. Wirth, R.E. Rudd, M.J. Caturla, J. Appl. Phys. 96 (2004) 3793.
[165] O.J. Kum, Appl. Phys. 93 (2003) 3239.
[166] N.A. Kubota, S.J. Economou, S.J. Plimpton, J. Appl. Phys. 83 (1998) 4055.
[167] E.M. Bringa, K. Rosolankova, R.E. Rudd, B.A. Remington, J.S. Wark, M. Duchaineau, D.H. Kalantar, J. Hawreliak, J. Belak, Nat. Mater. 5 (2006) 805.
[168] Y.M. Wang, E.M. Bringa, J.M. McNaney, M. Victoria, A. Caro, A.M. Hodge, R. Smith, B. Torralba, B.A. Remington, Appl. Phys. Lett. 88 (2006) 061917.
[169] Z. Lin, L.V. Zhigilei, V. Celli, Phys. Rev. B 77 (2008) 075133.
[170] Z.B. Lin, R.A. Johnson, L.V. Zhigilei, Phys. Rev. B 77 (2008) 214108.
[171] M.A. Meyers, F. Gregori, B.K. Kad, M.S. Schneider, D.H. Kalantar, B.A. Remington, G. Ravichandran, T. Boehly, J.S. Wark, Acta Mater. 51 (2003) 1211.
[172] B. Cao, D. H. Lassila, C. Huang, Y. Xu, M. A. Meyers, University of California, San Diego, CA, Mater. Sci. Eng. A, submitted 2009.
[173] C.H. Ma, L.E. Murr, Proceedings of 5th International Conference on High Energy Rate Fabrication, vol. 1, Denver, CO, 1977, p. 1.6.1.
[174] U. Andrade, M.A. Meyers, K.S. Vecchio, A.H. Chokshi, Acta Metall. Mater. 42 (1994) 3183.
[175] Y.M. Wang, E.M. Bringa, J.M. McNaney, M. Victoria, A. Caro, A.M. Hodge, R. Smith, B. Torralva, B.A. Remington, C.A. Schuh, H. Jarmakani, M.A. Meyers, Appl. Phys. Lett. 88 (2006) 061917.
[176] H. Van Swygenhoven, M. Spaczer, A. Caro, D. Farkas, Phys. Rev. B 60 (1999) 22.
[177] H. Van Swygenhoven, P.M. Derlet, A.G. Frøseth, Nat. Mater. 3 (2004) 399.
[178] N.Q. Vo, S. Odunuga, P. Bellon, R.S. Averback, A. Caro. Phys. Rev. B 77 (2008) 134108.

[179] S. Odunuga, Y. Li, P. Krasnochtchekov, P. Bellon, R.S. Averback, Phys. Rev. Lett. 95 (2005) 045901.
[180] E.M. Bringa, A. Caro, E. Leveugle, Appl. Phys. Lett. 89 (2006) 23101.
[181] M.A. Shehadeh, E.M. Bringa, H.M. Zbib, J.M. McNaney, B.A. Remington, Appl. Phys. Lett. 89 (2006) 171918.
[182] M. Chen, E. Ma, K.J. Hemker, H. Sheng, Y. Wang, X. Cheng, Science 300 (2003) 1275.
[183] Y.T. Zhu, X.Z. Liao, S.G. Srinivasan, Y.G. Zhao, M.I. Baskes, Appl. Phys. Lett. 85 (2004) 5049.
[184] J. Schiøtz, K.W. Jacobsen, Science 301 (2003) 1357.
[185] B.L. Holian, A.F. Voter, N.J. Wagner, R.J. Ravelo, S.P. Chen, W.G. Hoover, C.G. Hoover, J.E. Hammerberg, T.D. Dontje, Phys. Rev. A 43 (1991) 2655.
[186] Y.M. Wang, E.M. Bringa, M. Victoria, A. Caro, J.M. McNaney, R. Smith, B.A. Remington, J. Phys. IV France 134 (2006) 915.
[187] C.A. Schuh, T.G. Nieh, T. Yamasaki, Scripta Mater. 46 (2002) 735.
[188] C.A. Schuh, T.G. Nieh, H. Iwasaki, Acta Mater. 51 (2003) 431.
[189] D.H. Warner, W.A. Curtin, S. Qu, Nat. Mater. 6 (2007) 876.
[190] M.A. Shehadeh, H.M. Zbib, T. Diaz de la Rubia, Int. J. Plasticity 21 (2005) 2369.
[191] M.A. Shehadeh, H.M. Zbib, T. Diaz de la Rubia, Philos. Mag. 85 (2005) 1667.
[192] J. Hawreliak et al., submitted.
[193] A. Loveridge-Smith, A. Allen, J. Belak, et al., Phys. Rev. Lett. 86 (2001) 2349.
[194] F. Seitz, Phys. Rev. 79 (1950) 723.
[195] L.M. Brown, Philos. Mag. 21 (1970) 329.
[196] J. Silcox, P.B. Hirsch, Philos. Mag. 4 (1958) 72.
[197] F.J. Humphreys, P.B. Hirsch, Proc. R. Soc. Lond. 318 (1970) 73–92.
[198] B.P. Uberuaga, R.G. Hoagland, A.F. Voter, S.M. Valone, Phys. Rev. Lett. 99 (2007) 135501.
[199] W.G. Wolfer, Philos. Mag. 58 (1988) 285.
[200] V.A. Lubarda, M.S. Schneider, D.H. Kalantar, B.A. Remington, M.A. Meyers, Acta Mater. 52 (2004) 1397.
[201] S. Christy, H.R. Pak, M.A. Meyers, Metallurgical Applications of Shock Wave and High-Strain-Rate Phenomena, Marcel Dekker, New York, 1986, p. 835.
[202] M.F. Ashby, Philos. Mag. 21 (1970) 399.
[203] M.A. Meyers, S. Traiviratana, D.J. Benson, E.M. Bringa, JOM, February 2009, 61 (2009) 35.
[204] J.R. Rice, R. Thomson, Philos. Mag. A 29 (1974) 73.
[205] J. Dundurs, T.J. Mura, Mech. Phys. Solids 12 (1964) 177.
[206] J.R. Rice, J. Mech. Phys. Solids 40 (1992) 239.
[207] J.R. Rice, G.E. Beltz, J. Mech. Phys. Solids 42 (1994) 33.
[208] S. Traiviratana, E.M. Bringa, D.J. Benson, M.A. Meyers, Acta Mater. 56 (2008) 3874.
[209] L.P. Dávila, P. Erhart, E.M. Bringa, M.A. Meyers, V.A. Lubarda, M.S. Schneider, R. Becker, M. Kumar, Appl. Phys. Lett. 86 (2005) 161902.
[210] R.W. Minich, M. Kumar, J. Cazamias, A.J. Schwartz, in: Dynamic Deformation: Constitutive Modeling, Grain Size, and Other Effects, 2003 TMS Annual Meeting, San Diego, CA, 2003.
[211] M.A. Meyers, A.K. Zurek, in: L. Davison, D.E. Grady, M. Shahinpoor (Eds.), High Pressure Shock Compression of Solids II, Springer, New York, 1995, p. 25.
[212] M.A. Meyers, in: M.A. Meyers, R.W. Armstrong, H.O.K. Kirchner (Eds.), Mechanics and Materials: Fundamentals and Linkages, John Wiley, NY, 1999, p. 489.
[213] S.G. Srinivasan, M.I. Baskes, G.J. Wagner, J. Mater. Sci. 41 (2006) 7838.
[214] G.P. Potirniche, M.F. Horstemeyer, G.J. Wagner, P.M. Gullett, Int. J. Plasticity 22 (2006) 257.
[215] W. Zhu, Z. Song, X. Deng, H. He, X. Cheng, Phys. Rev. B 75 (2007) 024104-1.
[216] R.E. Rudd, J.F. Belak, Comput. Mater. Sci. 24 (2002) 148.
[217] E.T. Seppälä, J.F. Belak, R.E. Rudd, Phys. Rev. B 69 (2004) 134101-1-19.
[218] E.T. Seppälä, J. Belak, R.E. Rudd, Phys. Rev. Lett. 93 (2004) 245503-1-4.
[219] E.T. Seppälä, J. Belak, R.E. Rudd, Phys. Rev. B 71 (2005) 064112-1-10.
[220] J. Marian, J. Knap, M. Ortiz, Phys. Rev. Lett. 93 (2004) 1.
[221] J. Marian, J. Knap, M. Ortiz, Acta Mater. 53 (2005) 2893.
[222] E.M. Bringa, S. Traiviratana, M.A. Meyers, to be published (2010).